Structural robustness and temporal vulnerability of the starvation-responsive metabolic network in liver of healthy and obese mice

Keigo Morita[1,2], Atsushi Hatano[1,3,4], Toshiya Kokaji[1,5], Hikaru Sugimoto[6], Takaho Tsuchiya[7,8], Haruka Ozaki[7,8], Riku Egami[9], Dongzi Li[1], Akira Terakawa[1], Satoshi Ohno[1,2,10], Hiroshi Inoue[11], Yuka Inaba[11], Yutaka Suzuki[9], Masaki Matsumoto[3], Masatomo Takahashi[12], Yoshihiro Izumi[12], Takeshi Bamba[12], Akiyoshi Hirayama[13], Tomoyoshi Soga[13, 14], and Shinya Kuroda[1,2,6,9, *]

[1]Department of Biological Sciences, Graduate School of Science, The University of Tokyo, 7-3-1 Hongo, Bunkyo-ku, Tokyo 113-0033, Japan.

[2]Molecular Genetics Research Laboratory, Graduate School of Science, The University of Tokyo, 7-3-1 Hongo, Bunkyo-ku, Tokyo, Japan.

[3]Department of Omics and Systems Biology, Graduate School of Medical and Dental Sciences, Niigata University, 757 Ichibancho, Asahimachi-dori, Chuo-ku, Niigata City, Niigata 951-8510, Japan.

[4]Laboratory for Integrated Cellular Systems, RIKEN Center for Integrative Medical Sciences, 1-7-22 Suehiro-cho, Tsurumi-ku, Yokohama, Kanagawa, 230-0045, Japan

[5]Data Science Center, Nara Institute of Science and Technology, 8916-5 Takayama, Ikoma, Nara, 630-0192, Japan.

[6]Department of Biochemistry and Molecular Biology, Graduate School of Medicine, The University of Tokyo, 7-3-1 Hongo, Bunkyo-ku, Tokyo 113-0033, Japan.

[7]Bioinformatics Laboratory, Institute of Medicine, University of Tsukuba, Ibaraki, 305-8575, Japan.

[8]Center for Artificial Intelligence Research, University of Tsukuba, Ibaraki, 305-8577, Japan.

[9]Department of Computational Biology and Medical Sciences, Graduate School of Frontier Sciences, The University of Tokyo, 5-1-5 Kashiwanoha, Kashiwa, Chiba 277-8562, Japan.

[10]Department of AI Systems Medicine, M&D Data Science Center, Tokyo Medical and Dental University, 1-5-45 Yushima, Bunkyo-ku, Tokyo 113-8510, Japan.

[11]Metabolism and Nutrition Research Unit, Institute for Frontier Science Initiative, Kanazawa University, 13-1 Takaramachi, Kanazawa, Ishikawa, 920-8641, Japan.

[12]Division of Metabolomics, Medical Research Center for High Depth Omics, Medical Institute of Bioregulation, Kyushu University, Fukuoka 812-8582, Japan.

[13]Institute for Advanced Biosciences, Keio University, 246-2 Mizukami, Kakuganji, Tsuruoka, Yamagata 997-0052, Japan

[14]Human Biology-Microbiome-Quantum Research Center (WPI-Bio2Q), Keio University, Tokyo 108-8345, Japan.

*Correspondence to: skuroda@bs.s.u-tokyo.ac.jp (S.K.)

Abstract

Adaptation to starvation is a multi-molecular and temporally ordered process, that could be impaired in obesity. To elucidate how the healthy liver regulates various molecules in a temporally ordered manner during starvation and how obesity disrupts this process, we measured time course multiomic data in the liver of wild-type (WT) and leptin-deficient obese (*ob*/*ob*) mice during starvation. Using the measured data, we constructed a starvation-responsive metabolic network, that is a transomic network including responsive molecules and their regulatory relationships during starvation, and analyzed the structure of the network. In WT mice, ATP and AMP, the energy indicators, regulated various metabolic reactions in the network as the hub molecules, both of which were not responsive in *ob*/*ob* mice. However, the structural properties of the network were maintained in *ob*/*ob* mice. In WT mice, the molecules in the network were temporally ordered through metabolic process coordinated by the hub molecules including ATP and AMP and were positively or negatively co-regulated. By contrast, both temporal order and co-regulation were disrupted in *ob*/*ob* mice. Taken together, the starvation-responsive metabolic network is structurally robust, but temporally vulnerable by the loss of responsiveness of the hub molecules in obesity. In addition, we proposed a potential therapeutic target to treat the negative effects of obesity on intermittent fasting to extend lifespan.

One Sentence Summary

Hub molecules activate or inhibit various molecules in a temporally ordered manner in healthy liver, and the regulatory network is structurally robust but temporally vulnerable to obesity.

Introduction

Adaptation to starvation is important for life to maintain systemic homeostasis, that is a multi-molecular and temporally ordered process to optimize fuel usage (*1–6*). This process involves various molecules, including metabolites, lipids, metabolic enzymes, transcription factors (TFs), and protein kinases. These molecules are temporally ordered across metabolic processes, such as glycogen degradation, gluconeogenesis, and fatty acid degradation. However, how the liver, a central organ for metabolism (*7*, *8*), coordinates various molecules in a temporally ordered manner during starvation at a multiomic scale has been elusive. This is because of the lack of a multiomic measurement at precise time intervals during starvation in mammals, although many researches have conducted omic measurements during starvation at a limited number of time intervals in mammals (*9–19*) or time course omic measurements in microorganisms (*20–23*) or worms (*24*).

Obesity is a pathological status that affects various metabolic processes (*25–29*) including adaptation to starvation (*30*), but the global landscape of the effects at a multiomic scale has been elusive. In addition, obesity cancels the beneficial effects on lifespan of intermittent fasting, that is a permissive form of dietary restriction because of an accessible compliance (*31*). The effects of intermittent fasting, which is a long-term and repetitive starvation, result from the cumulative effects of short-term starvation. Thus, clarifying the differences of adaptation to short-term starvation between healthy and obese mice would be informative for investigating an effective therapeutic target of intermittent fasting for obese patients.

Analysis of properties of biological network is a powerful approach to understand such a multi-molecular process like adaptation to starvation (*32–35*). We

have developed transomic analysis, an analytical workflow for addressing multi-molecular processes (*36–38*). With this approach, we can integrate multiomic data into a transomic network, offering a global landscape of biochemical reactions. Recently, we showed that analysis of the structural properties of the transomic network aids in their interpretation during oral glucose ingestion (*39*). A network contains of nodes and edges: nodes are entities such as molecules; edges are relationships between nodes such as regulatory events (activation or inhibition). Network structure is how the edges connect nodes. Biological networks, such as metabolic networks (*40–42*), are often scale-free, which means that a small number of "hub" nodes interact with many other nodes, and large number of "leaf" nodes interact with a few other nodes (*43*). We showed that the transomic network is likely scale-free and structural properties of the networks were different between healthy and obese mice during oral glucose ingestion (*39*). However, we have not investigated the relationships between the structural properties and temporal orders of the transomic network, as well as temporal co-regulations, the correlated temporal patterns of nodes in a biological network. Because adaptation to starvation is a temporally ordered multi-molecular process, integrating the structural and temporal analysis of the transomic network would offer mechanistic insights of adaptation to starvation.

In this study, we measured multiomic data, constructed a transomic network, and conducted structural and temporal analyses of the network in the liver of wild-type (WT) and leptin-deficient obese (*ob*/*ob*) mice, a commonly used model of obesity caused by overeating due to loss of leptin (*44*). Through structural analyses, we showed that the starvation-responsive metabolic network is a scale-free-like network and that the structural properties of the network were maintained in *ob*/*ob* mice. We integrated

structural and temporal analyses of the transomic network. We found that the network was temporally ordered by hub nodes, such as ATP and AMP, in WT mice, but the temporal order was disrupted in *ob*/*ob* mice, as well as temporal co-regulations. This global feature of the starvation-responsive metabolic network was conserved in glycolysis/gluconeogenesis. However, the structural property of the starvation-responsive metabolic network in urea cycle was disrupted as well as the temporal properties, suggesting the profound disruption of amino acid metabolism in *ob*/*ob* mice during starvation. Our omic data was also informative for the study of dietary restriction. Taken together, the starvation-responsive metabolic network was well-structured, temporally ordered, and co-regulated in healthy liver. The network was structurally robust but temporally vulnerable to obesity.

The focus here is adaptive responses to starvation, rather than direct comparisons between WT and *ob*/*ob* mice in a steady state. We have conducted such comparative studies previously for fasting and fed states (*45*, *46*). Note that identical data of 0 h starvation have been already published in one of our studies (*46*).

Results

Workflow for the construction and analysis of a global starvation-responsive transomic network in liver of WT and *ob*/*ob* mice

To describe the temporal dynamics of various molecules during adaptation to starvation in healthy liver and pathological alterations caused by obesity, we constructed and analyzed a global starvation-responsive transomic network in liver of WT and *ob*/*ob* mice (Fig. 1). We collected multiomic data from mice starved for 0, 2, 4, 6, 8, 12, 16, and 24 hours (Fig. 1**A**). We measured the metabolome, lipidome, FFA & acyls (free fatty acids, acyl-carnitines, and acyl-CoAs), transcriptome, proteome, and phosphoproteome in liver. We also measured the metabolome in plasma.

Using the collected data, we conducted a single-omic layer analysis (Fig. 1**B**, and **C**). We identified starvation-responsive molecules and classified them into 4 groups in each layer (Fig. 1**B**): "common," those that exhibited the same response in both WT and *ob*/*ob* mice; "WT-specific," those that occurred only in WT mice; "*ob*/*ob*-specific," those that occurred only in *ob*/*ob* mice; and "opposite," those that exhibited opposing responses between WT and *ob*/*ob* mice. These results formed a single omic layer (Fig. 1**C**). Note that phosphorylation is a process occurred on a phosphosite, not a molecule, but we refer phosphorylation events as molecules as well as metabolites, lipids, FFA & acyls, proteins, and transcripts for simplicity.

The starvation-responsive molecules cooperatively activate or inhibit metabolic reactions to adapt to starvation across the multiomic layers (Fig. 1**D**). Metabolites, lipids, and FFA & acyls serve as substrates, products, and allosteric regulators for metabolic reactions. Enzyme abundance and phosphorylation activate or inhibit the metabolic reactions. TFs increase or decrease enzyme abundance through the gene

regulatory network, although the control is partial because of the effects of protein translation and degradation. Protein kinases increase or decrease enzyme phosphorylation through kinase-substrate network to regulate enzyme activity. Using bioinformatic platforms, we integrated single omic layers along the regulatory network of metabolic reactions and constructed a global starvation-responsive transomic network (Fig. 1**E**). In this manuscript, we refer to "regulation" as encompassing both activation and inhibition when no specific regulatory relationship is mentioned, for simplicity.

Metabolic enzymes, metabolites, lipids, and FFA & acyls, are direct, major and fine regulators of metabolism (*37*, *47*, *48*). Therefore, we focused on the starvation-responsive metabolic network, that is the sub-network of the global starvation-responsive transomic network (Fig. 1**D** and **E**, dotted orange outline) to investigate structural and temporal properties of the network. The starvation-responsive metabolic network contains the direct regulators of metabolic reactions: metabolite, lipid, FFA & acyls, enzyme_protein (protein abundances of metabolic enzymes), and enzyme_PTM (phosphorylation of metabolic enzymes). We investigated structural properties of this starvation-responsive metabolic network (Fig. 1**F**), the temporal order of changes in the network (Fig. 1**G**), and temporal co-regulation among molecules (Fig. 1**H**).

171 **Single-omic layer analysis: identification of starvation-responsive molecules and**
172 **their regulators**
173 We measured seven omic layers: metabolome, lipidome, FFA & acyls, transcriptome,
174 proteome, and phosphoproteome in the liver and metabolome in plasma (see fig. S1 for
175 representative examples, and fig. S2 and Data File S1 for complete data) and performed
176 a single-omic layer analysis in WT and *ob*/*ob* mice (Fig. 2). We conducted one-way
177 ANOVA tests (ANOVA-like testing of edgeR (*49–51*) for transcriptome) in WT and
178 *ob*/*ob* mice respectively, and defined molecules that showed a *P* value less than 0.025 as
179 starvation-responsive molecules (Fig. 2**A**; Data File S2), whose false discovery rates
180 were less than 0.1 except for phosphoproteome data (Table 1). Based on the area under
181 the curve (AUC) of the log2-transformed time courses (Fig. 2**B**), starvation-responsive
182 molecules with positive AUCs were classified as increased molecules (orange), and
183 those with negative AUCs were classified as decreased molecules (purple). Using these
184 classifications, we defined four classes of molecules: common (changing similarly in
185 both WT and *ob*/*ob* mice, green), WT-specific (blue), *ob*/*ob*-specific (red), and opposite
186 (changing in opposite directions in WT and *ob*/*ob* mice, magenta) (Fig. 2**C**).
187 We identified starvation-responsive molecules in the single-omic layer analyses
188 of metabolites (Fig. 2**D**), lipids (Fig. 2**E**; Table 2), FFA & acyls (Fig. 2**F**), plasma
189 metabolites (Fig. 2**G**), transcripts (Fig. 2**H**), proteins (Fig. 2**I**), and phosphorylation
190 events (Fig. 2**J**). The common group comprised more than one-third of the total
191 responsive metabolites in both liver (Fig. 2**D**) and plasma (Fig. 2**G**), FFA & acyls (Fig.
192 2**F**), and transcripts (Fig. 2**H**). Most starvation-responsive lipids were in the *ob*/*ob*-
193 specific group (Fig. 2**E**). More than half of responsive proteins (Fig. 2**I**) and
194 phosphorylation events (Fig. 2**J**) were WT-specifically responsive.

KEGG pathway enrichment analysis (Data File S3) revealed pathways that were associated with the starvation-responsive changes in both the transcriptome (Table 3) and proteome (Table 4). For example, KEGG pathways such as “fatty acid degradation” and “PPAR signaling pathway” were enriched in both transcriptome (Table 3) and proteome (Table 4) in WT mice. However, this analysis did not find any pathways that were enriched in the phosphoproteome data (Data File S3).

We inferred changes in the activities of following regulators of the starvation-responsive molecules (Fig. 2**K**): TFs (Fig, 2**L**; Table 5; Data File S4), protein kinases (Fig. 2**M**; Table 6; Data File S4), and signaling pathways (Fig. 2**N**; Table 7) based on the regulatory network obtained from bioinformatic platforms and measured omic data. Note that signaling pathway layer (Fig. 2**N**; Table 7) contains significantly enriched signaling pathways in any of the transcriptome (Table 3) or proteome data (Table 4). We classified the activities of these regulators as common, WT-specific, *ob*/*ob*-specific, or opposite (Fig. 2**K**). The common group comprised more than half of the total responsive TFs (Fig. 2**L**; Table 5), including Pparα and Hnf4α, well-established for promoting lipid degradation (*5*). Note that some circadian TFs are included beacause of sampling time and some results were not consistent with the previous studies such as failure of identification of Foxo1 and unexpected identification of Creb1 as an inhibited ~~down-regulated~~ TF~~s~~. These problems were caused by insufficient accuracy and comprehensiveness of the database and omic data, particularly the limited number of quantified proteins and phosphorylation sites. “PKC_group” kinases including Prkce, Prkcd and Prkcz, master regulators of liver metabolism (*52–54*), were commonly inhibited (Fig. 2**M**; Table 6). The “PPAR signaling pathway” was inferred as an activated signaling pathway (Fig. 2**N**; Table 7) commonly in WT and *ob*/*ob* mice.

Construction of the global starvation-responsive transomic network by integrating multiomic data

Using the starvation-responsive molecules and their regulators (Fig. 2), we constructed a global starvation-responsive transomic network (Fig. 3**A**; Data File S5). The network consists of nodes, layers, and edges. Nodes represent measured molecules (Figs 2**D**-**J**), inferred activities of the TFs, protein kinases, and signaling pathways (Figs. 2**L**, **M**, and **N**), metabolic reactions defined using KEGG (*55–57*), and transport activities from TCDB (*58*). Based on chemical properties, biological functions, or both, nodes were clustered into layers (see Table 8 for the precise definition). For example, the enzyme_protein layer includes proteins (chemical property) that are metabolic enzymes (biological functions). Enzyme_PTM layer represents phosphorylation (chemical property) of metabolic enzymes (biological functions). Metabolite, lipid, and FFA & acyls layers are assigned based on the chemical properties of the molecules. Edges are the regulatory connections between nodes, connected based on the regulatory relationships among omic layers (fig. S3**A**, **B**, **C**, and **D**), using bioinformatic platforms ~~(see Methods)~~. For example, edges from metabolite, lipid, and FFA & acyls layers to metabolic reaction layer represent the regulatory relationships among metabolites, lipids, and FFA & acyls— as substrates, products, and allosteric regulators— to metabolic reactions. Edges from enzyme_protein and enzyme_PTM to the metabolic reaction layer represent the regulatory relationships between metabolic enzymes and metabolic reactions mediated by enzyme abundance (enzyme_protein) and phosphorylation (enzyme_PTM). Colors of nodes and edges represent the type of response: green, common in both WT and *ob*/*ob* mice; blue, specific to WT mice; red,

242 specific to *ob*/*ob* mice; magenta, opposite responses between WT and *ob*/*ob* mice (Fig.
243 3**A** and **B**).
244 We showed the proportions of the commonly, WT-specifically, *ob*/*ob*-
245 specifically, and oppositely responsive nodes and edges in the global starvation-
246 responsive transomic network (Fig 3**B**). In this network, pie charts represent the
247 proportions of the classes of responses of nodes in the omic layers, and bar plots
248 between pie charts represent proportions of the classes of edges between omic layers.
249 For clear visualization, pie charts for signaling_activity and TF_activity are displayed
250 twice.
251 We assessed the proportions of the global starvation-responsive transomic
252 network (Fig. 3**B**). Although less than half (47 out of 122 nodes) of the starvation-
253 responsive metabolites ("metabolite" in Fig. 3**B**) were specific to WT mice, more than
254 half regulatory connections between the metabolites ("metabolite" in Fig. 3**B**) and the
255 metabolic reactions ("metabolic reaction" in Fig. 3**B**) were specific to WT mice (604
256 out of 1,008 substrate and product relationships and 828 out of 1,538 allosteric
257 regulatory relationships). Among the starvation-responsive lipids ("lipid" in Fig. 3**B**),
258 but not the FFA & acyls ("FFA & acyls" in Fig. 3**B**), most changes (8 out of 10) were
259 specific to *ob*/*ob* mice. This enrichment in the *ob*/*ob*-specific response also occurred
260 among the substrate, product, and allosteric regulatory connections between the lipids
261 ("lipid" in Fig. 3**B**) and the metabolic reactions ("metabolic reaction" in Fig. 3**B**) with
262 43 out of 48 substrate and product relationships *ob/ob*-specific and 160 out of 163
263 allosteric regulator relationships *ob/ob*-specific. This enrichment of *ob*/*ob*-specifically
264 responsive regulatory connections was due to a larger number of *ob*/*ob*-specifically

265 responsive lipids. In addition, the number of regulations from commonly responsive
266 lipids and oppositely responsive lipids was very small (fig. S3**E**).
267 In the enzyme_protein layer ("enzyme_protein" in Fig. 3**B**), most nodes were
268 in the WT-specific class (130 of the 203, 64%) and only 17 of the 203 (8.4%)
269 starvation-responsive nodes responded in common between WT and *ob/ob* mice.
270 However, more than half of all the starvation-responsive nodes (587 out of 1144;
271 51.3%) exhibited a common response in the enzyme_mRNA layer ("enzyme_mRNA"
272 in Fig. 3**B**). This disconnection between the responses at the mRNA and protein levels
273 indicated that the protein abundance of the metabolic enzymes is determined processes
274 occurring after transcription, such as the rate of translation and protein degradation, that
275 are known to be downregulated in *ob*/*ob* mice (*59*, *60*). Among most of the nodes and
276 edges related to phosphorylation ("kinase_protein", "kinase_PTM", "kinase_activity",
277 and "enzyme_PTM" in Fig. 3**B**), WT-specific groups occurred most often compared to
278 the common, *ob*/*ob*-specific, and opposite groups. These results suggested a decrease in
279 regulation by phosphorylation in response to starvation in *ob*/*ob* mice.
280 Although regulatory connections from metabolites, lipids, enzyme_protein, and
281 enzyme_PTM contain a small portion of commonly responsive regulatory connections,
282 most of the starvation-responsive metabolic reactions ("metabolic reaction" in Fig. 3**B**)
283 were commonly responsive in both WT and to *ob*/*ob* mice (493 out of 702).
284 Compared with nodes in the other classes of responses, nodes with common
285 responses were most abundant in several layers related to transport_activities ("plasma
286 metabolite", "transporter_mRNA", "transporter_protein", and "transport_activity" in
287 Fig. 3**B**).

288 Taken together, the regulatory connections from metabolite, lipid,
289 enzyme_protein, and enzyme_PTM layers to metabolic reactions were different
290 between WT and *ob/ob* mice. Disconnections between the responses of enzyme_mRNA
291 and enzyme_protein were observed in *ob/ob* mice, probably due to the disrupted protein
292 translation and degradation, while the transport activities were maintained.

Structural properties of the starvation-responsive metabolic network

We focused on the sub-network of the global starvation-responsive transomic network that directly regulate metabolic reactions, defined as the starvation-responsive metabolic network (Fig. 4). To visualize the differences between WT and *ob/ob* mice, we show the starvation-responsive metabolic network separately for WT (Fig. 4**A**) and *ob*/*ob* (Fig. 4**B**) mice. For each genotype, the networks include the layers for metabolite, lipid, FFA & acyls, enzyme_protein, and enzyme_PTM (Data File S6) and their regulatory relationship to the metabolic reaction layer (fig. S3**A**). The edges connecting metabolite, lipid, and FFA & acyls layers to the metabolic reaction layer represent their roles as substrates, products, and allosteric regulators of the metabolic reactions.

We analyzed the structural properties of the starvation-responsive metabolic networks in WT and *ob/ob* mice (Fig. 5). We calculated the number of edges connected to each node (called "degree") and then assessed the degree distribution of the network, by a log-log scatter plot (Fig. 5**A**). We found that nodes with large degree were rare, while nodes with small degree were abundant. This type of network is called a scale-free network, and nodes with large degree are called "hub", while nodes with small degree are called "leaf" (Fig. 5**B**). Degree distribution of a scale-free network can be approximated by a power-law (*32*, *43*, *61*) defined as:

$$n(k) \propto k^{-\gamma},$$

where $n(k)$ denotes the number of nodes with a degree of k, and γ is a constant called the scaling parameter. The scaling parameter represents the heterogeneity of the degree distribution (*62*) with a small scaling parameter representing a large heterogeneity of degree distribution of the network. From the calculated scaling parameter for each genotype's network, we found that the starvation-responsive network for WT and *ob/ob*

317 mice had a similar amount of heterogeneity in the degree distribution (Fig. 5**A**).
318 Because the calculated scaling parameters do not meet the strict definition of scale-free
319 network that should be $2 < \gamma < 3$ (*61*, *63*), we call the starvation-responsive metabolic
320 network as a scale-free-like network.

321 We defined the nodes that had a degree in the top 2% among the responsive
322 nodes in each genotype as hub nodes (Fig. 5**C** and **D**), that regulated multiple metabolic
323 pathways (fig. S4). We identified 20 hub nodes in the network of WT mice and 15 hub
324 nodes in the network of *ob*/*ob* mice (Fig. 5**C**, **D** and labeled on Fig. 4**A**, **B**). In WT
325 mice, 15 of the 20 were WT-specific (Fig. 4**A**; Fig. 5**C**). In *ob*/*ob* mice, 7 hub nodes out
326 of 15 were *ob*/*ob*-specific and 3 of the 7 were lipids (Fig. 4**B**; Fig. 5**D**). The hub nodes
327 with the highest degrees were ATP (degree >200) and AMP (degree >100) in the
328 network of WT mice (Fig. 5**C**); whereas all hub nodes in the network of *ob*/*ob* mice had
329 degrees less than 100 with reduced glutathione (degree 81) and NADH (degree 69) (Fig.
330 5**D**). Thus, the starvation-responsive metabolic network in *ob/ob* mice lacked the most
331 highly connected hub nodes such as ATP and AMP. The number of edges from the 15
332 WT-specific hub nodes was 955 out of 2,318 edges (41%) in the starvation-responsive
333 metabolic network in WT mice (Fig. 5**E**), suggesting a large contribution of WT-
334 specific hub nodes to the starvation-responsive metabolic network of WT mice, which
335 was lost in *ob*/*ob* mice.

336 To evaluate the effect of the loss of responsiveness of the highly connected hub
337 nodes in *ob/ob* mice, we analyzed the structural properties of the starvation-responsive
338 metabolic network: the relative size of the largest cluster (Fig. 5**F**) and average path
339 length (Fig. 5**G**). Cluster is a set of nodes connected through edges regardless of the
340 distances. The largest cluster is the cluster that includes the largest number of nodes in a

341 network. Fragmentation breaks the network into isolated clusters and reduce the relative
342 size of the largest cluster (Fig. 5**F**), that is the number of nodes in the largest cluster
343 divided by the total number of the responsive nodes in each genotype. Average path
344 length (Fig. 5**G**) is the average number of edges connecting two edges, which increases
345 by loss of communicability among nodes (*64*). In the starvation-responsive metabolic
346 networks of WT and *ob*/*ob* mice, the relative sizes of the largest cluster were similar
347 (Fig. 5**H**), indicating that the network was not fragmentated in *ob*/*ob* mice. Additionally,
348 the average path lengths were significantly different but almost similar in the networks
349 of the WT and *ob*/*ob* mice (Fig. 5**I**), indicating that communicability was almost
350 maintained in *ob*/*ob* mice. Collectively, all structural properties of the starvation-
351 responsive metabolic networks, the scaling parameter (Fig. 5**A**), the relative size of the
352 largest cluster (Fig. 5**H**), and the average path length (Fig. 5**I**) were similar between WT
353 and *ob*/*ob* mice. These results indicated that the starvation-responsive metabolic
354 network was structurally maintained in *ob*/*ob* mice, despite the loss of responsiveness of
355 highly connected hub nodes such as ATP and AMP.

356 The maintenance of the structural properties of the starvation-responsive
357 metabolic network in *ob*/*ob* mice seems counter-intuitive because it has been known
358 that the loss of hub nodes in a scale-free network drastically alter the structural
359 properties (*64*). Taking a close look at the degree distribution (Fig. 5**A** and fig. S5), the
360 number of nodes (y-axis of Fig. 5**A**) with small degree (log10-transformed degree < 0.5
361 in the x-axis of Fig. 5**A**) were smaller in *ob*/*ob* mice than in WT mice, but the number of
362 nodes (y-axis of Fig. 5**A**) with log10-transformed degree ranging from 0.5 to 2 (x-axis
363 of Fig. 5**A**) were comparable between WT and *ob*/*ob* mice (Fig. 5**A**, see fig. S5 in
364 detail). Specifically, the percentage of nodes among the responsive nodes was higher in

365 *ob*/*ob* mice than WT mice for nodes with a log10-transformed degree between 0.5 and 1
366 (fig. S5**G**) and between 1 and 1.5 (fig. S5**H**). Totally, the percentages of nodes with
367 relatively large degrees (log10-transformed degree > 1) were similar between WT and
368 *ob*/*ob* mice (fig. S5**K**). The maintenance of nodes with relatively large degrees could
369 maintain the structural properties of the starvation-responsive metabolic network in
370 *ob*/*ob* mice.

371 To experimentally evaluate the effects of the loss of the responsiveness of ATP
372 and AMP in *ob*/*ob* mice, we measured the phosphorylation of Ampk, which reflect its
373 kinase activity, by western blotting. Ampk activity is known to depend on the AMP/ATP
374 ratio (*65*), that was WT-specifically responsive in our dataset (Fig. 5**J**). Starvation-
375 responsive phosphorylation of Ampk in *ob*/*ob* mice was weaker than in WT mice (Fig.
376 5**K**, and **L**), although significant responses were observed in both WT and *ob*/*ob* mice.
377 This weak response of Ampk in *ob*/*ob* mice could be due to an aberrantly large decrease
378 of phosphorylation ratio of Akt (Fig. 5**K**, and **L**), a negative regulator of Ampk (*66*).
379 Taken together, the loss of AMP/ATP responsiveness reduced the response of Ampk
380 activity, although it was partially rescued by the larger of Akt activity.
381

Temporal order of the starvation-responsive metabolic network in WT mice and its disruption in *ob*/*ob* mice

Adaptation to starvation is a temporally well-ordered metabolic process (*1–6*). To explore the relationships between the network structure and the temporal order of the starvation-induced changes in the starvation-responsive metabolic network, we defined the time when the response reached half of the maximum amplitude of the responses as *t*-half (*37*). A small *t*-half represents rapid responsiveness, and a large *t*-half represents slow responsiveness. We analyzed molecules [metabolites, lipids, FFA & acyls, proteins (enzyme_protein), and phosphorylation events (enzyme_PTM)] in the starvation-responsive metabolic networks, because *t*-half can be defined only for measured molecules not for metabolic reactions. We refer to hub nodes (Fig. 5**C** and **D**) as hub molecules because all the hub nodes were molecules.

We investigated the relationships between network structure and *t*-half in WT and *ob*/*ob* mice. We found a negative correlation between *t*-half and degree of molecules in WT mice (Fig. 6**A**), indicating that the molecules connected with many edges responded rapidly to starvation. In addition, 9 out of 20 hub molecules, including ATP, were essential for the negative correlation with *t*-half in WT mice (fig. S6~~, see Methods~~), suggesting a dominant role of hub molecules in coordinating the temporal order of the starvation-responsive metabolic network. By contrast, no significant correlation between *t*-half and degree of molecules was observed in *ob*/*ob* mice (Fig. 6**B**). Indeed, molecules with many edges, either increased or decreased, responded to starvation more rapidly than those with few edges in WT mice (Fig. 6**A**), but not in *ob*/*ob* mice (Fig. 6**B**). The *t*-half values of *ob*/*ob*-specific hub molecules were larger

405 than those of WT-specific hub molecules (Fig. 6**C**), indicating a slower response of the
406 *ob*/*ob*-specific hub molecules.

407 We conducted *t*-half analysis to evaluate how the temporal order of use of the
408 metabolic fuels such as glycogen, carbohydrates, amino acids and lipids (*1–6*), differs
409 during starvation in WT and *ob/ob* mice. We classified molecules into the following
410 metabolic pathways: "Starch and sucrose metabolism" (containing glycogen and
411 glycogen metabolic enzymes), "Glycolysis/gluconeogenesis", "Arginine biosynthesis"
412 (containing the urea cycle that could indicate amino acid degradation), and "Fatty acid
413 degradation" of the KEGG database (*55–57*). We compared *t*-half values for the
414 molecules in each of the metabolic pathways for the starvation-responsive metabolic
415 network in WT (Fig. 6**D**) and *ob*/*ob* mice (Fig. 6**E**). In WT mice, we observed
416 significant differences in *t*-half values of molecules among the investigated metabolic
417 pathways (Fig. 6**D**), indicating that the metabolic processes are temporally ordered
418 across the metabolic pathways in WT mice. Among them, "Fatty acid degradation"
419 responded to starvation the slowest, which is consistent with fatty acids as fuel for the
420 late stage of starvation (*1–6*). By contrast, no significant differences in *t*-half values
421 were observed in *ob*/*ob* mice (Fig. 6**E**), indicating that the temporal order among the
422 metabolic pathways was disrupted in *ob*/*ob* mice.

423 To examine which metabolic pathways largely contribute to the disturbed
424 temporal order among metabolic pathways in *ob*/*ob* mice, we compared the *t*-half values
425 between WT and *ob*/*ob* mice for each metabolic pathway (Fig. 6**F**).

426 We found that *t*-half values were significantly smaller in "Fatty acid
427 degradation" of *ob*/*ob* mice than WT mice. "Fatty acid degradation" degrades fatty acids
428 to ketone body (3-Hydroxybutyrate) through acyl-CoAs and acyl-carnitines during

429 starvation (fig. S7**A**).We manually reconstructed major metabolic reactions for fatty
430 acid degradation based on "Fatty acid degradation" (mmu00071), "Propanoate
431 metabolism" (mmu00640), and "Butanoate metabolism" (mmu00650) in KEGG
432 database (*55–57*), and found that many metabolic enzymes (enzyme_protein and
433 enzyme_PTM) and allosteric regulators regulate the fatty acid degradation (fig. S7**B**).
434 Among substrates (fatty acids), intermediates (acyl-CoAs and acyl-carnitines), products
435 (3-Hydroxybutyrate, a ketone body), and regulators (metabolites, enzyme_protein, and
436 enzyme_PTM), only the *t*-half values of acyl-CoAs showed statistically significant
437 differences between WT and *ob*/*ob* mice (fig. S7**C**), suggesting that the significant
438 difference in *t*-half values between WT and *ob*/*ob* mice (Fig. 6**F**) was mainly due to
439 acyl-CoAs. Acyl-CoAs increased smoothly and continuously in WT mice, but showed a
440 transient increase in the early phase of starvation in *ob*/*ob* mice (figs. S7**A** and **B**).
441 Although the difference in *t*-half values between WT and *ob*/*ob* mice was not
442 statistically significant, acyl-carnitines showed time courses similar to those of acyl-
443 CoAs (figs. S7**A** and **B**). By contrast, fatty acids, the source of acyl-CoAs and acyl-
444 carnitines, showed similar time courses between WT and *ob*/*ob* mice. This
445 disconnection in the time courses between substrates (fatty acids) and intermediate
446 (acyl-CoAs and acyl-carnitines) in fatty acid degradation could be a hallmark of
447 disrupted flux in fatty acid degradation.
448 This disruption could be due to the enzyme_protein because the number of
449 responsive enzyme_protein is the largest among substrates, intermediates, products, and
450 regulators in WT mice, and this number largely decreased in *ob*/*ob* mice (fig. S7**D**).
451 However, most enzyme_mRNA corresponding to these enzyme_protein were
452 commonly responsive in both WT and *ob*/*ob* mice (11 out of 13, fig. S7**B**). This

453 disconnection between responses at the mRNA and protein levels could be due to the
454 decreased rate of protein translation and degradation in *ob*/*ob* mice (Fig. 3**B**) (*59*, *60*).
455 Consistently, the correlations between the time courses of enzyme_mRNA and
456 enzyme_protein for each metabolic enzyme in fatty acid degradation were significantly
457 decreased in *ob*/*ob* mice (fig. S7**E**). To further validate this hypothesis, we evaluated the
458 protein phosphorylation related to protein translational (fig. S8**A** and **B**) and autophagic
459 (fig. S8**C** and **D**) activities. Phosphorylation of eIF2α represents inhibition of translation
460 (*67*). Phosphorylation ratio of eIF2α increased in *ob*/*ob* mice before starvation (fig. S8**A**
461 and **B**), suggesting translational deficiency in *ob*/*ob* mice, consistent with the previous
462 report (*60*). Although measuring autophagic activity in vivo without an exogenous
463 probe remains challenging (*68*), phosphorylation of p62 at Ser^{351} is an autophagic
464 substrate (*69*) and can serve as a marker for autophagic degradation. Phosphorylated
465 p62 significantly decreased in WT mice during starvation, but not in *ob*/*ob* mice (fig.
466 S8**C** and **D**), suggesting autophagy deficiency in *ob*/*ob* mice, consistent with the
467 previous report (*59*). Taken together, deficiency in protein translation and degradation in
468 *ob*/*ob* mice (fig. S8) reduced the number of responsive enzyme_protein in *ob*/*ob* mice
469 (fig. S7) and disrupted the flux of fatty acid degradation, reslting in a transient increase
470 in acyl-CoAs and acyl-carnitines during starvation in *ob*/*ob* mice (figs. S7**A** and **B**).
471 In addition, we compared *t*-half values of molecules in each omic layer in the
472 starvation-responsive metabolic network in WT (Fig. 6**G**) and *ob*/*ob* mice (Fig. 6**H**). In
473 WT mice, we observed significant differences in *t*-half values of molecules among the
474 omics layers (Fig. 6**G**), indicating that adaptation to starvation is temporally ordered
475 across omic layers in WT mice. Metabolites responded to starvation fastest, indicating
476 that metabolic reactions are initially regulated by metabolites through the effect of

477 starvation-induced changes in substrates and products and metabolite-mediated
478 allosteric regulators. Phosphorylation (enzyme_PTM), protein abundance
479 (enzyme_protein), and lipids responded next. The FFA & acyls layer responded the
480 slowest, consistent with fatty acid degradation important for the late stages of adaptation
481 to starvation (*3*). By contrast, no significant differences in *t*-half values were observed
482 in *ob*/*ob* mice (Fig. 6**H**), indicating that the temporal order of the starvation response by
483 the omic layers was disrupted.
484 Taken together, these results indicated that hub molecules coordinate the
485 temporal order of the responses of molecules, metabolic pathways, and omic layers in
486 the starvation-responsive metabolic network in WT mice. In *ob*/*ob* mice, the temporal
487 order of the starvation response throughout the network was disrupted. Deficiency in
488 protein translation and degradation in *ob*/*ob* mice (Fig. 3**B**, and fig. S7**E** and S8) (*59*,
489 *60*) also disturbed the fatty acid degradation (fig. S7).
490

491 **Co-regulation among molecules in the starvation-responsive metabolic network**
492 **and disruption in *ob*/*ob* mice**
493 Molecules positively or negatively regulated by common regulatory mechanisms show
494 positively or negatively correlated time courses, defined as co-regulation (Fig. 7**A**).
495 Thus, positively or negatively correlated time courses represent co-regulations, which
496 could be disrupted by the disrupted temporal order of metabolites, lipids, FFA & acyls,
497 protein abundance, and phosphorylation events in *ob*/*ob* mice (Fig. 6). As an index of
498 temporal co-regulation (Fig. 7**A**), we calculated the pairwise Pearson's correlation
499 coefficients for time courses of each pair of molecules (including phosphorylation
500 events) in the starvation-responsive metabolic network in WT and *ob*/*ob* mice,
501 respectively (Fig. 7**B**). The distribution of correlation coefficients in WT mice was
502 bimodal with peaks at around 0.75 and -0.75, indicating both positive or negative co-
503 regulation occurred among molecules. By contrast, the distribution of correlation
504 coefficients was unimodal with a broad peak around 0 in *ob*/*ob* mice, indicating that co-
505 regulation was disrupted in *ob*/*ob* mice.
506 We evaluated the extent of disruption of co-regulations among molecules in
507 *ob*/*ob* mice in each metabolic pathway (Fig. 7**C**). We compared the absolute values of
508 pairwise Pearson's correlation coefficients for the time courses of each pair of
509 molecules (including phosphorylation events) in each metabolic pathway in the
510 starvation-responsive metabolic network between WT and *ob*/*ob* mice (Fig. 7**C**). We
511 found statistically significant ($Q < 0.1$) decrease in the absolute values of pairwise
512 Pearson's correlation coefficients in *ob*/*ob* mice compared to WT mice, in all the
513 investigated metabolic pathways except for "Starch and sucrose metabolism". This
514 suggests that the extent of disruption in co-regulations in *ob*/*ob* mice was so substantial,

515 leading to disrupted co-regulation even among the molecules in the same metabolic
516 pathways.

517 To examine the detailed disruptions in each metabolic pathway, we manually
518 reconstructed major metabolic reactions for glycolysis/gluconeogenesis (fig. S9) and the
519 urea cycle (fig. S10) based on "Glycolysis/gluconeogenesis" and "Arginine
520 biosynthesis" in KEGG database (*55–57*), respectively. We focused on these pathways
521 because the pairwise Pearson's correlation coefficients among molecules in
522 "Glycolysis/gluconeogenesis" and "Arginine biosynthesis" (including urea cycle)
523 significantly decreased in *ob*/*ob* mice (Fig. 7**C**). Consistent with the disrupted *t*-half
524 values in the manually reconstructed map of fatty acid degradation (fig. S7C), the
525 pairwise Pearson's correlation coefficients in "Fatty acid degradation" also significantly
526 decreased in *ob*/*ob* mice (Fig. 7**C**).

527 We manually reconstructed major metabolic reactions for
528 glycolysis/gluconeogenesis based on "Glycolysis/gluconeogenesis" (mmu00010) in
529 KEGG database (*55–57*) for WT (fig. S9**A**) and *ob*/*ob* mice (fig. S9**B**). We counted the
530 number of edges from each regulator and found that ATP and AMP regulate various
531 metabolic reactions in glycolysis/gluconeogenesis in WT mice (fig. S9**A**, and **C**), while
532 molecules with fewer edges than ATP and AMP regulate the metabolic reactions in
533 glycolysis/gluconeogenesis in *ob*/*ob* mice (fig. S9**B**, and **D**). We assessed the degree
534 distribution of the network by a log-log scatter plot and found that degree distribution
535 was similar between WT and *ob*/*ob* mice (fig. S9**E**) in glycolysis/gluconeogenesis,
536 consistent with the case of the whole starvation-responsive metabolic network (Fig.
537 5**A**). We assessed the temporal order of the starvation-responsive metabolic network in
538 glycolysis/gluconeogenesis by comparing the *t*-half and degree of responsive molecules

539 (figs. S9**F** and **G**). Although it was not statistically significant, we found a weak
540 negative correlation between *t*-half and the degree of responsive molecules in
541 glycolysis/gluconeogenesis of WT mice (figs. S9**F**), indicating that the molecules
542 connected with many edges responded rapidly to starvation (*t*-half values of nodes with
543 log10-transformed degree more than 0.6 were small). By contrast, the correlation
544 coefficient between *t*-half and the degree of molecules was slightly positive in *ob*/*ob*
545 mice (fig. S9**G**), suggesting that the temporal order of the molecules was disrupted in
546 *ob*/*ob* mice. We also calculated the pairwise Pearson's correlation coefficients for time
547 courses of each pair of molecules (including phosphorylation events) in
548 glycolysis/gluconeogenesis in WT and *ob*/*ob* mice (fig. S9**H**). Consistent with the case
549 of the whole starvation-responsive metabolic network (Fig. 7**B**), the distribution of
550 correlation coefficients in WT mice was bimodal with peaks at around 1 and -0.75,
551 indicating that both positive or negative co-regulation occurred among molecules. By
552 contrast, the distribution of correlation coefficients was unimodal with a broad peak
553 around 0 in *ob*/*ob* mice, suggesting that co-regulation was disrupted in *ob*/*ob* mice.
554 Taken together, the starvation-responsive metabolic network in
555 glycolysis/gluconeogenesis is regulated by highly connected hub molecules such as ATP
556 and AMP in WT mice, but by molecules connected with fewer edges than ATP or AMP
557 in *ob*/*ob* mice (figs. S9**C** and **D**). The network was structurally robust (fig. S9**E**) but
558 temporally vulnerable (figs. S9**F**, **G**, and **H**) in liver of WT and *ob*/*ob* mice.
559 We manually reconstructed major metabolic reactions for urea cycle based on
560 "Arginine biosynthesis" (mmu00220) in KEGG database (*55–57*) (fig. S10**A**). We
561 counted the number of edges from each regulator in WT (figs. S10**B)** and *ob*/*ob* (fig.
562 S10**C**) mice. We found that Glu and ATP, both of which were WT-specific hub nodes in

563 the starvation-responsive metabolic network (Fig. 5**C**), regulated various metabolic
564 reactions in WT mice (fig. S10**B**). In *ob*/*ob* mice, succinate, an *ob*/*ob*-specific hub node
565 in the starvation-responsive metabolic network (Fig. 5**D**), and citrulline regulated
566 various metabolic reactions in *ob*/*ob* mice (fig. S10**C**). We assessed the degree
567 distribution of the network by a log-log scatter plot and calculated the scaling
568 parameters in WT and *ob*/*ob* mice (fig. S10**D**). In contrast to the case of the whole
569 starvation-responsive metabolic network (Fig. 5**A**) and glycolysis/gluconeogenesis (fig.
570 S9**E**), we found that the scaling parameter in *ob*/*ob* mice was smaller than that in WT
571 mice (fig. S10**D**), suggesting that the degree distribution was altered and the proportion
572 of nodes connected with many edges relatively increased in *ob*/*ob* mice. This result
573 suggests that the structure of the starvation-responsive metabolic network was altered in
574 urea cycle of *ob*/*ob* mice. We assessed the temporal order of the starvation-responsive
575 metabolic network in urea cycle by comparing the *t*-half and the degree of responsive
576 molecules (figs. S10**E** and **F**). We found a significant negative correlation between *t*-
577 half and the degree of molecules in WT mice (fig. S10**E**), indicating that the molecules
578 connected with many edges responded rapidly to starvation in urea cycle. By contrast,
579 this significant correlation between *t*-half and the degree of molecules was lost in *ob*/*ob*
580 mice (fig. S10**F**), suggesting that the temporal order of the molecules was disrupted in
581 *ob*/*ob* mice. We also calculated the pairwise Pearson's correlation coefficients for time
582 courses of each pair of molecules (including phosphorylation events) in urea cycle in
583 WT and *ob*/*ob* mice, respectively (fig. S10**G**). The distribution of correlation
584 coefficients in WT mice was bimodal with peaks at around 1 and -0.6, indicating both
585 positive and negative co-regulation occurred among molecules in urea cycle. The
586 distribution of correlation coefficients in *ob*/*ob* mice was also bimodal but the peaks of

587 the distribution were at around 0.5 and -0.3, suggesting that co-regulation among
588 molecules was disrupted in *ob*/*ob* mice. Taken together, the starvation-responsive
589 metabolic network in urea cycle was both structurally and temporally altered in *ob*/*ob*
590 mice, suggesting the severe disruption of amino acid metabolism in *ob*/*ob* mice.

591 It should be noted that the distribution of correlation coefficients (Fig. 7**B**)
592 could also be affected by the threshold for significance of the responses to starvation,
593 because the distribution of correlation coefficient among time courses of all measured
594 molecules was unimodal both in WT and *ob*/*ob* mice (fig. S11).

595 To obtain a qualitative landscape of co-regulations at a molecular level, we
596 constructed networks of molecules that exhibited strong co-regulations (the absolute
597 value of Pearson's correlation coefficient > 0.9, see fig. S12) among metabolites, lipids,
598 FFA & acyls, enzyme_protein, and enzyme_PTM in WT mice (Fig. 7**D**) and *ob/ob* mice
599 (Fig. 7**E**), named as the correlation metabolic network (Data File S7). Note that the
600 correlation metabolic network is data-dependent and the network structure highly
601 depends on the threshold for the absolute value of correlation coefficient (fig. S12).

602 The correlation metabolic network in WT mice included a single large cluster
603 comprised of 275 molecules, representing molecules with various biological functions
604 such as carbohydrate metabolism and fatty acid degradation (Fig. 7**D**), indicating that
605 most of the responsive molecules in WT mice are co-regulated. ATP and AMP, the rapid
606 hub molecules in the starvation-responsive metabolic network (Fig. 5 and 6) were
607 included in the large cluster, possibly suggesting that ATP and AMP formed this large
608 cluster by regulating the large number of metabolic reactions. By contrast, the network
609 in *ob*/*ob* mice was fragmentated with some clusters containing functionally related

610 molecules (Fig. 7**E**). Taken together, temporal co-regulation of metabolism in response

611 to starvation was disrupted in the *ob/ob* mice.

612 **Functional analysis of transcriptomic and proteomic data for potential clinical**
613 **application**

614 Dietary restriction, including caloric restriction (reducing total calorie intake) and
615 intermittent fasting (setting fasting periods in daily life with or without reducing the
616 total calorie intake), extends lifespan and improves health in multiple species (*6*, *31*, *70*,
617 *71*). However, obesity cancels the effects of intermittent fasting, that is a permissive
618 form of dietary restriction considering the compliance, to extend lifespan (*31*).
619 Investigating a therapeutic target to treat the negative effects of obesity on intermittent
620 fasting is clinically important. To achieve this, comprehensive and unbiased
621 measurements are necessary, because manually measured phenotypic traits failed to
622 explain 61% of the diet to lifespan covariance (*31*). Intermittent fasting, a long-term and
623 repetitive form of starvation, is expected to include the cumulative effects of short-term
624 starvation up to 24 hours. Thus, analyzing our omics data on short-term starvation is
625 valuable, particularly to reveal the differences of starvation-induced changes between
626 WT and *ob*/*ob* mice. Since metabolic traits associated with lean tissue mass explained
627 only 3.8% of the lifespan covariance (*31*), we focused on general functions of liver
628 using our transcriptomic and proteomic data, rather than on metabolism. In addition, we
629 used MSigDB (*72*), a more generalized database than KEGG (*55–57*).

630 To functionally characterize the starvation-responsive transcripts, we conducted
631 an enrichment analysis of significantly changed (either increased or decreased)
632 transcripts in WT and *ob*/*ob* mice (Fig. 8**A** and table Data File S8). Hallmarks, which
633 are categories of molecules in MSigDB (*72*), related to immune responses, such as
634 TNFA_SIGNALING_VIA_NFKB, INTERFERON_ALPHA_RESPONSE, and
635 INTERFERON_GAMMA_RESPONSE; metabolism such as

636 CHOLESTEROL_HOMEOSTASIS, FATTY_ACID_METABOLISM, and
637 PEROXISOME; stress responses such as HYPOXIA, APOPTOSIS, and
638 UNFOLDED_PROTEIN_RESPONSE; and cellular signaling such as
639 MTORC1_SIGNALING, P53_PATHWAY, and KRAS_SIGNALING_DN were
640 identified as commonly enriched hallmarks in both WT and *ob*/*ob* mice (Fig. 8**A** and
641 Data File S8). Hallmarks such as ESTROGEN_RESPONSES_EARLY,
642 ESTROGEN_RESPONSES_LATE, and GLYCOLYSIS were identified as WT-
643 specifically enriched hallmarks (Fig. 8**A** and Data File S8). MYC_TARGET_V1 and
644 MYC_target_V2 were identified as *ob*/*ob*-specifically enriched hallmarks (Fig. 8**A** and
645 Data File S8). The common enrichment of the hallmarks related to immune responses in
646 both WT and *ob*/*ob* mice suggest that the changes of the immune repertoire observed
647 with dietary restriction (*31*) also occurred with short-term fasting within 24 hours.
648 To functionally characterize the starvation-responsive proteins, we conducted
649 an enrichment analysis of significantly changed proteins in WT and *ob*/*ob* mice (Fig. 8**B**
650 and Data File S8). Hallmarks related to stress responses such as APOPTOSIS and
651 UNFOLDED_PROTEIN_RESPONSE; metabolism such as GLYCOLYSIS and
652 FATTY_ACID_METABOLISM; MTORC1_SIGNALING; and
653 OXIDATIVE_PHOSPHORYLATION were identified as WT-specifically enriched
654 hallmarks. MYC_TARGETS_V1 was identified as an *ob*/*ob*-specifically enriched
655 hallmark. No hallmark was commonly enriched in both WT and *ob*/*ob* mice, suggesting
656 that the responses to starvation are functionally distinct between both genotypes in
657 proteomic data.
658 Taken together, commonly enriched hallmarks were most abundant in
659 transcriptomic data, while WT-specifically responsive hallmarks were most abundant in

660 proteomic data, suggesting that the responses to starvation in WT and *ob*/*ob* mice were
661 functionally similar in the transcriptome, but totally different in the proteome. This
662 disconnection between responses at the mRNA and protein levels in *ob*/*ob* mice could
663 be due to deficiencies in protein translation and degradation in *ob*/*ob* mice (fig. S8).
664 Therefore, targeting deficiencies in protein translation and degradation could be a
665 potential therapeutic target to treat the insensitivity of intermittent fasting in obese mice
666 (*31*).
667

668 **Discussion**

669 We measured multiomic data during starvation in WT and *ob*/*ob* mice (Fig. 2) and
670 constructed a global starvation-responsive transomic network by integrating these data
671 (Fig. 3). We also showed that the starvation-responsive metabolic network (Fig. 4), a
672 sub network of the global starvation-responsive transomic network, is a scale-free-like
673 network. The hub molecules of the networks, regulating many metabolic reactions, were
674 energy indicators, such as ATP and AMP in WT mice, and less highly connected hub
675 molecules, such as lipids in *ob*/*ob* mice (Fig. 5). Despite the loss of the responsiveness
676 of the hub energy indicators in *ob*/*ob* mice, structural properties of the network in *ob*/*ob*
677 mice were maintained (Fig. 5), likely through the maintenance of nodes with relatively
678 large degrees (Fig. S5). By contrast, the temporal properties including the temporal
679 order (Fig. 6) and the temporal co-regulation of molecules were disrupted in *ob*/*ob* mice
680 (Fig. 7). Similar to the whole starvation-responsive metabolic network, the starvation
681 responsive metabolic network of glycolysis/gluconeogenesis in *ob*/*ob* mice was
682 structurally maintained but temporally disrupted compared to the network in WT mice
683 (fig. S9). However, the starvation-responsive metabolic network of urea cycle in *ob*/*ob*
684 mice was both structurally and temporally disrupted comparing to the network in WT
685 mice (fig. S10). In addition, we proposed a potential clinical target to treat the negative
686 effects of obesity on the intermittent fasting (Fig. 8).

687 The maintenance of the structural properties of the starvation-responsive
688 metabolic network in *ob*/*ob* mice (Fig. 5) suggests the robustness of the metabolic
689 networks against pathological perturbations. Robustness of the structural properties of
690 metabolic networks have also been investigated in cancers (*41*, *42*). Structural
691 properties of metabolic networks based on the tissue-specific gene expression were

692 similar between 15 cancers and corresponding normal tissues (*41*). Metabolic network
693 based on flux correlations showed similar structural properties between normal and
694 cancer tissues (*42*). These two studies suggest that structural properties of metabolic
695 networks in cancer are similar to those of normal tissues, despite profound differences
696 in gene expression patterns of cancer and non-cancer cells (*73*). These studies, together
697 with our results, indicate that structural properties of metabolic networks are robust
698 among various metabolic perturbations including starvation in healthy or obese
699 conditions and cancers.

700 By contrast to the robust structural properties (Fig. 5), temporal properties,
701 which were maintained depending on the hub molecules including energy indicators
702 such as ATP and AMP in WT mice, were disrupted in *ob*/*ob* mice (Figs. 6 and 7). These
703 results highlight the significance of the highly connected hub molecules for temporal
704 properties of the starvation-responsive metabolic networks. If a small number of hub
705 molecules regulate the entire network, nodes in the network would be uniformly
706 regulated, resulting in a temporally ordered and co-regulated network. Thus, the
707 starvation-responsive metabolic network is temporally disrupted in *ob*/*ob* mice, that lost
708 the responsiveness of the highly connected hub molecules such as ATP and AMP.

709 Structural and temporal properties of the starvation-responsive metabolic
710 network were evaluated for specific metabolic pathways, such as
711 glycolysis/gluconeogenesis (fig. S9) and urea cycle (fig. S10). The starvation-
712 responsive metabolic network of glycolysis/gluconeogenesis in *ob*/*ob* mice was
713 structurally maintained but temporally disrupted, consistent with the whole starvation-
714 responsive metabolic network (fig. S9). However, the starvation-responsive metabolic
715 network of urea cycle in *ob*/*ob* mice was disrupted both structurally and temporally (fig.

716 S10), suggesting a strong disruption of amino acid metabolism in *ob*/*ob* mice during
717 starvation. Amino acids during starvation are supplied by autophagy (*74*), a protein
718 degradation process that is disrupted in *ob*/*ob* mice (fig. S8**C** and **D**). Therefore, a
719 disrupted amino acid supply caused by autophagy deficiency could result in severely
720 disrupted amino acid metabolism during starvation in *ob*/*ob* mice.

721 If the metabolic network is temporally vulnerable, the structural robustness
722 observed in starvation (several hours) and cancers (~years) could be disrupted in a rapid
723 metabolic shift such as glucose ingestion (minutes) because of the lack of time for
724 rescuing the structural properties. Previously, we conducted a transomic analysis of liver
725 in WT and *ob*/*ob* mice during oral glucose ingestion, in which we measured
726 metabolome, lipidome, and transcriptome (*37*, *39*). Small fraction of the responsive
727 metabolites (15 out of 88, 17.0%) and transcripts (732 out of 5,091, 14.4%) was
728 commonly responsive in WT and *ob*/*ob* mice during oral glucose ingestion, while more
729 than one-third of the responsive molecules were commonly responsive during starvation
730 (Fig. 2) (*37*). Scaling parameters of the transomic networks, representing the
731 heterogeneity of the network, were different during oral glucose ingestion but similar
732 during starvation between WT and *ob*/*ob* mice (*39*). Taken together, glucose ingestion
733 requires distinct responsive molecules and heterogeneities of transomic network
734 between WT and *ob*/*ob* mice, suggesting metabolic network is more vulnerable to
735 temporally rapid perturbations (oral glucose ingestion) than slow (starvation) or chronic
736 (cancer) perturbations.

737 By evaluating the temporal order among omic layers during starvation (Fig. 6),
738 we found that metabolite layer was the fastest even compared to the enzyme_PTM
739 layer, which is composed of protein phosphorylation events (Fig. 6**G**). Our previous

740 study showed that rapid metabolic regulation by metabolites also occurs in the liver of
741 WT mice during oral glucose ingestion (*37*). However, we did not measure the
742 phosphoproteome in that study (*37*), thus we cannot ascertain if metabolite regulation
743 precedes phosphorylation-mediated regulation. Because here we measured both the
744 metabolome and phosphoproteome, our data indicated that metabolites take the
745 initiating role in controlling the transomic layers during starvation in liver.

746 One of the limitations of this study is the accuracy of the inference of regulator
747 activities, including TFs and protein kinases, and regulatory relationships from
748 metabolites, lipids, and FFA & acyls to metabolic reactions. For inference of TF activity,
749 we failed to identify Foxo1, which is master regulator of liver metabolism and is
750 necessary for upregulation of glucose production during starvation (*75*). We can explain
751 this discrepancy because we removed data for Foxo1 in liver from the data obtained
752 from the ChIP-Atlas database (*76*, *77*) as not meeting our quality check process for
753 inference input (see Methods). Another example, Creb1, which has been known to be
754 upregulated during starvation (*5*), was classified as a down-regulated TF (Table 5),
755 probably due to the failure of detection in phosphorylation, that is important for Creb1
756 activity (*5*). For kinase inference, we failed both mTorc1 and Ampk as responsive
757 protein kinases, both of which are known to be important for adaptation to starvation
758 (*78*, *79*). Indeed, phosphorylation of Ampk was confirmed in our dataset by western
759 blotting (Fig. 5**K** and **L**), but not our phosphoproteome data, suggesting insufficient
760 comprehensiveness and quantitative capacity of our phosphoproteome data. In addition,
761 protein kinases were identified for less than 5% of phosphorylation events at present
762 (*80*), thus the prediction algorithm could be inaccurate. For regulatory relationships
763 including those from metabolites, lipids, and FFA & acyls to metabolic reactions, we

764 identified regulatory relationships that could be extracted from existing databases. Thus,
765 unfamiliar or unknown regulatory relationships not registered in the databases we used
766 were not included in our study. These limitations originate from incomprehensiveness of
767 omics measurement (for example, lack of phosphorylated Creb1 and Ampk) and
768 database (for example, lack of Foxo1). These limitations could be partially solved by
769 recently developed techniques of measurements such as LiP-SMAP (*81*), PROMIS (*82*),
770 and MIDAS (*83*) for protein-metabolite (including lipids and FFA & acyls) interaction,
771 LiP-MS (*84*) for post-transcriptional regulations including phosphorylation, and
772 integrating recently developed bioinformatic tools such as CollectTRI-based database
773 (*85*), The Kinase Library (*86*), and OmniPath (*87*) to transomic analyses for algorithm,
774 but it is still challenging to approach these limitations especially in vivo at present.
775 Therefore, we need some breakthrough for accurate inferences of regulator activities.
776 Another limitation of our study is that we only used one model of obesity. By
777 only using *ob*/*ob* mice, we cannot exclude the possibility that the results are caused by
778 the effect of leptin deficiency (*88*). We compared our results with the previous study
779 using high fat diet (HFD) as a model for obesity (*30*). We observed similar changes in
780 metabolic enzymes and in glycogen during starvation in WT and *ob/ob* mice (fig. S1) as
781 were reported for both lean and HFD mice (*30*). Thus, our results are related to obesity
782 not leptin-deficiency itself.
783 In addition, our experimental condition is not optimized for dietary restriction,
784 because we focused on adaptation to starvation. Although we proposed that disturbed
785 protein translation and degradation are potential therapeutic targets to treat the negative
786 effects of obesity on intermittent fasting to extend lifespan (*31*), validation is needed in
787 studies focusing on dietary restriction under well-controlled experimental conditions.

Despite several limitations, our present study successfully described the global landscape of adaptation to starvation in WT and *ob*/*ob* mice and suggested that the highly connected hub energy indicators temporally coordinate the starvation-responsive metabolic network in the healthy condition and that these critical hubs are no longer starvation-responsive in obesity, resulting in temporal disruption of the starvation-responsive metabolic network. Robustness of the structures against pathological perturbations could be a general nature of metabolic networks, combining with the previous studies in cancer (*41*, *42*). Vulnerability of temporal properties of the network in *ob*/*ob* mice could be helpful to understand the pathology of adaptive responses to starvation in obesity.

798 **Materials and Methods**

799 **Mouse experiments**

800 All the animal experiments were conducted after approval by the animal ethics
801 committee of the University of Tokyo. Ten-week-old C57BL/6 WT and *ob*/*ob* male
802 mice were purchased from Japan SLC Inc. Mice were starved for 0, 2, 4, 6, 8, 12, 16, 24
803 hours, starting at approximately 18:00. For omic measurement, mice were euthanized
804 by cervical dislocation, blood was collected from retro-orbital sinus into tubes
805 containing 0.5 mg of EDTA, and liver was dissected and immediately frozen in liquid
806 nitrogen. Blood was centrifuged at 2,300 × *g* for 15 min at 4°C to separate plasma.
807 Plasma was frozen in liquid nitrogen and stored at -80°C. The frozen liver was crushed
808 with dry ice to a fine powder with a Wonder Blender (WB-1, OSAKA CHEMICAL
809 CO., LTD). Blood glucose was determined using ACCU-CHECK (Roche).

810

811 **Metabolomic analysis**

812 Metabolomic analysis was conducted as previously described (*37*). For liver, total
813 metabolites were extracted with methanol:chroloform:water (2.5:2.5:1) along with total
814 proteins. Approximately 40 mg of liver was homogenized in 500 µl of ice-cold
815 methanol containing internal standards [20 µM l-methionine sulfone (Wako), 2-
816 morpholinoethanesulfonic acid, monohydrate (Dojindo), and d-camphor-10-sulfonic
817 acid (Wako)] for normalization of peak intensities of mass spectrometry (MS) among
818 runs. Next, 500 µL of chloroform and then 200 µL of water were added and mixed.
819 After centrifugation at 4,600 × *g* for 15 min at 4ºC, the aqueous layer was filtered
820 through a 5 kDa cutoff filter (UFC3LCCNB-HMT, Human Metabolome Technologies)
821 to remove protein contamination. Simultaneously, proteins were precipitated from the

822 interphase and organic layers by addition of 800 μL of ice-cold methanol followed by
823 centrifugation at 12,000 × *g* for 15 min at 4ºC. The pellet was washed with 1 mL of ice-
824 cold 80% (v/v) methanol and resuspended in 500 μL water, followed by sonication with
825 Bioruptor (UCW-310, COSMO BIO). By addition of 500 μL of 2% SDS and 100 mM
826 Tris-HCl pH8.8, the pellet was lysed for 1 hour at 4°C with gentle mixing followed by
827 sonication using Handy Sonic (UR-20P, TOMY). The concentration of total protein was
828 determined with the bicinchoninic acid (BCA) assay (23227, Thermo Fisher Scientific)
829 and used for normalization of concentration among samples.

830 For plasma, 40 μL of the samples were used to extract metabolites with
831 methanol:chloroform:water (2.5:2.5:1). The samples were dissolved in 400 μL of ice-
832 cold methanol containing the internal standards [20 μM l-methionine sulfone (Wako), 2-
833 morpholinoethanesulfonic acid, monohydrate (Dojindo), and d-camphor-10-sulfonic
834 acid (Wako)], followed by addition of 400 μL of chloroform, and then 120 μL of water.
835 After centrifugation at 10,000 × *g* for 3 min at 4 ºC, the aqueous layer was filtered
836 through a 5 kDa cutoff filter (UFC3LCCNB-HMT, Human Metabolome Technologies)
837 to remove protein contamination.

838 The filtrate was lyophilized and suspended in 50 μL of water containing the
839 reference compounds [200 μM each of trimesate (206-03641, Wako) and 3-
840 aminopyrrolidine (404624, Sigma-Aldrich)]. Metabolites were quantified using an
841 Agilent 1600 Capillary Electrophoresis system (Agilent technologies), a G1603A
842 Agilent CE-MS adapter kit, and a G1607A Agilent CE electrospray ionization (ESI)–
843 MS sprayer kit. For cationic compounds, a fused silica capillary [50 μm internal
844 diameter (i.d.) × 100 cm] was used with 1 M formic acid as the electrolyte (*89*).
845 Methanol/water (50%, v/v) containing 0.01 μM hexakis (2,2-difluoroethoxy)

846 phosphazene was used as sheath liquid and delivered at 10 μl/min. ESI–time-of-flight
847 (TOF) MS was conducted in positive ion mode, and the capillary voltage was set to 4
848 kV. Each acquired spectrum was recalibrated automatically using the masses of the
849 reference standards [^{13}C isotopic ion of a protonated methanol dimer (2 MeOH + H)]$^{+}$,
850 mass/charge ratio (*m*/*z*) 66.0631 and [hexakis(2,2-difluoroethoxy)phosphazene + H]$^{+}$,
851 *m*/*z* 622.0290. For identification of metabolites, relative migration times of all peaks to
852 the reference compound 3-aminopyrrolidine were calculated, followed by comparison
853 of their *m*/*z* values and relative migration times to the metabolite standards. For
854 quantification of the metabolites, peak areas were compared to calibration curves
855 generated using internal standardization techniques with methionine sulfone. The other
856 parameters and conditions were the same as previously described (*90*). For anionic
857 metabolites, COSMO (+) (chemically coated with cationic polymer) capillary (50 μm
858 i.d. by 105 cm) (Nacalai Tesque, Kyoto, Japan) was used with a 50 mM ammonium
859 acetate solution (pH 8.5) as the electrolyte. Methanol/5 mM ammonium acetate (50%,
860 v/v) containing 0.01 μM hexakis (2,2-difluoroethoxy) phosphazene was used as sheath
861 liquid and delivered at 10 μl/min. ESI-TOFMS was conducted in negative ion mode,
862 and the capillary voltage was set to 3.5 kV. Trimesate and d-camphor-10-sulfonic acid
863 were used as the reference and the internal standards, respectively. The other parameters
864 and conditions were same as described previously (*91*). The Agilent MassHunter
865 software (Agilent technologies) was used for data analysis (*89–91*).
866 F1,6P and F2,6P were measured separately using IC-QEMS (*92*). A Dionex
867 IonPac AS11-HC-4 μm column (250 × 0.4 mm, 4 μm; Thermo Fisher Scientific) was
868 used at 35°C to separate metabolite. We used KOH as an eluent at the speed of 0.02
869 mL/min. The gradient was as follows: 1 mM from 0 to 2 min, 20 mM at 16 min, 100

870 mM at 35 min. As a sheath solution, isopropanol containing 0.1% acetic acid was used
871 at the speed of 5 μl/min. MS was performed in the ESI negative-ion mode. The
872 parameters were as follows: sheath gas, 20 (arbitrary units); auxiliary gas, 10 (arbitrary
873 units); spray voltage, 4.0 kV; capillary temperature, 300°C; S-lens, 50 (arbitrary units).
874 Data acquisition was conducted in full MS scan mode. Parameters of the scanning were
875 as follows: resolution, 70,000; auto-gain control target, 3×10^6; maximum ion injection
876 time, 100 ms; scan range, 70–1,000 *m*/*z*.
877
878 **Lipidomic analysis**
879 Liver samples were prepared for lipid extraction using the Bligh and Dyer's method
880 (*93*) with minor modifications. Briefly, the lipids and their related metabolites were
881 extracted from frozen and crushed liver tissues (~50 mg) with 1 ml of cold methanol.
882 The samples were vigorously mixed for 1 min and sonicated for 5 min. The extracts
883 were then centrifuged at 16,000 ×*g* for 5 min at 4°C, and the resultant supernatant was
884 collected. Protein concentrations in the pellet were determined using the bicinchoninic
885 acid (BCA) assay (23227, Thermo Fisher Scientific). The collected supernatant (180
886 μL) was mixed with 200 μL of chloroform, 150 μL of water, 10 μL of internal standard
887 (IS) A (Mouse SPLASH Lipidomix Mass Spec Standard, Avanti Polar Lipids Inc.,
888 Alabaster, AL, USA) containing 1.0 nmol phosphatidylcholine (PC) 15:0–18:1 (d_7),
889 0.070 nmol phosphatidylethanolamine (PE) 15:0–18:1 (d_7), 0.20 nmol
890 phosphatidylserine (PS) 15:0–18:1 (d_7), 0.050 nmol phosphatidylglycerol (PG) 15:0–
891 18:1 (d_7), 0.20 nmol phosphatidylinositol (PI) 15:0–18:1 (d_7), 0.10 nmol phosphatidic
892 acid (PA) 15:0–18:1 (d_7), 0.45 nmol lysophosphatidylcholine (LPC) 18:1 (d_7), 0.020
893 nmol lysophosphatidylethanolamine (LPE) 18:1 (d_7), 2.5 nmol cholesteryl ester (CE)

894 18:1 (d_7), 0.15 nmol diacylglycerol (DG) 15:0–18:1 (d_7), 0.35 nmol triacylglycerol (TG)
895 15:0–18:1 (d_7)–15:0, and 0.20 nmol sphingomyelin (SM) d18:1–18:1 (d_9), 10 μL of IS
896 B (Avanti Polar Lipids Inc.) containing 1.0 nmol monoacylglycerol (MG) 18:1 (d_7),
897 0.10 nmol ceramide (Cer) d18:1 (d_7)–15:0, 0.10 nmol hexosylceramide (HexCer) d18:1
898 (d_7)–18:1, 1.1 nmol free fatty acid (FA) 16:0 ($^{13}C_{16}$), and 3.0 nmol cholesterol (d_7), and
899 10 μL of IS C (Merck, Darmstadt, Germany) containing 0.40 nmol acylcoenzyme A
900 (acyl-CoA) 2:0 ($^{13}C^2$). The aqueous and organic layers were separated by vortexing and
901 subsequent centrifugation at 16,000 ×*g* and 4°C for 5 min.
902 The aqueous (upper) layer (250 μL) was transferred to a clean tube for analysis
903 by a liquid chromatography (Nexera X2 UHPLC system, Shimadzu Co., Kyoto, Japan)
904 with a metal-free peek-coated InertSustain C18 column (2.1 mm i.d. × 150 mm, 3 μm
905 particle size, GL Sciences Inc., Tokyo, Japan) coupled with a Q Exactive, high-
906 performance benchtop quadrupole Orbitrap high-resolution tandem mass spectrometer
907 (Thermo Fisher Scientific) (C18-LC/MS) for acyl-CoAs and acyl-carnitines (*94*). After
908 the aqueous layer extracts were evaporated under vacuum, dried extracts were stored at
909 −80°C until use for C18-LC/MS analysis. Prior to analysis, the dried aqueous layer was
910 reconstituted in 50 μL of water.
911 The organic (lower) layer (140 μL) was transferred to a clean tube for analysis
912 by supercritical fluid chromatography (SFC, Nexera UC system, Shimadzu Co.) with an
913 ACQUITY UPC^2 HSS C18 column (3.0 mm i.d. × 100 mm, 1.8 μm particle size,
914 Waters, Milford, MA, USA) coupled with a triple quadrupole mass spectrometry
915 (TQMS, LCMS-8060, Shimadzu Co.) (C18-SFC/MS/MS) for FAs, TGs, and CEs (*94*)
916 and an SFC (Shimadzu Co.) with a ACQUITY UPC2 Torus diethylamine (DEA) (3.0
917 mm i.d. × 100 mm, 1.7 μm particle size, Waters) coupled with a TQMS (DEA-

918 SFC/MS/MS) for PCs, PEs, PSs, PGs, PIs, PAs, LPCs, LPEs, MGs, DGs, SMs,
919 cholesterol, Cers, and HexCers (*94*, *95*). The liver lipid extract (140 μL) was diluted to a
920 final volume of 200 μL with a solution of methanol for C18-SFC/MS/MS and DEA-
921 SFC/MS/MS analysis.
922
923 **Transcriptomic analysis**
924 Total RNAs were extracted from approximately 10 mg of liver using RNeasy Mini Kit
925 (74106, QIAGEN) and QIAshredder (79656, QIAGEN). The amount and quality of
926 RNAs were assessed using Nanodrop (Thermo Fisher Scientific) and the 2100
927 Bioanalyzer (Agilent Technologies). The cDNA libraries were prepared using the
928 TruSeq Stranded mRNA Kit (Illumina, San Diego, CA, USA). The resulting cDNAs
929 were subjected to 150 base pair (bp) paired-end sequencing on an Illumina
930 NovaSeq6000 Platform (Illumina). Sequences were aligned to the reference genome of
931 mice derived from the Ensembl database (*96*, *97*) (GRCm38/mm10, Ensembl release
932 97) using the STAR software package (v.2.5.3a) (*98*). The RSEM tool (*99*) (v.1.3.0) was
933 used to estimate gene expression levels from the aligned sequences. Resultant read
934 counts were used as inputs for edgeR software (*49*). For other analyses, transcripts per
935 kilobase million (TPM) were used.
936
937 **Proteomic analysis**
938 Total proteins extracted during sample preparation of metabolomic analysis were
939 subjected to the following proteomic analysis. For standardization among runs of
940 measurement, proteins from frozen liver powder of Lys(6)-SILAC mice (Silantes) were
941 also extracted with methanol/chloroform extraction. Protein concentration of the lysates

942 was determined using the bicinchoninic acid (BCA) assay (23227, Thermo Fisher
943 Scientific) and calibrated to 1 mg/mL. Then, 50 μg each of non-labeled and labeled
944 lysates were mixed for peptide preparation. Cysteine residues were blocked by 2 mM
945 Tris (2-carboxyethyl) phosphine hydrochloride (TCEP) (Thermo Fisher Scientific) at
946 37°C for 30 min followed by alkylation with 10 mM 2-iodoacetamide (IAA) at room
947 temperature for 30 min. The proteins were precipitated with acetone for 3 hours at
948 −30°C and the resulting pellet was dispersed in 50 mM triethylammonium bicarbonate
949 by ultrasonic treatment (three times for 30 s with intervals of 30 s) with a Bioruptor
950 (Diagenode). The protein suspension was subjected to digestion with lysyl
951 endopeptidase (Wako) for 16 h at 37°C. Resulting peptides were centrifuged at 15,000 ×
952 *g* for 15 min at 4°C and subjected to C18-StageTip purification (*100*). Peptides were
953 resolved in 50 μL 3% acetonitrile (can)-0.1% foromic acid prior to MS analysis.
954 All samples were analyzed with Q Exactive HF-X (Thermo Fisher Scientific)
955 instrument equipped with an UltiMate 3000 RSLCnano LC System (Thermo Fisher
956 Scientific) via a nano-electrospray source with a column oven set at 50°C (AMR Inc.).
957 Peptides were directly injected onto a 75 μm × 25 cm PicoFrit emitter (New Objective,
958 Woburn, MA, USA) packed in-house with C18 core-shell particles (CAPCELL CORE
959 MP 2.7 μm, 160 Å material; Osaka Soda Co., Ltd., Osaka, Japan) with a linear gradient
960 of 7–42% B for 76 min, 42-80% B for 5 min, and 80% B for 9 min at a flow rate of 100
961 nL/min, where A is 0.1% formic acid and B is 0.1% formic acid and 80% acetonitrile.
962 MS data acquisition was performed in data-independent acquisition (DIA) mode. For
963 quantification in the DIA mode, MS1 spectra were collected in the range of *m*/*z* 423-865
964 at 60,000 resolution to set an AGC target of 3×10^6. For MS2 spectra, collections were
965 conducted in the range of > *m*/*z* 200 at 30,000 resolution to set an AGC target of 3 ×

966 10^6. The isolation width was configured to 8 Th with stepped normalized collision
967 energies of 20, and 23%. Through the optimization by Skyline 4.1 (*101*), isolation
968 window patterns in *m*/*z* 428-860 were used as window placements. In the DIA mode for
969 a spectral library, the pool of all samples was analyzed by using the above
970 measurements and the gas-phase fractionation method. In the gas-phase fraction
971 method, six MS ranges (*m*/*z* 426-502, 498-574, 570-646, 642-718, 714-790, and 786-
972 862) were used, and each was measured by overlapping DIA (*102*, *103*). MS1 spectra
973 were collected at 120,000 resolution to set an AGC target of 3×10^6. MS2 spectra were
974 collected in the range of > *m*/*z* 200 at 60,000 resolution to set an AGC target of 3×10^6.
975 The isolation width was set to 2 Th with stepped normalized collision energies of 20 and
976 23%. Isolation window patterns in the ranges of *m*/*z* 428-500, 500-572, 572-644, 644-
977 716, 716-788, and 788-860 were used as window placements optimized by Skyline 4.1.
978 The spectra library was generated by searching MS data in the library against
979 the mouse Ensembl release 97 database using Scaffold DIA (Proteome Software Inc.,
980 Portland OR, USA). The parameters were as follows: experimental data search enzyme,
981 LysC/P; maximum missed cleavage sites, 1; precursor mass tolerance, 6 ppm; fragment
982 mass tolerance, 8 ppm; and static modification, cysteine carbamidomethylation. The
983 threshold for identification of peptides was a peptide false discovery rate (FDR) < 1%.
984 To identify peptides derived from Lys(6)-SILAC mice, a library of identified peptides
985 with a mass increase 6.020129 Da on Lys was built and added to the library obtained
986 above. All raw data was processed with DIA-NN (ver. 1.8) using library search mode
987 using the following parameters: reannotation, Mus_musculus.GRCm38.97.pep.all.fa;
988 modification, UniMod188 (6.020129), and peak-translation. Using the output from
989 DIA-NN software, the SILAC ratios of all assigned fragment ion pairs were calculated,

990 and the median of the SILAC ratios of each protein was used for protein quantification.
991 Proteins assigned to a single ensemble gene ID were used in the following analyses. The
992 SILAC ratios of all the proteins were normalized by the median of the SILAC ratio in
993 each biological sample.
994
995 **Phosphoproteomic analysis**
996 Total proteins extracted during sample preparation of metabolomic analysis were
997 subjected to the following phosphoproteomic analysis. As described above, 2 mg of
998 protein solution was subjected to reduction and alkylation by TCEP and IAA,
999 respectively. Then, proteins were precipitated in three volumes of ice-cold acetone and
1000 centrifuged at 16,000 × *g* for 2 h. The pellet was rinsed with 90% acetone followed by
1001 digestion with 30 μg of trypsin in 600 μl of 100 mM ammonium bicarbonate for 16 h.
1002 Thirty-five μl of 10% trifluoroacetic acid (TFA) and 450 μl of ACN were added to the
1003 protein digests (1 mg/300 μl). The mixture was centrifuged at 16,000 × *g* and the
1004 supernatant was collected into a new tube. Phosphopeptides were enriched using Fe^{3+}-
1005 IMAC (*104*). NTA-agarose resin (1 mL) (Qiagen) was washed twice with 3 ml of
1006 distilled water and 2 ml of 100 mM $FeCl_3$ in 0.1% acetic acid was added. Following a
1007 wash with 2 ml of 0.1% TFA, 2% ACN and 0.1% TFA, 60% ACN, the resin was stored
1008 in 1 ml of 0.1% TFA, 60% ACN (Fe^{3+}-IMAC agarose resin). C18-StageTip (3M)
1009 packed with 75 μl of Fe^{3+}-IMAC agarose resin was equilibrated with 200 μl of 0.1%
1010 TFA, 60% ACN, then the protein digests were loaded onto the IMAC/C18-StageTip and
1011 the loaded system was washed twice with 200 μL of 0.1% TFA, 60% ACN. Following
1012 equilibration with 200 μl of 0.1% TFA, 2% ACN, 200 μl of 1% inorganic phosphate
1013 was added to elute phosphopeptides from the Fe^{3+}-IMAC agarose resin and bind them

1014 to the C18-StageTip. Following a wash with 200 μL of 0.1% TFA, 2% ACN, the
1015 peptides were eluted with 0.1% TFA, 60%ACN from the IMAC/C18-StageTip. The
1016 resulting peptides were dried, reconstituted in 3% ACN with 0.1% formic acid, and
1017 subjected to MS analysis.

1018 All samples were analyzed with Orbitrap Exploris 480 MS (Thermo Fisher
1019 Scientific) instrument equipped with an UltiMate 3000 RSLCnano LC System (Thermo
1020 Fisher Scientific) via a nano-electrospray source with a column oven set at 60°C (AMR
1021 Inc.). Peptides were directly applied onto a 75 μm × 120 mm column (Nikkyo Technos
1022 Co.,Ltd) with a linear gradient of 5–32% B for 70 min and 32-65% B for 10 min at a
1023 speed of 200 nL/min, where A is 0.1% formic acid and B is 0.1% formic acid and 80%
1024 acetonitrile.

1025 MS data were acquired in overlapping data-independent acquisition (DIA)
1026 mode (*102*, *103*). For quantification in the DIA mode, MS1 spectra were collected in the
1027 range of *m*/*z* 390-1010 at 30,000 resolution to set an AGC target of 3×10^6. MS2 spectra
1028 were collected in the range of > *m*/*z* 200 at 30,000 resolution to set an AGC target of 3 ×
1029 10^6, and stepped normalized collision energies of 22, 26, and 30%. The isolation width
1030 for MS2 was set to 10 Th and overlapping window patterns in *m*/*z* 400-1000 were used
1031 window placements optimized by Skyline v4.1 (*101*). In the DDA-MS mode for a
1032 spectral library, the pool of all samples was analyzed by using the gas-phase
1033 fractionation method with MS ranges of *m*/*z* 395-555, 545-705, 695-1005, and 390-
1034 1010. MS1 spectra were collected at 120,000 resolution to set an AGC target of 3×10^6.
1035 Within the MS ranges of *m*/*z* 395-555, 545-705, 695-1005, the 20 most intense ions with
1036 charge states of 2^+ to 5^+ more than 5.0×10^3 were fragmented by HCD with normalized
1037 collision energies of 22, 26, and 30%, and MS2 spectra were collected in the range of >

1038 *m*/*z* 200 at 60,000 resolution to set an AGC target of 5×10^5. Within the MS ranges of
1039 *m*/*z* 390-1010, the 40 most intense ions with charge states of 2^+ to 5^+ that exceeded $5.0 \times$
1040 10^3 were fragmented by HCD with normalized collision energies of 22, 26, and 30%,
1041 and MS2 spectra were collected in the range of > *m*/*z* 200 at 30,000 resolution to set an
1042 AGC target of 2×10^5.
1043 The spectra library was built by searching MS data in the library against the
1044 mouse Ensembl database (GRCm38/mm10, Ensembl release 97) using Proteome
1045 Discoverer v2.3 (Thermo Fisher Scientific). The setting parameters were as follows:
1046 Fragmentation, HCD; Precursor Tolerance, 8 ppm; Fragment Tolerance, 0.02 Da;
1047 Digestion Enzyme, Trypsin; Max Missed Cleavages, 1; Variable Modification, Phospho
1048 [S, T, Y]; Fixed Modification, Carbamidomethylation [C]; Site Probability Threshold,
1049 75; Peptide FDR, < 1%. Unique phosphopeptides were subjected to the following
1050 analyses. To determine phosphorylation at each phosphosite, the intensities of all signals
1051 of quantified phosphopeptides that include the phosphosite of interest were summed.
1052
1053 **Glycogen content assay**
1054 Glycogen content in liver was measured using Amplex Red Glucose/Glucose Oxidase
1055 Assay Kit glucose assay (Thermo Fisher Scientific) after digestion of glycogen to
1056 glucose (*37*, *105*). Approximately 20 mg of crushed tissue samples was incubated for 1
1057 hour at 95°C in 1 mL of 30% (w/v) KOH solution. The lysate (50 μL) was collected into
1058 another 1.5 mL tube and neutralized by 15.3 μL of glacial acetic acid. Total protein
1059 concentration of the liver digest was determined using the BCA assay (23227, Thermo
1060 Fisher Scientific) and the concentration of protein was adjusted to 1 μg/μL. Lipids were
1061 removed by the Bligh and Dyer method and glycogen was extracted. Ice-cold methanol

1062 (120 μL), 50 μL of chloroform, 10 μL 1% (w/v) of linear polyacrylamide, and 70 μL of
1063 water were added to the liver digest (50 μL) and mixed. The mixture was incubated for
1064 30 min on ice and centrifuged at 12,000 × *g* to remove the aqueous layer. The glycogen
1065 was precipitated by adding 200 μL of methanol, followed by centrifugation at 12,000 ×
1066 *g* for 30 min at 4°C. The pellet was washed with ice-cold 80% (v/v) methanol and dried
1067 completely. Glycogen pellets were resuspended in 20 μL of amyloglucosidase (0.1
1068 mg/mL; Sigma-Aldrich) in 50 mM sodium acetate buffer and incubated for 2 hours at
1069 55°C. The glycogen content was determined using the Amplex Red Glucose/Glucose
1070 Oxidase Assay Kit glucose assay (Thermo Fisher Scientific) following the
1071 manufacture's protocol.
1072
1073 **Western blotting analysis**
1074 Total proteins extracted during sample preparation of metabolomic analysis were boiled
1075 in sample buffer (58.28 mM Tirs-HCl, pH 6.8, 4.7% glycerol, 2.82% SDS, 6% β-
1076 Mercaptoethanol, and 0.0094% bromophenol blue). Samples were subsequently
1077 separated by SDS-PAGE followed by transfer to nitrocellulose membrane, and then
1078 immunoblotting was conducted using total Akt (#9272, Cell Signaling), phospho-Akt
1079 (Ser473) (#9271, Cell Signaling), total eIF2α (#9722, Cell Signaling), phospho-eIF2α
1080 (Ser51) (#9721, Cell Signaling), total Ampk (#2532, Cell Signaling), phospho-Ampk
1081 (Thr172) (#2531, Cell Signaling), total p62 (PM045, MBL), and phospho-p62 (PM074,
1082 MBL). A Peroxidase (HRP)-conjugated anti-rabbit antibody (NA9340V) was used as a
1083 secondary antibody. Immunodetection was performed using Immobilon Western
1084 Chemiluminescent HRP Substrate (Millipore) and signals were detected by a
1085 luminoimage analyzer (Fusion System Solo 7S; M&S Instruments Inc). Quantification

1086 and brightness adjustment were conducted with the Fiji software (ImageJ; National
1087 Institutes of Health). For the images with high background, we used the subtract
1088 background function in the Fiji software (*106*). Conversion of the images to 8-bit image
1089 was conducted by Photoshop CS6 (Adobe).
1090
1091 **Identification of starvation-responsive molecules**
1092 We analyzed molecules or phosphorylation events that were quantified in more than half
1093 of replicates in both WT and *ob*/*ob* mice at all the time points after food removal (Fig. 2
1094 and Fig. S1). For every molecule, one-way-ANOVA tests were conducted in data for
1095 WT or *ob*/*ob* mice. Molecules with $P < 0.025$ were defined as starvation-responsive
1096 molecules. False discovery rate (FDR) of the responsive molecules was less than 0.1
1097 except for phosphoproteome data (Table 1). FDR was calculated using the Storey's
1098 procedure (*107*) except for the lipidomic and FFA & acyls layers, including molecules
1099 in the lipid and FFAs & acyls layers. For lipidomic and FFA & acyls analyses,
1100 Benjamini-Hochberg procedure was conducted (*108*), because the number of measured
1101 molecules were small in these omic layers (16 for lipidome and 41 for FFA & acyls).
1102 For transcriptomic analysis, the likelihood ratio test in the edgeR package (version
1103 3.34.1) (*49*) of the R language (version 4.1.1) was used to identify significantly changed
1104 molecules during starvation. Mean time courses for each molecule in WT and *ob*/*ob*
1105 mice were log2-transformed relative to the geometric mean of the values of WT and
1106 *ob*/*ob* mice before food deprivation (0 h). Using these log2-transformed time courses,
1107 the area under the curve (AUC) was calculated as the area between the time course
1108 curves during starvation and the baseline value at 0 h (before food deprivation).
1109 Molecules with positive AUC and P value < 0.025 were defined as increased molecules,

1110 and molecules with negative AUC and *P* value < 0.025 were defined as decreased
1111 molecules.
1112
1113 **Pathway enrichment analysis**
1114 We conducted pathway enrichment analysis for increased or decreased transcripts
1115 (Table 3; Data File S3), proteins (Table 4; Data File S3), and phosphoproteins (Data File
1116 S3). From KEGG database (*55–57*), we extracted gene sets of pathways in
1117 "Metabolism", "Genetic Information Processing", "Environmental Information
1118 Processing", "Cellular Processes", and "Organismal Systems". Note that
1119 "Global/overview pathways" were removed. The enrichment of increased or decreased
1120 molecules in each pathway was determined using one-tailed Fisher's exact test followed
1121 by FDR correction by the Benjamini-Hochberg procedure (*108*). Transcripts, proteins,
1122 and phosphoproteins quantified in more than half of the replicates in WT and *ob*/*ob*
1123 mice were used as background. Pathways with *Q*-values < 0.1 were identified
1124 significantly enriched.
1125
1126 **Inference for activities of TFs**
1127 We inferred the TF activities using transcriptomic data and ChIP-Atlas (*76*, *77*) (Table
1128 5; Data File S4). ChIP-Atlas includes a database curating publicly available ChIP-seq
1129 experiments, that can be used for inference of the activities of TFs (*109*). The list for all
1130 the ChIP-seq experiments was downloaded (https://github.com/inutano/chip-
1131 atlas/wiki#downloads_doc) and all the experimental IDs of mm10 were extracted. We
1132 focused on the ChIP-seq experiments conducted using "liver" or "hepatocytes" in mice.
1133 Using this list of experimental IDs of mm10, we scraped "Target Genes" information

1134 that includes genes whose transcription start sites (TSSs) were identified as binding
1135 partners with the bait proteins (TFs) (https://chip-
1136 atlas.dbcls.jp/data/mm10/target/**Protein.Distance**.tsv). The "Distance" was set as 1 kb
1137 from TSS. We set the threshold for statistical significance of values calculated by peak-
1138 caller MACS2 as 50 and identified target genes for each ChIP-seq experiment. To keep
1139 quality of the inference, we removed ChIP-seq experiments that detected less than 50
1140 target genes. Through these processes, we obtained a network between bait proteins
1141 (TFs) for each ChIP-seq experiment and "Target Genes" with TSSs that were bound to
1142 the bait proteins (TFs). Note that this network is a network of ChIP-seq experiments and
1143 transcripts, not TFs and transcripts. In other words, ChIP-seq experiments for the
1144 identical TFs were not combined at this step.

1145 Using this network, we conducted TF enrichment analyses for increased or
1146 decreased transcripts during starvation in WT and *ob*/*ob* mice. The enrichment of
1147 increased or decreased transcripts in each ChIP-seq experiment was determined using
1148 one-tailed Fisher's exact test followed by FDR correction conducted by the Benjamini-
1149 Hochberg procedure (*108*). Transcripts quantified in more than half of the replicates in
1150 both WT and *ob*/*ob* mice were used as background. ChIP-seq experiments with *Q*-
1151 values less than 0.1 were identified as significantly enriched ChIP-seq experiments. TFs
1152 for which significant enrichment was observed in at least one ChIP-seq experiment were
1153 identified as candidate TFs that changed their activities during starvation.

1154 We further screened the candidate TFs to define the up-regulated or down-
1155 regulated TFs using transcriptomic, proteomic, and phosphoproteomic data. It should be
1156 noted that TFs that are registered as negative regulators in Transcriptional Repressor
1157 Complex (GO_0017053) were defined as negative regulators, and other TFs were

1158 regarded as activators in this study. If a transcriptional activator was enriched in
1159 increased transcripts, and any of the transcriptomic, proteomic, or phosphoproteomic
1160 data of the TF increased and none of the transcriptomic nor proteomic data decreased,
1161 the TF was identified as an up-regulated TF. If a transcriptional activator was enriched
1162 in decreased transcripts, and any of the transcriptomic, proteomic, or phospho-
1163 proteomic data of the TF decreased and none of the transcriptomic nor proteomic data
1164 increased, the TF was identified as a down-regulated TF. If a transcriptional inhibitor
1165 was enriched in increased transcripts, and any of the transcriptomic, proteomic, or
1166 phosphoproteomic data of the TF decreased and none of the transcriptomic nor
1167 proteomic data increased, the TF was identified as an up-regulated TF. If a
1168 transcriptional inhibitor was enriched in decreased transcripts, and any of the
1169 transcriptomic, proteomic, or phosphoproteomic data of the TF increased and none of
1170 the transcriptomic nor proteomic data decreased, the TF was identified as a down-
1171 regulated TF.
1172 Downstream genes of the inferred TFs were defined based on the gene
1173 regulatory network from the ChIP-Atlas database. For each up-regulated TF, increased
1174 transcripts whose TSS bind to the TF in at least one ChIP-experiment were defined as
1175 downstream transcripts of the TF. For each down-regulated TF, decreased transcripts
1176 whose TSS bind to the TF in at least one ChIP-experiment were defined as downstream
1177 transcripts of the TF.
1178
1179 **Inference for activities of protein kinases**
1180 We inferred the protein kinase activities using phosphoproteomic data and NetPhorest
1181 (*110*) (Table 6; Data File S4). We constructed a kinase regulatory network using

1182 NetPhorest (*110*), a protein sequence-based algorithm to infer kinase-substrate
1183 relationships. The inputs for NetPhorest were mouse protein sequences that were
1184 associated with ENSMUSP in FASTA format obtained from
1185 Mus_musculus.GRCm38.97.pep.all.fa in Ensembl database (*96*, *97*), and a list for
1186 phosphorylated residues measured in our phosphoproteomic data. The sequences in
1187 FASTA format were handled using Seqkit tool (*111*). With the NetPhorest algorithm, we
1188 obtained posterior probabilities that a residue was phosphorylated by protein kinase
1189 groups. We selected protein kinase groups with posterior probability value more than
1190 0.1 for each residue. Protein kinases contained in protein kinase groups were obtained
1191 from NetworKIN (*112*). We converted the NetworKIN kinase names to Ensembl IDs
1192 using Ensembl databases, STRING data in NetWorKIN_release3.0, and manual curation
1193 (Data File S10).

1194 We obtained a regulatory network among transcripts, proteins,
1195 phosphorylation, and activities of protein kinases and phosphorylation of substrate
1196 proteins. Using this network, we conducted kinase enrichment analyses for increased or
1197 decreased phosphorylation events during starvation in WT and *ob*/*ob* mice. The
1198 enrichment of increased or decreased phosphorylation events in each kinase group was
1199 determined using one-tailed Fisher's exact test followed by FDR correction conducted
1200 by the Benjamini-Hochberg procedure (*108*). Phosphorylation events quantified in more
1201 than half of the replicates in WT and *ob*/*ob* mice were used as background. Protein
1202 kinase groups with *Q*-values less than 0.1 were identified significantly enriched protein
1203 kinases.

1204 We screened the candidate protein kinases to define the upregulated or
1205 downregulated protein kinases using transcriptomic, proteomic, and phosphoproteomic

1206 data. If a protein kinase was enriched in increased phosphorylation events, and any of
1207 the transcriptomic, proteomic, or phosphoproteomic data of the protein kinase increased
1208 and none of the transcriptomic nor proteomic data decreased, the protein kinase was
1209 identified as an up-regulated protein kinase. If a protein kinase was enriched in
1210 decreased phosphorylation events, and any of the transcriptomic, proteomic, or
1211 phospho-proteomic data of the protein kinase decreased and none of the transcriptomic,
1212 proteomic, nor phosphoproteomic data increased, the protein kinase was identified as a
1213 downregulated protein kinase.
1214

1215 **Inference for activities of signaling pathways**

1216 Pathways in KEGG (*55–57*) database that contain "signaling" in their pathway names
1217 were defined as signaling pathways. We identified up-regulated or down-regulated
1218 signaling pathways that were enriched in increased or decreased transcripts, proteins, or
1219 phosphorylation events at least one omics layer of transcriptomic, proteomic, or
1220 phosphoproteomic data (Table 7; Data File S3).
1221

1222 **Construction of allosteric regulatory network**

1223 Allosteric regulation of metabolic reactions by metabolites was determined using
1224 BRENDA database (https://www.brenda-enzymes.org/download.php) (*113*). Activating
1225 and inhibiting compounds in mammals were extracted from brenda_2023_1.txt. Note
1226 that the taxonomy list of mammals was obtained from NCBI
1227 (https://ftp.ncbi.nlm.nih.gov/pub/taxonomy/new_taxdump/) (*114*). Compound names in
1228 brenda_2023_1.txt were transformed to KEGG ID via InChI key or using compound
1229 names in KEGG (ftp.kegg.net/kegg/ligand/compound.tar.gz) (*55–57*) or HMDB
1230 (https://hmdb.ca/downloads, ver. 5) (*115*). InChI keys of BRENDA ligands were

1231 obtained from the search results of "Search Ligands" function in the classic view of
1232 BRENDA without any query terms. Through these processes, we obtained the table of
1233 the pairs of EC numbers and KEGG compound IDs.
1234
1235 **Construction of transport network**
1236 We used the Transporter Classification Database (TCDB, https://tcdb.org/) (*58*) to
1237 identify transporters and substrates. Transport_activity was defined by the substrates of
1238 transports. To define substrates of transports, TC2ChEBI.txt in TCDB was processed as
1239 follows. TC2ChEBI.txt includes ChEBI IDs, that is a hierarchical database and linked to
1240 each other with "is_a" function (for example, anion (CHEBI: 22563) **is a** ion (CHEBI:
1241 24870)) (*116*). To focus on specific substrates, we selected ChEBI IDs that include less
1242 than 50 ChEBI IDs that can be traced by "is_a" function. The selected ChEBI IDs were
1243 transformed to KEGG compound IDs using KEGG
1244 (ftp.kegg.net/kegg/ligand/compound.tar.gz, downloaded on 13rd/12/2022) (*55–57*) or
1245 HMDB (https://hmdb.ca/downloads, ver. 5) (*115*), directly or via compound names.
1246 For transporter protein, we selected transporters that are expressed in human or
1247 mice using Uniprot database
1248 (https://ftp.uniprot.org/pub/databases/uniprot/knowledgebase/complete/) (*117*), using
1249 taxonomy list of mammals in NCBI
1250 (https://ftp.ncbi.nlm.nih.gov/pub/taxonomy/new_taxdump/) (*114*). Among them, we
1251 further screened the transporters localizing on cell membrane, by selecting transporters
1252 that include "Apical cell membrane", "Apicolateral cell membrane", "Basal cell
1253 membrane", "Basolateral cell membrane", "Cell membrane", or "Lateral cell
1254 membrane" in SUBCELLULARLOCATION in Uniprot database with at least one

1255 evidence in ECO:0000250, ECO:0000269, ECO:0000303, or ECO:0000305. Uniprot
1256 accessions were transformed to Entrez IDs by Uniprot database. Entrez IDs for human
1257 were translated to Entrez IDs for mice using gene ortholog table in NCBI database
1258 (gene_orthologs, https://ftp.ncbi.nlm.nih.gov/gene/DATA/) (*114*).
1259 Combining information of substrates and transporter proteins, we obtained a
1260 table of combinations of TCDB IDs, transporter Entrez IDs and KEGG compound IDs.
1261 Note that the transport_activities were defined by the name of substrates of the
1262 transport.
1263
1264 **Construction of the global starvation-responsive transomics network**
1265 To construct the global starvation-responsive transomics network, nodes were grouped
1266 into layers based on the chemical properties, biological functions, or both (Table 8).
1267 Layers were defined as follows:
1268 • The signaling_activity layer includes signaling pathways of KEGG database
1269 (*55–57*), that contains "signaling" in their pathway names.
1270 • The TF_activity, TF_mRNA, TF_protein, and TF_PTM layers include activities,
1271 transcripts, proteins, and phosphorylations of all the TFs investigated, those
1272 were included in "liver" or "hepatocytes" data in ChIP-Atlas database (*76*, *77*).
1273 • The kinase_activity layer contains all the activities of the protein kinase groups
1274 in the NetPhorest database (*110*).
1275 • The kinase_mRNA, kinase_protein, and kinase_PTM layers include transcripts,
1276 proteins, and phosphorylations of the protein kinases that belong to the kinase
1277 groups in the NetPhorest database, respectively.
1278 • Metabolic enzymes were defined using KEGG Pathway information

(ftp.kegg.net\kegg\pathway\organisms\mmu.tar.gz and ftp.kegg.net\kegg\pathway\pathway.list). The enzymes that belong to the pathways that are classified in "Metabolism" were defined as metabolic enzymes, except for Slc33a1 (mmu:11416), a transporter.

- The enzyme_mRNA, enzyme_protein, and enzyme_PTM layers include transcripts, proteins, and phosphorylations of metabolic enzymes, respectively.
- The metabolite (in the liver), lipid, FFA & acyls, and plasma metabolite layers include all the compounds measured in our metabolomic, lipidomic, and the FFA & acyls measurements.
- The transport_activity layer includes all the possible transport activities, that is defined using substrates of the transports in TCDB.
- The transporter_mRNA, transporter_protein, and transporter_PTM layers include all the measured transcripts, proteins, and phosphorylations of transporters regulating transport_activities, respectively.
- The metabolic reaction layer includes EC numbers in the KEGG database (*55–57*) (ftp.kegg.net\kegg\genes\organisms\mmu\mmu_link.tar.gz) that metabolic enzymes belong to.

Regulatory connections between nodes were determined using databases. The following databases or assumptions were used to infer the edges (regulatory connections):

- KEGG database (ftp.kegg.net\kegg\ligand\enzyme.tar.gz) (*55–57*) was used to infer the substrate and product regulation from metabolites, lipids, and FFA & acyls to metabolic reactions.
- The BRENDA (*113*) database was used to infer the allosteric regulatory connections from metabolites, lipids, and FFA & acyls to metabolic reactions.

1303 • Regulation from enzyme_protein and enzyme_PTM to metabolic reactions were
1304 defined using KEGG database (*55–57*).
1305 • Regulation of transport_activities was assumed to be mediated by the plasma
1306 metabolites, transporter_proteins, and transporter_PTMs.
1307 • TCDB was used to determine regulation of metabolites in the liver by
1308 transport_activity (*58*).
1309 • To determine regulatory connections between the TF_mRNA, TF_protein,
1310 TF_PTM and TF_activity layers, gene symbols of the bait in ChIP-Atlas
1311 database (TFs) were translated to ENSMUSG IDs using Ensembl database (ver.
1312 97) (*96*, *97*).
1313 • ChIP-Atlas (*76*, *77*) was used to determine regulatory connections between the
1314 TF_activity, and enzyme_mRNA or transporter_mRNA layers.
1315 • Regulation between the enzyme_mRNA and enzyme_protein, and
1316 transporter_mRNA and transporter_protein, were established by aligning Entrez
1317 IDs (*114*) of the metabolic enzymes and transporters.
1318 • For protein kinase and phosphorylations, the kinase_mRNA, kinase_protein, and
1319 kinase_PTM layers were assumed to regulate the kinase_activity layer.
1320 • NetPhorest (*110*) was used to determine regulation between the kinase_activity
1321 layer and the enzyme_PTM layer.
1322 • Signaling pathways were assumed to regulate TF_mRNA, TF_protein,
1323 TF_PTM, kinase_mRNA, kinase_protein, kinase_PTM, enzyme_mRNA,
1324 enzyme_protein, enzyme_PTM, transporter_mRNA, transporter_protein, and
1325 transporter_PTM. The regulatory relationships were defined using KEGG
1326 database. Note that signaling pathways and downstream molecules were

connected regardless of increase or decrease of the molecules.

For phosphorylation-related regulation, phosphorylation events curated as "activity, inhibited", "enzymatic activity, inhibited", "protein degradation", "receptor desensitization, induced", "receptor inactivation, induced", "receptor internalization, induced", or "receptor recycling, inhibited" in PhosphositePlus (https://www.phosphosite.org/staticDownloads) (*118*) were assumed to negatively regulates their downstream nodes.

Construction and structural analysis of the starvation-responsive metabolic network

The starvation-responsive metabolic network is a sub-network of the global starvation-responsive metabolic network containing metabolic reactions and their direct regulators, including metabolite, lipid, FFA & acyls, enzyme_protein and enzyme_PTM layers (Data File S6). It should be noted that if a metabolite regulates a metabolic reaction both as a substrate or product, and as an allosteric regulator, the edges were counted as a single edge in the starvation-responsive metabolic network. The network was regarded as directed graph for the calculation of degree and degree distribution. The degree of each node (k) was counted by the centrality function in MATLAB, with the 'outdegree' option specified, and degree distribution ($n(k)$) was determined. Scaling parameter was inferred by fitlm function in MATLAB. Hub nodes were defined as responsive nodes within the top 2% based on highest degrees.

The network was regarded as an undirected graph for the calculation of the following structural properties. Because the starvation-responsive metabolic network is composed of metabolic reactions and their direct regulators, all the edges are directed to

metabolic reactions and no edge starts from metabolic reactions. In this case, for the calculation of the cluster sizes, only weakly connected components are generated. For simplicity, we regarded the starvation-responsive metabolic network as an undirected graph. In addition, the average path length would be 1 if we regard the starvation-responsive metabolic network as a directed graph, because the regulators of the metabolic reactions (metabolites, lipids, FFA & acyls, proteins and phosphorylation events) regulate metabolic reactions with a single edge, and no edge starts from the metabolic reactions.

The conncomp function in MATLAB was used to determine the maximum cluster size. Distances between nodes were calculated by the distances function in MATLAB and the average path length of the graphs were determined. Note that distances among nodes without any connection were removed for calculation of the average path length.

To connect hub nodes to metabolic pathways (fig. S4), metabolic reactions were classified into metabolic pathways in carbohydrate metabolism, lipid metabolism, nucleotide metabolism, and amino acid metabolism using KEGG database (*55–57*). Then the number of metabolic reactions in each pathway that was regulated by the hub nodes was counted. The number of metabolic reactions were log2-transformed to display in the heatmap. Note that some metabolic reactions overlap among pathways because KEGG database (*55–57*) allow overlaps of metabolic reactions among pathways.

Calculation of *t*-half and temporal order analysis

The index of the temporal rate of response (*t*-half) was defined as the time when the

1375 responses to starvation reached the half of the maximum absolute values of the gain of
1376 the responses. We defined *t*-half for the responsive nodes not for metabolic reactions.
1377 Calculated *t*-half values were analyzed by the following procedures. The
1378 correlation between *t*-half and log10-transformed degree was determined by Spearman's
1379 correlation coefficient. Comparison between *t*-half values of WT-specific and *ob*/*ob*-
1380 specific hub molecules were conducted by Wilcoxon rank sum test. The classification of
1381 starvation-responsive metabolites, FFA & acyls, and lipids into metabolic pathways was
1382 conducted using KEGG database (*55–57*) for comparison of *t*-half values among
1383 metabolic pathways. Note that some molecules are included in multiple metabolic
1384 pathways. Comparisons of *t*-half values among metabolic pathways and omic layers
1385 were conducted using Kruskal-Wallis test followed by Dunn-Sidak test. Comparisons of
1386 *t*-half values between WT and *ob*/*ob* mice were conducted by Wilcoxon rank sum test
1387 followed by FDR correction conducted by the Benjamini-Hochberg procedure (*108*).
1388 To identify the essential molecules for negative correlation between log10-
1389 transformed degree and *t*-half in the starvation-responsive metabolic network in WT
1390 mice, leave-one-out correlation and cumulative leave-one-out correlation were
1391 calculated for each molecule. The leave-one-out correlation of molecule X was defined
1392 as correlation coefficient between the log10-transformed degree and *t*-half for all the
1393 responsive molecules in the starvation-responsive metabolic network except for X. The
1394 cumulative leave-one-out correlation of molecule X was defined as correlation
1395 coefficient between the log10-transformed degree and *t*-half of the responsive molecules
1396 in the starvation-responsive metabolic network with leave-one-out correlations that
1397 were smaller (the contribution to the negative correlation between log10-transformed
1398 degree and *t*-half is smaller) than X.

1399

1400 **Analysis of co-regulation among molecules in the starvation-responsive metabolic**
1401 **network and construction of correlation metabolic network**

1402 Pairwise Pearson's correlation coefficients were calculated among time courses of
1403 significantly changed or all the molecules [metabolites, lipids, FFA & acyls, protein
1404 (enzyme_protein), and phosphorylation events (enzyme_PTM)] in the starvation-
1405 responsive metabolic network in WT and *ob*/*ob* mice. The same procedure was
1406 conducted for significantly changed molecules in each metabolic pathway and the
1407 correlation coefficients between WT and *ob*/*ob* mice were compared by Wilcoxon rank
1408 sum test followed by FDR correction conducted by the Benjamini-Hochberg procedure
1409 (*108*).

1410 Based on these correlations, pairs of molecules whose Pearson's correlation
1411 coefficients are more than the threshold were connected by edges, resulting in
1412 correlation networks of the responsive molecules in the starvation-responsive metabolic
1413 network in WT and *ob*/*ob* mice, named as correlation metabolic networks. We tested
1414 several thresholds for the absolute value of the Pearson's correlation coefficients (from
1415 0.3 to 0.9). For each tested threshold, degree of each node was calculated using
1416 centrality function in MATLAB with the 'degree' option specified, and then degree
1417 distribution ($n(k)$) was determined. The scaling parameter was inferred by fitlm function
1418 in MATLAB for each threshold. In addition, the number of the clusters (fig. S12**B**), the
1419 relative size of the large cluster (fig. S12**C**) and the average path length (fig. S12**D**)
1420 were calculated using MATLAB (conncomp function for the number of the clusters and
1421 the relative size of the largest cluster and distances function for the average path length).

1422

1423 **Functional analysis of transcriptomic and proteomic data for potential clinical**
1424 **application**
1425 Hallmark gene sets (h.all.v7.4.entrez.gmt) were downloaded from the download page of
1426 MSigDB (*72*) (http://www.gsea-msigdb.org/gsea/login.jsp). Gene IDs were converted
1427 using gene ortholog table in NCBI database (gene_orthologs,
1428 https://ftp.ncbi.nlm.nih.gov/gene/DATA/) (*114*). We conducted functional enrichment
1429 analysis for significantly changed transcripts and proteins during starvation. The
1430 enrichment of significantly changed molecules in each hallmark was determined using
1431 one-tailed Fisher's exact test followed by FDR correction by the Benjamini-Hochberg
1432 procedure (*108*). Transcripts and proteins quantified in more than half of the replicates
1433 in WT and *ob*/*ob* mice were used as background. Hallmarks with Q-values < 0.1 were
1434 identified significantly enriched.
1435
1436 **Construction and analysis of each metabolic pathway**
1437 For fatty acid degradation (fig. S7), map of "Fatty acid degradation" (mmu00071) was
1438 extracted from KEGG database (*55–57*) and measured fatty acids, acyl-carnitines, and
1439 acyl-CoAs were basically annotated to palmitic acid (C00249), palmitoyl-CoA
1440 (C00154), and L-palmitoylcarnitine (C02990), respectively. Long-chain fatty acids and
1441 acyl-carnitines, whose number of carbons were more than 20, were annotated to long-
1442 chain fatty acid (C00638) and long-chain acyl-[acyl-carrier protein] (C20683). In
1443 addition, "Propanoate metabolism" (mmu00640) and "Butanoate metabolism"
1444 (mmu00650) were merged for acyl-CoA (3:0) and ketone body metabolism,
1445 respectively. Major metabolic reactions, substrates and products were manually
1446 extracted for further analyses.

1447 For glycolysis/gluconeogenesis (fig. S9) and urea cycle (fig. S10), major
1448 metabolic reactions, substrates and products were extracted from the map of
1449 "Glycolysis/gluconeogenesis" (mmu00010) and "Arginine biosynthesis" (mmu00220),
1450 respectively. Allosteric regulators (metabolites, FFA & acyls, and lipids),
1451 enzyme_protein, and enzyme_PTM of the extracted metabolic reactions were obtained
1452 from the global starvation-responsive transomic network (Fig. 3A; Data File S5) and
1453 visualized. For fatty acid degradation, significantly responsive enzyme_mRNA in WT
1454 or *ob*/*ob* mice corresponding to the responsive enzyme_protein in WT or *ob*/*ob* mice
1455 were also extracted and visualized. The starvation-responsive metabolic network of the
1456 extracted molecules was obtained from the starvation-responsive metabolic network
1457 (Data File S6). For glycolysis/gluconeogenesis (fig. S9) and urea cycle (fig. S10), the
1458 degree of each node (k) was counted by the centrality function in MATLAB, with the
1459 'outdegree' option specified. The degree distribution ($n(k)$) was also determined. Note
1460 that the networks were regarded as direct graphs for the calculation of degree and
1461 degree distribution. The fitlm function in MATLAB was used to calculate the scaling
1462 parameters. Correlations between t-half values and log10-transformed degree were
1463 determined by Spearman's correlation coefficient. Pairwise Pearson's correlation
1464 coefficients among time courses of the extracted molecules in each metabolic pathway
1465 were calculated to examine the co-regulations among the molecules in each metabolic
1466 pathway.
1467 For fatty acid degradation, t-half values of WT and *ob*/*ob* mice in each
1468 molecular type (FFA, acyl-carnitine, acyl-CoA, ketone body, metabolite,
1469 enzyme_protein, and enzyme_PTM) were compared by Wilcoxon rank sum test
1470 followed by FDR correction conducted by the Benjamini-Hochberg procedure (*108*).

1471 For fatty acid degradation, correlation between the time courses of enzyme_mRNA and
1472 enzyme_protein in each molecule in each genotype, that is included the extracted
1473 molecules visualized (fig. S7), were calculated using Pearson's correlation, followed by
1474 a comparison between WT and *ob*/*ob* mice by *t*-test.
1475
1476 **Implementation**
1477 Statistical test, enrichment analysis, construction of transomic network, and network
1478 analysis were conducted using MATLAB 2021a (The MathWorks Inc.). For edgeR, R
1479 language (version 4.1.1) was used. For handling of database, MATLAB, Python 3.8, R
1480 language, and Cygwin (version 3.2.0-1) were used. Transcriptomic analysis obtaining
1481 count and TPM data from sequences and running of NetPhorest software were
1482 conducted on the supercomputer system from the National Institute of Genetics in
1483 Japan. Transomic networks were visualized in Graph Modeling Language formats using
1484 Python 2.7 and Visualization and Analysis of Networks containing Experimental Data
1485 (VANTED) (*119*).
1486
1487 **Statistical Analysis**
1488 As described above, we conducted statistical analysis using MATLAB 2021a (The
1489 MathWorks Inc.) or R. For identification of responsive molecules, one-way ANOVA
1490 tests (ANOVA-like testing of edgeR (51–53) for transcriptome) were conducted in WT
1491 and *ob*/*ob* mice respectively. For pathway enrichment analysis, inference of activities of
1492 TFs, and inference of activities of protein kinases, one-tailed Fisher's exact test
1493 followed by FDR correction by the Benjamini-Hochberg procedure (96) was conducted.
1494 For comparison of *t*-half values of the hub molecules between WT and *ob*/*ob* mice,

Wilcoxon rank sum test was conducted. For multi comparison of *t*-half values, Kruskal-Wallis test followed by Dunn-Sidak test was conducted. For identification of responsive molecules or phosphorylation events, *P*-values less than 0.025 were defined as significant. For multiple comparisons except for identification of responsive molecules or phosphorylation events, *Q*-values less than 0.1 was defined as significant. *P*-values less than 0.05 were defined as significant in other cases.

Acknowledgments: We thank Maki Ohishi and Ayano Ueno (Keio University) for their expertise and assistance with metabolome analysis using CE-MS. We thank Maiko Goto (Kyushu University) for technical assistance with lipidome analysis using SFC-MS/MS and LC-MS. We also thank Kazusa DNA Research Institute for conducting the proteomic and phosphoproteomic measurements. We also thank our laboratory members for critically reading this manuscript and technical assistance with the experiments. The computational analysis of this work was performed in part with support of the supercomputer system of the National Institute of Genetics (NIG), Research Organization of Information and Systems (ROIS). The authors thank Nancy R. Gough (BioSerendipity, LLC) for editorial assistance and critical input. We used ChatGPT, DeepL, and Claude3 for the assistance of manuscript editing and coding.

Funding and Assistance: This study was supported by the Japan Society for the Promotion of Science (JSPS) KAKENHI grant numbers JP17H06299, JP17H06300, JP18H03979, JP21H04759, JP23H04939, and JP23H04946 to S.K.); CREST, the Japan Science and Technology Agency (JST) (JPMJCR2123 to S.K., Y. Inaba, and T.S.); The Uehara Memorial Foundation (to S.K.); K.M. receives funding from a Grant-in-Aid for

Early-Career Scientists (JP21K15342). A.Hatano receives funding from a Grant-in-Aid for Early-Career Scientists (JP22K15034). T.K. receives funding from a Grant-in-Aid for Early-Career Scientists (JP21K16349). T.T. receives funding from a Grant-in-Aid for Early-Career Scientists (JP20K19915). H.O. receives funding from a Grant-in-Aid for Early-Career Scientists (JP22K17992). S.O. receives funding from a Grant-in-Aid for Early-Career Scientists (JP21K14467). Y. Inaba also receives AMED-PRIME (JP23gm6910002). This work was also supported by the Japan Society for the Promotion of Science (JSPS) KAKENHI grant number JP22H04925 (PAGS); in part by the MEXT Cooperative Research Project Program, Medical Research Center Initiative for High Depth Omics, and CURE:JPMXP1323015486 for MIB, Kyushu University; and AMED Grant Number JP21zf0127001 (T.S.), JST, MEXT KAKENHI Grant Number JP23H04946(T.S.) and World Premier International Research Center Initiative (WPI), Human Biology-Microbiome-Quantum Research Center (Bio2Q) (T.S.), MEXT, Japan.; and JST FOREST Program (Grant Number JPMJFR2052, to A. Hirayama).

Author contributions: K.M., A. Hatano, T.K., H.S, S.O, and S.K. designed the project. K.M., A. Hatano, and M.M. conducted animal experiments and sample preparation for omic measurements. K.M. conducted single-omic analysis, transomic analysis, and network structural and temporal analyses. T.S. and A. Hirayama performed metabolomic analysis using CE-MS and IC-QEMS. Y. Izumi., M.T., and T.B. performed lipidomic analysis using LC-MS and SFC-MS/MS. Y.S. performed transcriptomic analysis using RNA-seq. K.M., T.T., R.E., and H.O. analyzed the RNA-seq data. K.M., T.K., H.S., D.L., and A.T. conducted database for transomic analysis. The writing group

consisted of K.M., Y. Inaba, H.I., and S.K. The study was conceived and supervised by K.M. and S.K.

Conflict of Interest: The authors declare that they have no competing interests.

Data and code availability: Sequencing data have been deposited in the DNA Data Bank of Japan Sequence Read Archive (DRA) (www.ddbj.nig.ac.jp/) with accession no. DRR571760-DRR571839. Proteome and phosphoproteome data were deposited in jPOSTrepo (*120*) (https://repository.jpostdb.org/) with accession no. JPST003082 (proteome, for reviewers: https://repository.jpostdb.org/preview/56792610366738a30bc36f, Access key is 9357) and JPST003130 (phosphoproteome, for reviewers: https://repository.jpostdb.org/preview/124893828466738a2ae0323, Access key is 4346). All other data are present in the paper or the Supplementary Materials. The code used for the analysis in this paper was deposited in Zenodo (DOI: 10.5281/zenodo.14061381).

Prior Presentation: A non–peer-reviewed version of this article was submitted to the bioRxiv preprint server (https://www.biorxiv.org/content/10.1101/2024.06.17.599249v1).

Supplementary Materials

Figs. S1 to S12

Data Files S1 to S10

References and Notes

1. G. F. Cahill Jr, Fuel metabolism in starvation. *Annu. Rev. Nutr.* **26**, 1–22 (2006).

2. T. Wang, C. C. Y. Hung, D. J. Randall, The comparative physiology of food deprivation: from feast to famine. *Annu. Rev. Physiol.* **68**, 223–251 (2006).

3. C. E. Geisler, C. Hepler, M. R. Higgins, B. J. Renquist, Hepatic adaptations to maintain metabolic homeostasis in response to fasting and refeeding in mice. *Nutr. Metab.* **13**, 62 (2016).

4. S. D. Anton, K. Moehl, W. T. Donahoo, K. Marosi, S. A. Lee, A. G. Mainous 3rd, C. Leeuwenburgh, M. P. Mattson, Flipping the Metabolic Switch: Understanding and Applying the Health Benefits of Fasting. *Obesity* **26**, 254–268 (2018).

5. I. Goldstein, G. L. Hager, Transcriptional and Chromatin Regulation during Fasting - The Genomic Era. *Trends Endocrinol. Metab.* **26**, 699–710 (2015).

6. S. J. Hofer, D. Carmona-Gutierrez, M. I. Mueller, F. Madeo, The ups and downs of caloric restriction and fasting: from molecular effects to clinical application. *EMBO Mol. Med.* **14**, e14418 (2022).

7. A. Ghazalpour, B. J. Bennett, D. Shih, N. Che, L. Orozco, C. Pan, R. Hagopian, A. He, P. Kayne, W.-P. Yang, T. Kirchgessner, A. J. Lusis, Genetic regulation of mouse liver metabolite levels. *Mol. Syst. Biol.* **10**, 730 (2014).

8. O. E. Owen, P. Felig, A. P. Morgan, J. Wahren, G. F. Cahill Jr, Liver and kidney metabolism during prolonged starvation. *J. Clin. Invest.* **48**, 574–583 (1969).

9. F. Pietrocola, Y. Demont, F. Castoldi, D. Enot, S. Durand, M. Semeraro, E. E. Baracco, J. Pol, J. M. Bravo-San Pedro, C. Bordenave, S. Levesque, J. Humeau, A. Chery, D. Métivier, F. Madeo, M. C. Maiuri, G. Kroemer, Metabolic effects of fasting on human and mouse blood in vivo. *Autophagy* **13**, 567–578 (2017).

10. M. Defour, G. J. E. J. Hooiveld, M. van Weeghel, S. Kersten, Probing metabolic memory in the hepatic response to fasting. *Physiol. Genomics* **52**, 602–617 (2020).

11. R. Thøgersen, C. M. Kristensen, M. A. Olsen, H. C. Bertram, H. Pilegaard, M. K. Rasmussen, Hepatic PGC-1α is not essential for fasting-induced cytochrome p450 regulation in mouse liver. *Biochem. Pharmacol.* **172**, 113736 (2020).

12. C. Rennert, S. Vlaic, E. Marbach-Breitrück, C. Thiel, S. Sales, A. Shevchenko, R. Gebhardt, M. Matz-Soja, The Diurnal Timing of Starvation Differently Impacts Murine Hepatic Gene Expression and Lipid Metabolism - A Systems Biology Analysis Using Self-Organizing Maps. *Front. Physiol.* **9**, 1180 (2018).

13. M. Régnier, A. Polizzi, Y. Lippi, E. Fouché, G. Michel, C. Lukowicz, S. Smati, A. Marrot, F. Lasserre, C. Naylies, A. Batut, F. Viars, J. Bertrand-Michel, C. Postic, N. Loiseau, W. Wahli, H. Guillou, A. Montagner, Insights into the role of hepatocyte PPARα activity in response to fasting. *Mol. Cell. Endocrinol.* **471**, 75–88 (2018).

14. M. Schupp, F. Chen, E. R. Briggs, S. Rao, H. J. Pelzmann, A. R. Pessentheiner, J. G. Bogner-Strauss, M. A. Lazar, D. Baldwin, A. Prokesch, Metabolite and transcriptome analysis during fasting suggest a role for the p53-Ddit4 axis in major metabolic tissues. *BMC Genomics* **14**, 758 (2013).

15. K. Lenaerts, M. Sokolović, F. G. Bouwman, W. H. Lamers, E. C. Mariman, J. Renes, Starvation induces phase-specific changes in the proteome of mouse small intestine. *J. Proteome Res.* **5**, 2113–2122 (2006).

16. M. L. Steinhauser, B. A. Olenchock, J. O'Keefe, M. Lun, K. A. Pierce, H. Lee, L. Pantano, A. Klibanski, G. I. Shulman, C. B. Clish, P. K. Fazeli, The circulating metabolome of human starvation. *JCI Insight* **3** (2018).

17. I. Rubio-Aliaga, B. de Roos, S. J. Duthie, L. K. Crosley, C. Mayer, G. Horgan, I. J. Colquhoun, G. Le Gall, F. Huber, W. Kremer, M. Rychlik, S. Wopereis, B. van Ommen, G. Schmidt, C. Heim, F. G. Bouwman, E. C. Mariman, F. Mulholland, I. T. Johnson, A. C. Polley, R. M. Elliott, H. Daniel, Metabolomics of prolonged fasting in humans reveals new catabolic markers. *Metabolomics* **7**, 375–387 (2011).

18. M. Pietzner, B. Uluvar, K. J. Kolnes, P. B. Jeppesen, S. V. Frivold, Ø. Skattebo, E. I. Johansen, B. S. Skålhegg, J. F. P. Wojtaszewski, A. J. Kolnes, G. S. H. Yeo, S. O'Rahilly, J. Jensen, C. Langenberg, Systemic proteome adaptions to 7-day complete caloric restriction in humans. *Nature Metabolism*, 1–14 (2024).

19. T. Wasselin, S. Zahn, Y. L. Maho, A. Van Dorsselaer, T. Raclot, F. Bertile, Exacerbated oxidative stress in the fasting liver according to fuel partitioning. *Proteomics* **14**, 1905–1921 (2014).

20. M. J. Brauer, J. Yuan, B. D. Bennett, W. Lu, E. Kimball, D. Botstein, J. D. Rabinowitz, Conservation of the metabolomic response to starvation across two divergent microbes. *Proc. Natl. Acad. Sci. U. S. A.* **103**, 19302–19307 (2006).

21. B. Bergdahl, D. Heer, U. Sauer, B. Hahn-Hägerdal, E. W. van Niel, Dynamic metabolomics differentiates between carbon and energy starvation in recombinant Saccharomyces cerevisiae fermenting xylose. *Biotechnol. Biofuels* **5**, 34 (2012).

22. H. Link, T. Fuhrer, L. Gerosa, N. Zamboni, U. Sauer, Real-time metabolome profiling of the metabolic switch between starvation and growth. *Nat. Methods* **12**, 1091–1097 (2015).

23. D. Peng, C. Ruan, S. Fu, C. He, J. Song, H. Li, Y. Tu, D. Tang, L. Yao, S. Lin, Y. Shi, W. Zhang, H. Zhou, L. Zhu, C. Ma, C. Chang, J. Ma, Z. Xie, C. Wang, Y. Xue, Atg9-centered multi-omics integration reveals new autophagy regulators in Saccharomyces cerevisiae. *Autophagy* **17**, 4453–4476 (2021).

24. E. B. Harvald, R. R. Sprenger, K. B. Dall, C. S. Ejsing, R. Nielsen, S. Mandrup, A. B. Murillo, M. Larance, A. Gartner, A. I. Lamond, N. J. Færgeman, Multi-omics Analyses of Starvation Responses Reveal a Central Role for Lipoprotein Metabolism in Acute Starvation Survival in C. elegans. *Cell Syst* **5**, 38-52.e4 (2017).

25. M. N. Goodman, P. R. Larsen, M. M. Kaplan, T. T. Aoki, V. R. Young, N. B. Ruderman, Starvation in the rat. II. Effect of age and obesity on protein sparing and fuel metabolism. *Am. J. Physiol.* **239**, E277–E286 (1980).

26. A. R. Soltis, N. J. Kennedy, X. Xin, F. Zhou, S. B. Ficarro, Y. S. Yap, B. J. Matthews, D. A. Lauffenburger, F. M. White, J. A. Marto, R. J. Davis, E. Fraenkel, Hepatic Dysfunction Caused by Consumption of a High-Fat Diet. *Cell Rep.* **21**, 3317–3328 (2017).

27. J. Stöckli, K. H. Fisher-Wellman, R. Chaudhuri, X.-Y. Zeng, D. J. Fazakerley, C. C. Meoli, K. C. Thomas, N. J. Hoffman, S. P. Mangiafico, C. E. Xirouchaki, C.-H. Yang, O. Ilkayeva, K. Wong, G. J. Cooney, S. Andrikopoulos, D. M. Muoio, D. E. James, Metabolomic analysis of insulin resistance across different mouse strains and diets. *J. Biol. Chem.* **292**, 19135–19145 (2017).

28. M. E. Nelson, S. Madsen, K. C. Cooke, A. M. Fritzen, I. H. Thorius, S. W. C. Masson, L. Carroll, F. C. Weiss, M. M. Seldin, M. Potter, S. L. Hocking, D. J. Fazakerley, A. E. Brandon, S. Thillainadesan, A. M. Senior, G. J. Cooney, J. Stöckli, D. E. James, Systems-level analysis of insulin action in mouse strains provides insight into tissue- and pathway-specific interactions that drive insulin resistance. *Cell Metab.* **0** (2022).

29. D. J. Fazakerley, J. van Gerwen, K. C. Cooke, X. Duan, E. J. Needham, A. Díaz-Vegas, S. Madsen, D. M. Norris, A. S. Shun-Shion, J. R. Krycer, J. G. Burchfield, P. Yang, M. R. Wade, J. T. Brozinick, D. E. James, S. J. Humphrey, Phosphoproteomics reveals rewiring of the insulin signaling network and multi-nodal defects in insulin resistance. *Nat. Commun.* **14**, 1–20 (2023).

30. J. H. Stern, G. I. Smith, S. Chen, R. H. Unger, S. Klein, P. E. Scherer, Obesity dysregulates fasting-induced changes in glucagon secretion. *J. Endocrinol.* **243**, 149–160 (2019).

31. A. Di Francesco, A. G. Deighan, L. Litichevskiy, Z. Chen, A. Luciano, L. Robinson, G. Garland, H. Donato, M. Vincent, W. Schott, K. M. Wright, A. Raj, G. V. Prateek, M. Mullis, W. G. Hill, M. L. Zeidel, L. L. Peters, F. Harding, D. Botstein, R. Korstanje, C. A. Thaiss, A. Freund, G. A. Churchill, Dietary restriction impacts health and lifespan of genetically diverse mice. *Nature*, 1–9 (2024).

32. A.-L. Barabási, Z. N. Oltvai, Network biology: understanding the cell's functional organization. *Nat. Rev. Genet.* **5**, 101–113 (2004).

33. A. Halu, R. J. Mondragón, P. Panzarasa, G. Bianconi, Multiplex PageRank. *PLoS One* **8**, e78293 (2013).

34. K. Chella Krishnan, Z. Kurt, R. Barrere-Cain, S. Sabir, A. Das, R. Floyd, L. Vergnes, Y. Zhao, N. Che, S. Charugundla, H. Qi, Z. Zhou, Y. Meng, C. Pan, M. M. Seldin, F. Norheim, S. Hui, K. Reue, A. J. Lusis, X. Yang, Integration of Multi-omics Data from Mouse Diversity Panel Highlights Mitochondrial Dysfunction in Non-alcoholic Fatty Liver Disease. *Cell Syst* **6**, 103-115.e7 (2018).

35. A. Halu, M. De Domenico, A. Arenas, A. Sharma, The multiplex network of human diseases. *NPJ Syst Biol Appl* **5**, 15 (2019).

36. K. Yugi, H. Kubota, Y. Toyoshima, R. Noguchi, K. Kawata, Y. Komori, S. Uda, K. Kunida, Y. Tomizawa, Y. Funato, H. Miki, M. Matsumoto, K. I. Nakayama, K. Kashikura, K. Endo, K. Ikeda, T. Soga, S. Kuroda, Reconstruction of insulin signal flow from phosphoproteome and metabolome data. *Cell Rep.* **8**, 1171–1183 (2014).

37. T. Kokaji, A. Hatano, Y. Ito, K. Yugi, M. Eto, K. Morita, S. Ohno, M. Fujii, K.-I. Hironaka, R. Egami, A. Terakawa, T. Tsuchiya, H. Ozaki, H. Inoue, S. Uda, H. Kubota, Y. Suzuki, K. Ikeda, M. Arita, M. Matsumoto, K. I. Nakayama, A. Hirayama, T. Soga, S. Kuroda, Transomics analysis reveals allosteric and gene regulation axes for altered hepatic glucose-responsive metabolism in obesity. *Sci. Signal.* **13** (2020).

38. T. Kokaji, M. Eto, A. Hatano, K. Yugi, K. Morita, S. Ohno, M. Fujii, K.-I. Hironaka, Y. Ito, R. Egami, S. Uematsu, A. Terakawa, Y. Pan, H. Maehara, D. Li, Y. Bai, T. Tsuchiya, H. Ozaki, H. Inoue, H. Kubota, Y. Suzuki, A. Hirayama, T. Soga, S. Kuroda, In vivo transomic analyses of glucose-responsive metabolism in skeletal muscle reveal core differences between the healthy and obese states. *Sci. Rep.* **12**, 13719 (2022).

39. H. Sugimoto, K. Morita, D. Li, Y. Bai, M. Mattanovich, S. Kuroda, iTraNet: a web-based platform for integrated trans-omics network visualization and analysis. *Bioinform. Adv.* **4**, vbae141 (2024).

40. E. Ravasz, A. L. Somera, D. A. Mongru, Z. N. Oltvai, A. L. Barabási, Hierarchical organization of modularity in metabolic networks. *Science* **297**, 1551–1555 (2002).

41. Y. Asgari, A. Salehzadeh-Yazdi, F. Schreiber, A. Masoudi-Nejad, Controllability in cancer metabolic networks according to drug targets as driver nodes. *PLoS One* **8**, e79397 (2013).

42. J.-M. Schwartz, H. Otokuni, T. Akutsu, J. C. Nacher, Probabilistic controllability approach to metabolic fluxes in normal and cancer tissues. *Nat. Commun.* **10**, 2725 (2019).

43. A. L. Barabasi, R. Albert, Emergence of scaling in random networks. *Science* **286**, 509–512 (1999).

44. P. Lindström, The physiology of obese-hyperglycemic mice [ob/ob mice]. *ScientificWorldJournal* **7**, 666–685 (2007).

45. R. Egami, T. Kokaji, A. Hatano, K. Yugi, M. Eto, K. Morita, S. Ohno, M. Fujii, K.-I. Hironaka, S. Uematsu, A. Terakawa, Y. Bai, Y. Pan, T. Tsuchiya, H. Ozaki, H. Inoue, S. Uda, H. Kubota, Y. Suzuki, M. Matsumoto, K. I. Nakayama, A. Hirayama, T. Soga, S. Kuroda, Trans-omic analysis reveals obesity-associated dysregulation of inter-organ metabolic cycles between the liver and skeletal muscle. *iScience* **24**, 102217 (2021).

46. Y. Bai, K. Morita, T. Kokaji, A. Hatano, S. Ohno, R. Egami, Y. Pan, D. Li, K. Yugi, S. Uematsu, H. Inoue, Y. Inaba, Y. Suzuki, M. Matsumoto, M. Takahashi, Y. Izumi, T. Bamba, A. Hirayama, T. Soga, S. Kuroda, Trans-omic analysis reveals opposite metabolic dysregulation between feeding and fasting in liver associated with obesity. *iScience* **27**, 109121 (2024).

47. S.-M. Fendt, J. M. Buescher, F. Rudroff, P. Picotti, N. Zamboni, U. Sauer, Tradeoff between enzyme and metabolite efficiency maintains metabolic homeostasis upon perturbations in enzyme capacity. *Mol. Syst. Biol.* **6**, 356 (2010).

48. D. Lorendeau, S. Christen, G. Rinaldi, S.-M. Fendt, Metabolic control of signalling pathways and metabolic auto-regulation. *Biol. Cell* **107**, 251–272 (2015).

49. M. D. Robinson, D. J. McCarthy, G. K. Smyth, edgeR: a Bioconductor package for differential expression analysis of digital gene expression data. *Bioinformatics* **26**, 139–140 (2010).

50. D. J. McCarthy, Y. Chen, G. K. Smyth, Differential expression analysis of multifactor RNA-Seq experiments with respect to biological variation. *Nucleic Acids Res.* **40**, 4288–4297 (2012).

51. Y. Chen, A. T. L. Lun, G. K. Smyth, From reads to genes to pathways: differential expression analysis of RNA-Seq experiments using Rsubread and the edgeR quasi-likelihood pipeline. *F1000Res.* **5**, 1438 (2016).

52. G. L. King, N. Das-Evcimen, Role of protein kinase C in diabetic complications. *Expert Rev. Endocrinol. Metab.* **5**, 77–88 (2010).

53. A. C. Newton, Protein kinase C: perfectly balanced. *Crit. Rev. Biochem. Mol. Biol.* **53**, 208–230 (2018).

54. O. Bezy, T. T. Tran, J. Pihlajamäki, R. Suzuki, B. Emanuelli, J. Winnay, M. A. Mori, J. Haas, S. B. Biddinger, M. Leitges, A. B. Goldfine, M. E. Patti, G. L. King,

C. R. Kahn, PKCδ regulates hepatic insulin sensitivity and hepatosteatosis in mice and humans. *J. Clin. Invest.* **121**, 2504–2517 (2011).

55. M. Kanehisa, S. Goto, Y. Sato, M. Furumichi, M. Tanabe, KEGG for integration and interpretation of large-scale molecular data sets. *Nucleic Acids Res.* **40**, D109-14 (2012).

56. M. Kanehisa, M. Furumichi, M. Tanabe, Y. Sato, K. Morishima, KEGG: new perspectives on genomes, pathways, diseases and drugs. *Nucleic Acids Res.* **45**, D353–D361 (2017).

57. M. Kanehisa, M. Furumichi, Y. Sato, M. Kawashima, M. Ishiguro-Watanabe, KEGG for taxonomy-based analysis of pathways and genomes. *Nucleic Acids Res.* **51**, D587–D592 (2023).

58. M. H. Saier, V. S. Reddy, G. Moreno-Hagelsieb, K. J. Hendargo, Y. Zhang, V. Iddamsetty, K. J. K. Lam, N. Tian, S. Russum, J. Wang, A. Medrano-Soto, The Transporter Classification Database (TCDB): 2021 update. *Nucleic Acids Res.* **49**, D461–D467 (2021).

59. L. Yang, P. Li, S. Fu, E. S. Calay, G. S. Hotamisligil, Defective hepatic autophagy in obesity promotes ER stress and causes insulin resistance. *Cell Metab.* **11**, 467–478 (2010).

60. S. Fu, J. Fan, J. Blanco, A. Gimenez-Cassina, N. N. Danial, S. M. Watkins, G. S. Hotamisligil, Polysome profiling in liver identifies dynamic regulation of endoplasmic reticulum translatome by obesity and fasting. *PLoS Genet.* **8**, e1002902 (2012).

61. A. A. Atiia, C. Hopper, K. Inoue, S. Vidal, J. Waldispühl, Computational intractability law molds the topology of biological networks. *Applied Network Science* **5**, 1–22 (2020).

62. Y.-Y. Liu, J.-J. Slotine, A.-L. Barabási, Controllability of complex networks. *Nature* **473**, 167–173 (2011).

63. A. D. Broido, A. Clauset, Scale-free networks are rare. *Nat. Commun.* **10**, 1017 (2019).

64. R. Albert, H. Jeong, A. L. Barabasi, Error and attack tolerance of complex networks. *Nature* **406**, 378–382 (2000).

65. S. Herzig, R. J. Shaw, AMPK: guardian of metabolism and mitochondrial homeostasis. *Nat. Rev. Mol. Cell Biol.* **19**, 121–135 (2018).

66. S. Kovacic, C.-L. M. Soltys, A. J. Barr, I. Shiojima, K. Walsh, J. R. B. Dyck, Akt activity negatively regulates phosphorylation of AMP-activated protein kinase in the heart. *J. Biol. Chem.* **278**, 39422–39427 (2003).

67. N. Donnelly, A. M. Gorman, S. Gupta, A. Samali, The eIF2α kinases: their structures and functions. *Cell. Mol. Life Sci.* **70**, 3493–3511 (2013).

68. N. Mizushima, L. O. Murphy, Autophagy assays for biological discovery and therapeutic development. *Trends Biochem. Sci.* **45**, 1080–1093 (2020).

69. Y. Ichimura, S. Waguri, Y.-S. Sou, S. Kageyama, J. Hasegawa, R. Ishimura, T. Saito, Y. Yang, T. Kouno, T. Fukutomi, T. Hoshii, A. Hirao, K. Takagi, T. Mizushima, H. Motohashi, M.-S. Lee, T. Yoshimori, K. Tanaka, M. Yamamoto, M. Komatsu, Phosphorylation of p62 activates the Keap1-Nrf2 pathway during selective autophagy. *Mol. Cell* **51**, 618–631 (2013).

70. A. A. Parkhitko, E. Filine, S. E. Mohr, A. Moskalev, N. Perrimon, Targeting metabolic pathways for extension of lifespan and healthspan across multiple species. *Ageing Res. Rev.* **64**, 101188 (2020).

71. M. M. Mihaylova, A. Chaix, M. Delibegovic, J. J. Ramsey, J. Bass, G. Melkani, R. Singh, Z. Chen, W. W. Ja, M. Shirasu-Hiza, M. N. Latimer, J. A. Mattison, A. E. Thalacker-Mercer, V. D. Dixit, S. Panda, D. W. Lamming, When a calorie is not just a calorie: Diet quality and timing as mediators of metabolism and healthy aging. *Cell Metab.*, doi: 10.1016/j.cmet.2023.06.008 (2023).

72. A. Liberzon, C. Birger, H. Thorvaldsdóttir, M. Ghandi, J. P. Mesirov, P. Tamayo, The Molecular Signatures Database (MSigDB) hallmark gene set collection. *Cell Syst* **1**, 417–425 (2015).

73. J. Saez-Rodriguez, L. G. Alexopoulos, M. Zhang, M. K. Morris, D. A. Lauffenburger, P. K. Sorger, Comparing signaling networks between normal and transformed hepatocytes using discrete logical models. *Cancer Res.* **71**, 5400–5411 (2011).

74. H. Morishita, N. Mizushima, Diverse cellular roles of autophagy. *Annu. Rev. Cell Dev. Biol.* **35**, 453–475 (2019).

75. R. A. Haeusler, K. Hartil, B. Vaitheesvaran, I. Arrieta-Cruz, C. M. Knight, J. R. Cook, H. L. Kammoun, M. A. Febbraio, R. Gutierrez-Juarez, I. J. Kurland, D. Accili, Integrated control of hepatic lipogenesis versus glucose production requires FoxO transcription factors. *Nat. Commun.* **5**, 5190 (2014).

76. S. Oki, T. Ohta, G. Shioi, H. Hatanaka, O. Ogasawara, Y. Okuda, H. Kawaji, R. Nakaki, J. Sese, C. Meno, ChIP-Atlas: a data-mining suite powered by full integration of public ChIP-seq data. *EMBO Rep.* **19** (2018).

77. Z. Zou, T. Ohta, F. Miura, S. Oki, ChIP-Atlas 2021 update: a data-mining suite for exploring epigenomic landscapes by fully integrating ChIP-seq, ATAC-seq and Bisulfite-seq data. *Nucleic Acids Res.* **50**, W175–W182 (2022).

78. G. J. Gowans, D. G. Hardie, AMPK: a cellular energy sensor primarily regulated by AMP. *Biochem. Soc. Trans.* **42**, 71–75 (2014).

79. G. Y. Liu, D. M. Sabatini, mTOR at the nexus of nutrition, growth, ageing and disease. *Nat. Rev. Mol. Cell Biol.* **21**, 183–203 (2020).

80. E. J. Needham, B. L. Parker, T. Burykin, D. E. James, S. J. Humphrey, Illuminating the dark phosphoproteome. *Sci. Signal.* **12** (2019).

81. I. Piazza, K. Kochanowski, V. Cappelletti, T. Fuhrer, E. Noor, U. Sauer, P. Picotti, A Map of Protein-Metabolite Interactions Reveals Principles of Chemical Communication. *Cell* **172**, 358-372.e23 (2018).

82. M. Luzarowski, R. Vicente, A. Kiselev, M. Wagner, D. Schlossarek, A. Erban, L. P. de Souza, D. Childs, I. Wojciechowska, U. Luzarowska, M. Górka, E. M. Sokołowska, M. Kosmacz, J. C. Moreno, A. Brzezińska, B. Vegesna, J. Kopka, A. R. Fernie, L. Willmitzer, J. C. Ewald, A. Skirycz, Global mapping of protein-metabolite interactions in Saccharomyces cerevisiae reveals that Ser-Leu dipeptide regulates phosphoglycerate kinase activity. *Commun. Biol.* **4**, 181 (2021).

83. K. G. Hicks, A. A. Cluntun, H. L. Schubert, S. R. Hackett, J. A. Berg, P. G. Leonard, M. A. Ajalla Aleixo, Y. Zhou, A. J. Bott, S. R. Salvatore, F. Chang, A. Blevins, P. Barta, S. Tilley, A. Leifer, A. Guzman, A. Arok, S. Fogarty, J. M. Winter, H.-C. Ahn, K. N. Allen, S. Block, I. A. Cardoso, J. Ding, I. Dreveny, W. C. Gasper,

Q. Ho, A. Matsuura, M. J. Palladino, S. Prajapati, P. Sun, K. Tittmann, D. R. Tolan, J. Unterlass, A. P. VanDemark, M. G. Vander Heiden, B. A. Webb, C.-H. Yun, P. Zhao, B. Wang, F. J. Schopfer, C. P. Hill, M. C. Nonato, F. L. Muller, J. E. Cox, J. Rutter, Protein-metabolite interactomics of carbohydrate metabolism reveal regulation of lactate dehydrogenase. *Science* **379**, 996–1003 (2023).

84. V. Cappelletti, T. Hauser, I. Piazza, M. Pepelnjak, L. Malinovska, T. Fuhrer, Y. Li, C. Dörig, P. Boersema, L. Gillet, J. Grossbach, A. Dugourd, J. Saez-Rodriguez, A. Beyer, N. Zamboni, A. Caflisch, N. de Souza, P. Picotti, Dynamic 3D proteomes reveal protein functional alterations at high resolution in situ. *Cell* **184**, 545-559.e22 (2021).

85. S. Müller-Dott, E. Tsirvouli, M. Vazquez, R. O. Ramirez Flores, P. Badia-I-Mompel, R. Fallegger, D. Türei, A. Lægreid, J. Saez-Rodriguez, Expanding the coverage of regulons from high-confidence prior knowledge for accurate estimation of transcription factor activities. *Nucleic Acids Res.* **51**, 10934–10949 (2023).

86. J. L. Johnson, T. M. Yaron, E. M. Huntsman, A. Kerelsky, J. Song, A. Regev, T.-Y. Lin, K. Liberatore, D. M. Cizin, B. M. Cohen, N. Vasan, Y. Ma, K. Krismer, J. T. Robles, B. van de Kooij, A. E. van Vlimmeren, N. Andrée-Busch, N. F. Käufer, M. V. Dorovkov, A. G. Ryazanov, Y. Takagi, E. R. Kastenhuber, M. D. Goncalves, B. D. Hopkins, O. Elemento, D. J. Taatjes, A. Maucuer, A. Yamashita, A. Degterev, M. Uduman, J. Lu, S. D. Landry, B. Zhang, I. Cossentino, R. Linding, J. Blenis, P. V. Hornbeck, B. E. Turk, M. B. Yaffe, L. C. Cantley, An atlas of substrate specificities for the human serine/threonine kinome. *Nature*, doi: 10.1038/s41586-022-05575-3 (2023).

87. D. Türei, T. Korcsmáros, J. Saez-Rodriguez, OmniPath: guidelines and gateway for literature-curated signaling pathway resources. *Nat. Methods* **13**, 966–967 (2016).

88. R. C. Davis, A. van Nas, L. W. Castellani, Y. Zhao, Z. Zhou, P. Wen, S. Yu, H. Qi, M. Rosales, E. E. Schadt, K. W. Broman, M. Péterfy, A. J. Lusis, Systems genetics of susceptibility to obesity-induced diabetes in mice. *Physiol. Genomics* **44**, 1–13 (2012).

89. T. Soga, D. N. Heiger, Amino acid analysis by capillary electrophoresis electrospray ionization mass spectrometry. *Anal. Chem.* **72**, 1236–1241 (2000).

90. T. Soga, R. Baran, M. Suematsu, Y. Ueno, S. Ikeda, T. Sakurakawa, Y. Kakazu, T. Ishikawa, M. Robert, T. Nishioka, M. Tomita, Differential metabolomics reveals ophthalmic acid as an oxidative stress biomarker indicating hepatic glutathione consumption. *J. Biol. Chem.* **281**, 16768–16776 (2006).

91. T. Soga, K. Igarashi, C. Ito, K. Mizobuchi, H.-P. Zimmermann, M. Tomita, Metabolomic profiling of anionic metabolites by capillary electrophoresis mass spectrometry. *Anal. Chem.* **81**, 6165–6174 (2009).

92. A. Hirayama, S. Tabata, R. Kudo, M. Hasebe, K. Suzuki, M. Tomita, T. Soga, The use of a double coaxial electrospray ionization sprayer improves the peak resolutions of anionic metabolites in capillary ion chromatography-mass spectrometry. *J. Chromatogr. A* **1619**, 460914 (2020).

93. E. G. Bligh, W. J. Dyer, A rapid method of total lipid extraction and purification. *Can. J. Biochem. Physiol.* **37**, 911–917 (1959).

94. T. Fushimi, Y. Izumi, M. Takahashi, K. Hata, Y. Murano, T. Bamba, Dynamic Metabolome Analysis Reveals the Metabolic Fate of Medium-Chain Fatty Acids in AML12 Cells. *J. Agric. Food Chem.* **68**, 11997–12010 (2020).

95. H. Takeda, Y. Izumi, M. Takahashi, T. Paxton, S. Tamura, T. Koike, Y. Yu, N. Kato, K. Nagase, M. Shiomi, T. Bamba, Widely-targeted quantitative lipidomics method by supercritical fluid chromatography triple quadrupole mass spectrometry. *J. Lipid Res.* **59**, 1283–1293 (2018).

96. P. Flicek, M. R. Amode, D. Barrell, K. Beal, K. Billis, S. Brent, D. Carvalho-Silva, P. Clapham, G. Coates, S. Fitzgerald, L. Gil, C. G. Girón, L. Gordon, T. Hourlier, S. Hunt, N. Johnson, T. Juettemann, A. K. Kähäri, S. Keenan, E. Kulesha, F. J. Martin, T. Maurel, W. M. McLaren, D. N. Murphy, R. Nag, B. Overduin, M. Pignatelli, B. Pritchard, E. Pritchard, H. S. Riat, M. Ruffier, D. Sheppard, K. Taylor, A. Thormann, S. J. Trevanion, A. Vullo, S. P. Wilder, M. Wilson, A. Zadissa, B. L. Aken, E. Birney, F. Cunningham, J. Harrow, J. Herrero, T. J. P. Hubbard, R. Kinsella, M. Muffato, A. Parker, G. Spudich, A. Yates, D. R. Zerbino, S. M. J. Searle, Ensembl 2014. *Nucleic Acids Res.* **42**, D749-55 (2014).

97. F. Cunningham, M. R. Amode, D. Barrell, K. Beal, K. Billis, S. Brent, D. Carvalho-Silva, P. Clapham, G. Coates, S. Fitzgerald, L. Gil, C. G. Girón, L. Gordon, T. Hourlier, S. E. Hunt, S. H. Janacek, N. Johnson, T. Juettemann, A. K. Kähäri, S.

Keenan, F. J. Martin, T. Maurel, W. McLaren, D. N. Murphy, R. Nag, B. Overduin, A. Parker, M. Patricio, E. Perry, M. Pignatelli, H. S. Riat, D. Sheppard, K. Taylor, A. Thormann, A. Vullo, S. P. Wilder, A. Zadissa, B. L. Aken, E. Birney, J. Harrow, R. Kinsella, M. Muffato, M. Ruffier, S. M. J. Searle, G. Spudich, S. J. Trevanion, A. Yates, D. R. Zerbino, P. Flicek, Ensembl 2015. *Nucleic Acids Res.* **43**, D662-9 (2015).

98. A. Dobin, C. A. Davis, F. Schlesinger, J. Drenkow, C. Zaleski, S. Jha, P. Batut, M. Chaisson, T. R. Gingeras, STAR: ultrafast universal RNA-seq aligner. *Bioinformatics* **29**, 15–21 (2013).

99. B. Li, C. N. Dewey, RSEM: accurate transcript quantification from RNA-Seq data with or without a reference genome. *BMC Bioinformatics* **12**, 323 (2011).

100. J. Rappsilber, M. Mann, Y. Ishihama, Protocol for micro-purification, enrichment, pre-fractionation and storage of peptides for proteomics using StageTips. *Nat. Protoc.* **2**, 1896–1906 (2007).

101. B. MacLean, D. M. Tomazela, N. Shulman, M. Chambers, G. L. Finney, B. Frewen, R. Kern, D. L. Tabb, D. C. Liebler, M. J. MacCoss, Skyline: an open source document editor for creating and analyzing targeted proteomics experiments. *Bioinformatics* **26**, 966–968 (2010).

102. Y. Kawashima, E. Watanabe, T. Umeyama, D. Nakajima, M. Hattori, K. Honda, O. Ohara, Optimization of Data-Independent Acquisition Mass Spectrometry for Deep and Highly Sensitive Proteomic Analysis. *Int. J. Mol. Sci.* **20** (2019).

103. D. Amodei, J. Egertson, B. X. MacLean, R. Johnson, G. E. Merrihew, A. Keller, D. Marsh, O. Vitek, P. Mallick, M. J. MacCoss, Improving Precursor Selectivity in Data-Independent Acquisition Using Overlapping Windows. *J. Am. Soc. Mass Spectrom.* **30**, 669–684 (2019).

104. A. Hatano, M. Matsumoto, Sample preparation for phosphopeptides enrichment using Fe^{3+}-IMAC. *Journal of Proteome Data and Methods* **2**, 3 (2020).

105. R. Noguchi, H. Kubota, K. Yugi, Y. Toyoshima, Y. Komori, T. Soga, S. Kuroda, The selective control of glycolysis, gluconeogenesis and glycogenesis by temporal insulin patterns. *Mol. Syst. Biol.* **9**, 664 (2013).

106. J. Schindelin, I. Arganda-Carreras, E. Frise, V. Kaynig, M. Longair, T. Pietzsch, S. Preibisch, C. Rueden, S. Saalfeld, B. Schmid, J.-Y. Tinevez, D. J. White, V. Hartenstein, K. Eliceiri, P. Tomancak, A. Cardona, Fiji: an open-source platform for biological-image analysis. *Nat. Methods* **9**, 676–682 (2012).

107. J. D. Storey, A Direct Approach to False Discovery Rates. *J. R. Stat. Soc. Series B Stat. Methodol.* **64**, 479–498 (2002).

108. Y. Benjamini, Y. Hochberg, Controlling the false discovery rate: A practical and powerful approach to multiple testing. *J. R. Stat. Soc.* **57**, 289–300 (1995).

109. L. Garcia-Alonso, C. H. Holland, M. M. Ibrahim, D. Turei, J. Saez-Rodriguez, Benchmark and integration of resources for the estimation of human transcription factor activities. *Genome Res.* **29**, 1363–1375 (2019).

110. M. L. Miller, L. J. Jensen, F. Diella, C. Jørgensen, M. Tinti, L. Li, M. Hsiung, S. A. Parker, J. Bordeaux, T. Sicheritz-Ponten, M. Olhovsky, A. Pasculescu, J. Alexander, S. Knapp, N. Blom, P. Bork, S. Li, G. Cesareni, T. Pawson, B. E. Turk, M. B. Yaffe, S. Brunak, R. Linding, Linear motif atlas for phosphorylation-dependent signaling. *Sci. Signal.* **1**, ra2 (2008).

111. W. Shen, S. Le, Y. Li, F. Hu, SeqKit: A Cross-Platform and Ultrafast Toolkit for FASTA/Q File Manipulation. *PLoS One* **11**, e0163962 (2016).

112. R. Linding, L. J. Jensen, A. Pasculescu, M. Olhovsky, K. Colwill, P. Bork, M. B. Yaffe, T. Pawson, NetworKIN: a resource for exploring cellular phosphorylation networks. *Nucleic Acids Res.* **36**, D695-9 (2008).

113. A. Chang, L. Jeske, S. Ulbrich, J. Hofmann, J. Koblitz, I. Schomburg, M. Neumann-Schaal, D. Jahn, D. Schomburg, BRENDA, the ELIXIR core data resource in 2021: new developments and updates. *Nucleic Acids Res.* **49**, D498–D508 (2021).

114. E. W. Sayers, E. E. Bolton, J. R. Brister, K. Canese, J. Chan, D. C. Comeau, R. Connor, K. Funk, C. Kelly, S. Kim, T. Madej, A. Marchler-Bauer, C. Lanczycki, S. Lathrop, Z. Lu, F. Thibaud-Nissen, T. Murphy, L. Phan, Y. Skripchenko, T. Tse, J. Wang, R. Williams, B. W. Trawick, K. D. Pruitt, S. T. Sherry, Database resources of the national center for biotechnology information. *Nucleic Acids Res.* **50**, D20–D26 (2022).

115. D. S. Wishart, A. Guo, E. Oler, F. Wang, A. Anjum, H. Peters, R. Dizon, Z. Sayeeda, S. Tian, B. L. Lee, M. Berjanskii, R. Mah, M. Yamamoto, J. Jovel, C. Torres-Calzada, M. Hiebert-Giesbrecht, V. W. Lui, D. Varshavi, D. Varshavi, D. Allen, D. Arndt, N. Khetarpal, A. Sivakumaran, K. Harford, S. Sanford, K. Yee, X. Cao, Z. Budinski, J. Liigand, L. Zhang, J. Zheng, R. Mandal, N. Karu, M. Dambrova, H. B. Schiöth, R. Greiner, V. Gautam, HMDB 5.0: the Human Metabolome Database for 2022. *Nucleic Acids Res.* **50**, D622–D631 (2022).

116. J. Hastings, G. Owen, A. Dekker, M. Ennis, N. Kale, V. Muthukrishnan, S. Turner, N. Swainston, P. Mendes, C. Steinbeck, ChEBI in 2016: Improved services and an expanding collection of metabolites. *Nucleic Acids Res.* **44**, D1214-9 (2016).

117. UniProt Consortium, UniProt: the Universal Protein Knowledgebase in 2023. *Nucleic Acids Res.* **51**, D523–D531 (2023).

118. P. V. Hornbeck, B. Zhang, B. Murray, J. M. Kornhauser, V. Latham, E. Skrzypek, PhosphoSitePlus, 2014: mutations, PTMs and recalibrations. *Nucleic Acids Res.* **43**, D512-20 (2015).

119. B. H. Junker, C. Klukas, F. Schreiber, VANTED: a system for advanced data analysis and visualization in the context of biological networks. *BMC Bioinformatics* **7**, 109 (2006).

120. S. Okuda, Y. Watanabe, Y. Moriya, S. Kawano, T. Yamamoto, M. Matsumoto, T. Takami, D. Kobayashi, N. Araki, A. C. Yoshizawa, T. Tabata, N. Sugiyama, S. Goto, Y. Ishihama, jPOSTrepo: an international standard data repository for proteomes. *Nucleic Acids Res.* **45**, D1107–D1111 (2017).

FIGURE TITLES AND LEGENDS

Fig. 1: Workflow for the construction and analysis of a global starvation-responsive transomic network in liver of WT and *ob*/*ob* mice

(**A**) Experimental design. WT and *ob*/*ob* mice were starved for the indicated hours, followed by the collection of liver and plasma samples. These samples were subjected to multiomic measurements. It should be noted that metabolome was basically measured by CE-MS, but IC-QEMS was used for quantification of F1,6BP and F2,6BP. Enzymatic assay kit was used for glycogen. (**B**) Classification of molecules into 4 groups: commonly responsive in both WT and *ob*/*ob* mice (common, green); WT-specifically (WT-specific, blue); *ob*/*ob*-specifically (*ob/ob*-specific, red); oppositely (opposite, magenta) responsive molecules between WT mice and *ob*/*ob* mice. (**C**) Schema for a single-omic layer composed of responsive molecules classified as in (**B**). (**D**) Schema of regulatory input into the metabolic reactions. TFs increase or decrease metabolic enzyme abundance through gene regulation. Protein kinases increase or decrease enzyme phosphorylation to activate or inhibit enzyme activity. The metabolites, FFA & acyls, and lipids act as substrates, products, and allosteric regulators in metabolic reactions. The subset of the network that is defined as the starvation-responsive metabolic network is outlined in orange. (**E**) Schematic representation of the global starvation-responsive transomic network consisting of the indicated layers. The subset of the network that is defined as the starvation-responsive metabolic network is outlined in orange. (**F**) Structural properties of the starvation-responsive metabolic network in WT and *ob/ob* mice. (**G**) Temporal order of the starvation-responsive metabolic network in WT and *ob*/*ob* mice. (**H**) Temporal co-

regulations among the time courses molecules in the starvation-responsive metabolic network in WT and *ob*/*ob* mice.

Fig. 2: Single-omic layer analysis during starvation

(**A**-**C**) Identification and classification of starvation-responsive molecules. (**A**) One-way ANOVA tests ($P < 0.025$) defined starvation-responsive molecules. (**B**) Area under the curve (AUC) of log2-transformed mean time courses classified molecules into increased (AUC > 0, orange) and decreased (AUC < 0, purple) classes. (**C**) Classification of starvation-responsive molecules: common in both WT and *ob*/*ob* (either increased or decreased in both, green), WT-specific (blue), *ob*/*ob*-specific (red), or opposite (increased in WT and decreased in *ob*/*ob*, or vice versa, magenta). (**D**-**J**) The number of molecules and distribution in each group shown as pie charts colored as defined in (**C**). Increased or decreased molecules are indicated by the orange or purple arcs, respectively. The number and the ratio of significantly changed molecules of the molecules in each category are shown. Responsive metabolites (**D**), lipids (**E**), and FFA & acyls (**F**) in liver. Responsive plasma metabolites (**G**). Responsive transcripts (**H**), proteins (**I**), and phosphorylation events (**J**) in liver. (**K**) Strategy for inferring activities of upstream regulators and signaling pathways. Briefly, we constructed regulatory networks using database and identified increased and decreased downstream molecules from the measured data. In the case of positive regulators, we assumed that a regulator is activated if most of the downstream molecules increased and vice versa (see Methods). We screened regulators whose inferred activities were consistent with the measured data (see Methods). Activated or inhibited regulators were classified into common (green), WT-specific (blue), *ob*/*ob*-specific (red), or opposite (magenta)

groups. (**L**-**N**) The number and distribution of these inferred TFs (**L**), protein kinases (**M**), or signaling pathways (**N**) are shown in pie charts. *n* = 5 biological replicates per group.

Fig. 3: Global starvation-responsive transomic network

(**A**) An overview of the global starvation-responsive transomic network. Nodes in the layers represent metabolic reactions, transport activities, measured molecules, measured phosphorylation events, and the inferred activities of TF, protein kinase, and signaling pathway. Edges between the nodes represent regulatory relationships identified using bioinformatic platforms. Colors represent the responsiveness: green indicates common responses both in WT and *ob*/*ob* mice; blue, specific to WT mice; red, specific to *ob*/*ob* mice; magenta, opposite responses between the WT and *ob*/*ob* mice. For metabolic reaction and transport_activity layers, the classes were defined by the existences of regulations regardless of the regulatory directions (activation or inhibition): green indicates the node is regulated in both WT and *ob*/*ob* mice; blue, specific to WT mice; red, specific to *ob*/*ob* mice. (**B**) The proportions of nodes and edges classified as common (green), WT-specific (blue), *ob*/*ob*-specific (red), and opposite (magenta) in the global starvation-responsive transomic network. Pie charts represent the distribution of nodes in the omic layers, and bar plots between pie charts represent the distribution of edges between omic layers. Type of regulation into the metabolic reactions for metabolite, FFA& acyls, and lipid are indicated as allosteric regulation (denoted as “A”) and substrate and product (denoted as “S & P”). The starvation-responsive metabolic network is outlined in orange, and layer names included in the starvation-responsive metabolic networks are underlined.

Fig. 4: Starvation-responsive metabolic network

Projected views of the starvation-responsive metabolic networks in WT (**A**) and *ob*/*ob* mice (**B**). The network is composed of direct regulators of metabolic reactions: metabolites, lipids, FFA & acyls, enzyme_protein, and enzyme_PTM. Colors represent the responsiveness: green indicates common responses both in WT and *ob*/*ob* mice; blue, specific to WT mice; red, specific to *ob*/*ob* mice; magenta, opposite responses between the two genotypes. Hub nodes, which will be defined in Fig. 5, are labeled.

Fig. 5: Structural properties of the starvation-responsive metabolic network

(**A**) Degree distributions of the starvation-responsive metabolic network in WT (blue) and *ob*/*ob* (red) mice. The x-axis represents the log10-transformed degree (k); the y-axis represents the log10-transformed number of nodes with degree of k. Lines show the linear regression of the degree distributions. The slope of the lines (γ), which is defined as a scaling parameter, and the 95% credible interval are shown. n = 990 in WT and n = 721 in *ob*/*ob* mice for the number of nodes. (**B**) Diagram of a scale-free network, where $n(k)$ denotes the number of nodes with degree of k, and γ is a constant called a scaling parameter. Circles represent nodes; lines represent edges. Light blue represents the hub nodes; yellow represents leaf nodes. (**C** and **D**) Hub nodes with the top 2% highest degree in WT (**C**) and *ob*/*ob* mice (**D**). The x-axis represents hub nodes. The y-axis represents degrees. Colors represent the responsiveness: green indicates common responses both in WT and *ob*/*ob* mice; blue, specific to WT mice; red, specific to *ob*/*ob* mice; magenta, opposite responses between WT and *ob*/*ob* mice. (**E**) The number of edges (y-axis) from WT-specifically responsive hub nodes (blue), WT-specific nodes

2079 except for the hub nodes (light blue), *ob*/*ob*-specific hub nodes (red), *ob*/*ob*-specific
2080 nodes except for the hub nodes (light red), other nodes (commonly or oppositely
2081 responsive, gray). (**F**) Illustration of fragmentation of a network through loss of hub
2082 nodes. The largest cluster is orange. (**G**) Illustration of how communicability of a
2083 network influences average path length (average length of the shortest paths between all
2084 the pairs of nodes). (**H**) The relative size of the largest cluster in the starvation-
2085 responsive metabolic network in WT and *ob*/*ob* mice, calculated as the number of nodes
2086 in the largest cluster of the network divided by the total number of responsive nodes in
2087 the network for each genotype. (**I**) The average path length of the starvation-responsive
2088 metabolic network in WT and *ob*/*ob* mice. n = 853,884 paths in WT and n = 443,643
2089 paths in *ob*/*ob* mice. The error bars show standard deviation. P value of t-test is shown.
2090 (**J**) Time courses of ATP, AMP, and AMP/ATP ratio during starvation in WT and *ob*/*ob*
2091 mice. The x-axis represents the starvation time (hours) and the y-axis represents the
2092 concentration (nmol/mg-protein) for ATP and AMP, and ratio for AMP/ATP. Blue lines
2093 are the responses to starvation in WT mice, and red lines are those in *ob*/*ob* mice. Solid
2094 lines represent that the responses were significant; dotted lines represent no
2095 significance. Data are shown as the mean and SEM. Dots represent the data from
2096 individual mice. (**K**) Time courses of phosphorylation ratio of Akt and Ampk during
2097 starvation in WT and *ob*/*ob* mice. The x-axis represents the starvation time (hours) and
2098 the y-axis represents the phosphorylation ratio (the amount of phosphorylated protein
2099 divided by the total amount of protein) of Akt and Ampk. (**L**) Images of the western
2100 blotting analysis for (**K**) at the indicated starvation time (h) of the indicated genotype.
2101 IC represents internal control to normalize the signals across membranes. n = 5

2102 biological replicates per group. *P* values of one-way ANOVA of the molecules or ratio
2103 with significant changes are shown.
2104
2105 **Fig. 6: Temporal order of the starvation-responsive metabolic network in WT mice**
2106 **and its disruption in *ob*/*ob* mice**
2107 (**A** and **B**) Scatter plots for the log10-transformed degree (x-axis) and *t*-half (y-axis) in
2108 WT (**A**) and *ob*/*ob* (**B**) mice. Dots represent the molecules (including phosphorylation
2109 events) in the starvation-responsive metabolic network and colors denote the
2110 responsiveness: green indicates common responses both in WT and *ob*/*ob* mice; blue,
2111 specific to WT mice; red, specific to *ob*/*ob* mice; magenta, opposite responses between
2112 WT and *ob*/*ob* mice. Spearman's correlation coefficient (Rho) and *P* values are shown.
2113 Hub molecules for each genotype are labeled (see Fig. 5**C** and **D**). Time courses of
2114 increased and decreased molecules connected with few (1 ≤ degree < 10), relatively
2115 many (10 ≤ degree < 100), and many (100 ≤ degree) edges in WT (**A**) and *ob*/*ob* (**B**)
2116 mice are also shown. The x-axis represents starvation time (hours) and the y-axis
2117 represents the log2-transformed concentration to the concentrations before starvation of
2118 the molecules in each genotype. *n* = 291 molecules for WT and *n* = 163 molecules for
2119 *ob*/*ob* mice. (**C**) Values of *t*-half for the WT-specific and *ob*/*ob*-specific hub molecules
2120 (see Fig. 5**C** and **D**). The *P* value of Wilcoxon's rank sum test is shown. *n* = 15 hub
2121 molecules for WT and *n* = 10 hub molecules for *ob*/*ob* mice. (**D** and **E**) Distributions of
2122 *t*-half values of molecules (metabolites, lipids, FFA & acyls, proteins, and
2123 phosphorylation events) in the indicated metabolic pathways in WT (**D**) and *ob*/*ob* mice
2124 (**E**). The data are ordered along the x-axis by the median *t*-half (red line) with each
2125 molecule represented by a dot. *n* = 19, 10, 14, and 36 molecules in mice WT for

2126 “Glycolysis/gluconeogenesis”, “Starch and sucrose metabolism”, “Arginine
2127 biosynthesis”, and “Fatty acid degradation”. *n* = 5, 15, 13, and 3 molecules in *ob*/*ob*
2128 mice for “Starch and sucrose metabolism”, “Glycolysis/gluconeogenesis”, “Fatty acid
2129 degradation”, and “Arginine biosynthesis”. *P* values of the Kruskal-Wallis test are
2130 shown above the panels and those of the Dunn-Sidak test are shown above the lines
2131 indicating the pairs of metabolic pathways with significant differences ($P < 0.05$). (**F**)
2132 *Q*-values comparing *t*-half values of WT and *ob*/*ob* mice for each metabolic pathway.
2133 (**G** and **H**) Distributions of *t*-half values in each omic layer in the starvation-responsive
2134 metabolic network in WT (**G**) and in *ob*/*ob* (**H**) mice. The data are ordered along the x-
2135 axis by the median *t*-half (red line). *n* = 98, 47, 154, 2, and 23 molecules in mice WT for
2136 metabolite, enzyme_PTM, enzyme_protein, lipid, and FFA & acyls. *n* = 19, 75, 73, 15,
2137 and 10 molecules in *ob*/*ob* mice for enzyme_PTM, metabolite, enzyme_protein, FFA &
2138 acyls, and lipid. *P* values of the Kruskal-Wallis test are shown above the panels and
2139 those of the Dunn-Sidak test are shown above the lines indicating the pairs of omic
2140 layers with significant differences ($P < 0.05$).
2141
2142 **Fig. 7: Co-regulation among molecules in the starvation-responsive metabolic**
2143 **network and disruption in *ob*/*ob* mice**
2144 (**A**) Schematic representation of the analyses for co-regulation among the molecules in
2145 the starvation-responsive metabolic network. Time courses of molecules sharing a
2146 common regulatory mechanism could be positively or negatively correlated, defined as
2147 co-regulation. Pairwise Pearson’s correlation coefficients were calculated for the time
2148 courses of molecules that showed significant responses during starvation in the
2149 starvation-responsive metabolic network in WT and *ob*/*ob* mice. Positive correlation

2150 represents positive co-regulation and negative correlation represents negative co-
2151 regulation. (**B**) Distribution of the pairwise Pearson's correlation coefficients for time
2152 courses of responsive molecules in the starvation-responsive metabolic network in WT
2153 and *ob*/*ob* mice. The x-axis represents correlation coefficients; the y-axis represents the
2154 number of pairs of molecules examined for correlation. Pairs with an absolute value of
2155 correlation coefficient > 0.9 were connected by edges in the correlation metabolic
2156 network (see fig. S12). n = 324 molecules for WT mice, n = 192 molecules for *ob*/*ob*
2157 mice. (**C**) The absolute values of pairwise Pearson's correlation coefficients among time
2158 courses of responsive molecules in the indicated metabolic pathways in WT and *ob*/*ob*
2159 mice. The x-axis represents the absolute values of Pearson's correlation coefficient. The
2160 y-axis represents metabolic pathways and genotypes. Light blue dots represent the
2161 absolute values of pairwise Pearson's correlation coefficients among time courses of
2162 responsive molecules in each metabolic pathway of the starvation-responsive metabolic
2163 network. Red vertical lines indicate median, boxes the interquartile range (25th to 75th
2164 percentile), and whiskers 1.5 times the interquartile range. Red crosses represent
2165 outliers. Q-values comparing the correlation coefficients of WT and *ob*/*ob* mice by
2166 Wilcoxon rank sum test followed by FDR through Benjamini-Hochberg procedure are
2167 shown. The numbers of pairs of molecules are shown in the parenthesis. (**D** and **E**) The
2168 correlation metabolic network during starvation in WT (**D**) and *ob*/*ob* mice (**E**). Orange
2169 indicates the largest cluster; all other clusters are dark green. Individual orphan nodes
2170 with no connections are shown only by numbers.
2171
2172 **Fig. 8: Functional analysis of transcriptomic and proteomic data for potential**
2173 **clinical application**

2174 (**A**) Enrichment analysis of significantly changed transcripts in WT (blue circle) and

2175 *ob*/*ob* (red circle) mice using MSigDB. (**B**) Enrichment analysis of significantly

2176 changed proteins in WT (blue circle) and *ob*/*ob* (red circle) mice using MSigDB.

2177

SUPPLEMENTARY FIGURE TITLES AND LEGENDS

fig. S1: Time courses of responsive molecules during starvation

The x-axis represents the starvation time (hours) and the y-axis represents the concentration of the indicated molecule: ng/μg-protein for glycogen, nmol/mg-protein for other metabolites (F6P, Ala, 3-hydroxybutyrate); pmol/mg-protein for lipids (PS, PE, PI) and FFA & acyls (Acyl-CoA 16:0); arbitrary units for proteins (Cpt1a, Pck1, G6pc) and phosphorylation (Ser^{775} of Pfkl). TPM for transcripts (*Cpt1a*, *Pck1*, *G6pc*). Blue lines are the responses to starvation in WT mice, and red lines are those in *ob*/*ob* mice. Solid lines represent that the responses were significant; dotted lines represent no significance. Data are shown as the mean and SEM. Dots represent the data from individual mice. n = 5 biological replicates per group. P values of one-way ANOVA of the molecules or ratio with significant changes are shown.

fig. S2: Overview of each omic data

The heatmaps of the time courses of 123 responsive metabolites (liver, **A**), 10 responsive lipids (**B**), 27 responsive FFA & acyls (**C**), 60 responsive metabolites (plasma, **D**), 9,872 responsive transcripts (**E**), 663 responsive proteins (**F**), and 391 responsive phosphorylation events (**G**) of WT and *ob*/*ob* mice during starvation. For heatmap, two time courses for each molecule were divided by the geometric mean of the values of WT and *ob*/*ob* mice before starvation (0 h) and then log2-transformed. The x-axis represents time for starvation, and the y-axis represents the molecules or phosphorylation events. n = 5 biological replicates per group.

fig. S3: Regulatory relationships in the starvation-responsive transomic network

2202 We assumed that the starvation-responsive molecules cooperatively regulate metabolic
2203 reactions (see also Fig. 1**D**).
2204 (**A**) Metabolic network. The enzyme_protein (protein abundance of metabolic enzymes)
2205 and enzyme_PTM (phosphorylation events on metabolic enzymes) regulate metabolic
2206 reactions (identified with KEGG). Metabolites, lipids, and FFA & acyls regulate
2207 metabolic reactions as substrates, products (identified with KEGG), and allosteric
2208 regulators (identified with BRENDA). (**B**) Transport network identified with TCDB.
2209 The transporter_protein (protein abundance of transporters), transporter_PTM
2210 (phosphorylation events on transporters), and plasma metabolites regulate
2211 transport_activity (activities of transport). Transport_activity regulates metabolites in
2212 the liver, thereby regulating metabolic reactions in the liver. (**C**) Gene regulatory
2213 network identified with ChIP-Atlas and Ensembl. The TF_mRNA (mRNA abundance of
2214 TFs), TF_protein (protein abundance of TFs), and TF_PTM (phosphorylation events on
2215 TFs) regulate TF_activity (activities of TFs). TF_activity regulates enzyme_mRNA
2216 (mRNA abundance of metabolic enzymes) and transporter_mRNA (mRNA abundance
2217 of transporters). Enzyme_mRNA and transporter_mRNA regulate enzyme_protein and
2218 transporter_protein, respectively, and were aligned with Ensembl database. (**D**)
2219 Phosphorylation network identified with NetPhorest. The kinase_mRNA (mRNA
2220 abundance of kinases), kinase_protein (protein abundance of kinase), and kinase_PTM
2221 (phosphorylation events on kinases) regulate kinase_activity (activities of kinases). The
2222 kinase_activity regulates enzyme_PTM and transporter_PTM. (**E**) The number of
2223 metabolic reactions that lipids regulate as substrates, products, and/or allosteric
2224 regulators. The colors of the bars represent common responses (green), *ob*/*ob*-specific
2225 responses (red), and opposite responses (magenta) to starvation.

2226

2227 **fig. S4: Metabolic pathways regulated by the hub nodes**

2228 Heatmaps representing the number of regulated metabolic reactions in each metabolic
2229 pathway (x-axis) regulated by the hub nodes (y-axis) in the starvation-responsive
2230 metabolic network in WT (**A**) and *ob*/*ob* mice (**B**). Colors of the labels of the hub nodes
2231 represent the responsiveness: green indicates common responses both in WT and *ob*/*ob*
2232 mice; blue, specific to WT mice; red, specific to *ob*/*ob* mice; magenta, opposite
2233 responses between WT and *ob*/*ob* mice. KEGG metabolic pathways (x-axis) in
2234 carbohydrate metabolism (olive green), lipid metabolism (orange), nucleotide
2235 metabolism (brown), and amino acid metabolism (light blue) are displayed.

2236

2237 **fig. S5: Maintenance of the number of nodes with relatively large degrees in *ob*/*ob***
2238 **mice**

2239 The number of nodes (**A**-**E**) and the percentage of nodes to the number of responsive
2240 nodes in each genotype (**F**-**J**), whose log10-transformed degree are as indicated. (**K**)
2241 The percentages of nodes whose log10-transformed degree is more than 1.

2242

2243 **fig. S6: Identification of molecules essential for the negative correlation between**
2244 **degree and *t*-half in WT mice**

2245 (**A**) Schema for leave-one-out correlations. Log10-transformed degree negatively
2246 correlated with *t*-half in WT mice (center, "Rho of full"). The leave-one-out correlation
2247 of molecule X (left, "Rho without X") was defined as correlation coefficient between
2248 log10-transformed degree and *t*-half that was calculated for all the molecules except for
2249 X. The larger leave-one-out correlation (left, "Rho without X") represents the larger

2250 contribution to the negative correlation between log10-transformed degree and *t*-half.
2251 By contrast, the smaller leave-one-out correlation (right, "Rho without Y") represents
2252 the smaller contribution to the negative correlation between log10-transformed degree
2253 and *t*-half. (**B**) The cumulative leave-one-out correlation of molecule X (right) was
2254 defined by the correlation coefficient between log10-transformed degree and *t*-half that
2255 was calculated for the molecules with leave-one-out correlation smaller than X
2256 (indicated in light blue). (**C**) Leave-one-out correlations (gray bars), cumulative leave-
2257 one-out correlations (black dots), and *P*-values of the cumulative leave-one-out
2258 correlations (black solid line) of the indicated molecules. Here, we displayed molecules
2259 with *P*-values of the cumulative leave-one-out correlations that were less than 0.05 and
2260 with leave-one-out correlations that were less than other molecules. $n = 291$ molecules
2261 in total.
2262
2263 **fig. S7: The starvation-responsive metabolic network for starvation-responsive**
2264 **metabolic reactions in fatty acid degradation**
2265 (**A**) Time courses of fatty acids as substrates, acyl-CoAs and acyl-carnitines as
2266 intermediates, and 3-Hydroxybutyrate (a ketone body) as a product of fatty acid
2267 degradation. Gray lines indicate the time courses of molecules in each group in each
2268 genotype. Solid lines represent significantly responsive molecules, while dashed lines
2269 represent not significantly responsive molecules. Bold and colored lines represent mean
2270 and STD of the time courses of the significantly responsive molecules. The total
2271 numbers of molecules are shown in parentheses following to the names of the molecule
2272 types. The numbers of significantly changed molecules in each genotype are shown in
2273 parentheses following to the label for genotype. (**B**) The transomic network for

2274 starvation-responsive metabolic reactions in fatty acid degradation, that were manually
2275 constructed based on "Fatty acid degradation" (mmu00071), "Propanoate metabolism"
2276 (mmu00640), and "Butanoate metabolism" (mmu00650) in the KEGG database (*55*–
2277 *57*). Time courses of measured metabolites, lipids, FFA & acyls, enzyme_protein, and
2278 enzyme_PTM are shown for corresponding nodes as the mean and SEM. $n = 5$
2279 biological replicates per group. The colors of the frames represent common responses
2280 (green), WT-specific responses (blue), *ob*/*ob*-specific responses (red), and opposite
2281 responses (magenta) to starvation. The black frames indicate that were not responsive to
2282 starvation. From metabolites, lipids, and FFA & acyls to metabolic reactions, only
2283 allosteric regulatory connections are colored. (**C**) The *t*-half values of the indicated
2284 types of molecules in WT and *ob*/*ob* mice. The x-axis represents molecule types and
2285 genotypes. The y-axis represents *t*-half values. Light blue dots represent *t*-half values of
2286 each molecule. Red horizontal lines indicate median, boxes the interquartile range (25th
2287 to 75th percentile), and whiskers 1.5 times the interquartile range. Red crosses represent
2288 outliers. *Q*-value less than 0.1 for the differences of *t*-half values between WT and *ob*/*ob*
2289 mice by Wilcoxon rank sum test followed by FDR using Benjamini-Hochberg
2290 procedure is shown. The number of molecules in each category is shown in parentheses
2291 following to the genotype label. (**D**) The number of responsive molecules of the
2292 indicated molecule types in WT and *ob*/*ob* mice. Blue represents WT and red represents
2293 *ob*/*ob* mice. The x-axis represents molecule types and genotypes. The y-axis represents
2294 the number of responsive molecules. (**E**) The distribution of Pearson's correlation
2295 coefficients between the time courses of enzyme_mRNA and enzyme_protein for each
2296 metabolic enzyme involved in fatty acid degradation, whose mRNA and protein were
2297 both measured in our transcriptome and proteome data. The x-axis represents genotype

2298 and the y-axis represents Pearson's correlation coefficient. The *P*-value calculated by
2299 two-sample *t*-test comparing the correlation coefficients of WT and *ob*/*ob* mice is
2300 shown. *n* = 13 commonly measured molecules both in transcriptome and proteome that
2301 fatty acid degradation map (fig. S7**B**) includes.
2302
2303 **fig. S8: Activities of protein translation and degradation in *ob*/*ob* mice**
2304 (**A**) Phosphorylation ratio of eIF2α in WT and *ob*/*ob* mice before starvation. The x-axis
2305 represents genotype and the y-axis represents the ratio of phosphorylated eIF2α to total
2306 eIF2α. The *P*-value of a two-sample *t*-test comparing the phosphorylation ratios of
2307 eIF2α between WT and *ob*/*ob* mice is shown. (**B**) Images of western blotting for (**A**).
2308 (**C**) The time course of phosphorylation ratio of p62 in WT (blue line) and *ob*/*ob* mice
2309 (red line). The x-axis represents starvation time (h) and the y-axis represents ratio of
2310 phosphorylated p62 to total p62. The solid line represents that the response was
2311 significant; the dotted line represents no significance. Data are shown as the mean and
2312 SEM. Dots represent the data from individual mice. *P* value of one-way ANOVA of
2313 ratio-pp62 with significant changes is shown. (**D**) Images of western blotting for (**C**) at
2314 the indicated starvation time (h) of the indicated genotype. IC represents internal control
2315 to normalize the signals across membranes. Arrowheads indicate the total and
2316 phosphorylated p62 bands. *n* = 5 biological replicates per group.
2317
2318 **fig. S9: The starvation-responsive metabolic network for starvation-responsive**
2319 **metabolic reactions in glycolysis/gluconeogenesis**
2320 The starvation-responsive metabolic network for starvation-responsive metabolic
2321 reactions in glycolysis/gluconeogenesis, that were manually constructed based on

2322 “Glycolysis/gluconeogenesis” (mmu00010) in the KEGG database (*55–57*), in WT (**A**)
2323 and *ob*/*ob* (**B**) mice. Time courses of measured metabolites, lipids, FFA & acyls,
2324 enzyme_protein, and enzyme_PTM are shown for corresponding nodes as the mean and
2325 SEM. n = 5 biological replicates per group. The colors of the frames represent common
2326 responses (green), WT-specific responses (blue), *ob*/*ob*-specific responses (red), and
2327 opposite responses (magenta) to starvation. The black frames indicate that were not
2328 responsive to starvation. From metabolites, lipids, and FFA & acyls to metabolic
2329 reactions, only allosteric regulatory connections are colored. (**C** and **D**) The degree of
2330 the indicated nodes in WT (**C**) and in *ob*/*ob* (**D**) mice. Nodes with degree more than 4
2331 are shown. The x-axis represents degree (the number of edges) and the y-axis represents
2332 nodes. It should be noted that the degrees shown in **C** and **D** are not necessarily
2333 identical to those shown in **A** and **B.** This is because if a molecule regulates a metabolic
2334 reaction both as a substrate or product, and as an allosteric regulator, the edges were
2335 counted as a single edge in **C** and **D**, but were shown separately in **A** and **B**. (**E**) Degree
2336 distributions of the nodes in the starvation-responsive metabolic network of
2337 glycolysis/gluconeogenesis in WT (blue) and *ob*/*ob* (red) mice. The x-axis represents
2338 the log10-transformed degree (k); the y-axis represents the log10-transformed number
2339 of nodes with degree of k. Lines show the linear regression of the degree distributions.
2340 The slope of the lines (γ), which is defined as a scaling parameter, and the 95% credible
2341 interval are shown. n = 49 molecules for WT mice and n = 37 molecules for *ob*/*ob* mice.
2342 (**F** and **G**) Scatter plots for the log10-transformed degree (x-axis) and *t*-half (y-axis) in
2343 WT (**F**) and *ob*/*ob* (**G**) mice. Dots represent the molecules (including phosphorylation
2344 events) in the starvation-responsive metabolic network of glycolysis/gluconeogenesis.
2345 Blue dots represent WT and red dots represent *ob*/*ob* mice. Spearman’s correlation

2346 coefficients (Rho) and *P* values are shown. *n* = 49 molecules for WT mice and *n* = 37
2347 molecules for *ob*/*ob* mice. (**H**) Distribution of the pairwise Pearson's correlation
2348 coefficients among time courses of responsive molecules in the starvation-responsive
2349 metabolic network of glycolysis/gluconeogenesis in WT and *ob*/*ob* mice. The x-axis
2350 represents correlation coefficients; the y-axis represents the number of pairs of
2351 molecules examined for correlation. *n* = 49 molecules for WT mice and *n* = 37
2352 molecules for *ob*/*ob* mice.
2353
2354 **fig. S10: The starvation-responsive metabolic network for starvation-responsive**
2355 **metabolic reactions in urea cycle**
2356 The starvation-responsive metabolic network for starvation-responsive metabolic
2357 reactions in urea cycle, that were manually constructed based on "Arginine
2358 biosynthesis" (mmu00220) in the KEGG database (*55–57*) (**A**). Time courses of
2359 measured metabolites, lipids, FFA & acyls, enzyme_protein, and enzyme_PTM are
2360 shown for corresponding nodes as the mean and SEM. The colors of the frames
2361 represent common responses (green), WT-specific responses (blue), *ob*/*ob*-specific
2362 responses (red), and opposite responses (magenta) to starvation. The black frames
2363 indicate that were not responsive to starvation. From metabolites, lipids, and FFA &
2364 acyls to metabolic reactions, only allosteric regulatory connections are colored. (**B** and
2365 **C**) The degree of the indicated nodes in WT (**B**) and in *ob*/*ob* (**C**) mice. Nodes with
2366 degree more than 2 are shown. The x-axis represents degree (the number of edges) and
2367 the y-axis represents nodes. It should be noted that the degrees shown in **B** and **C** are
2368 not necessarily identical to those shown in **A.** This is because if a molecule regulates a
2369 metabolic reaction both as a substrate or product, and as an allosteric regulator, the

edges were counted as a single edge in **B** and **C**, but were shown separately in **A**. (**D**) Degree distributions of the nodes in the starvation-responsive metabolic network of urea cycle in WT (blue) and *ob*/*ob* (red) mice. The x-axis represents the log10-transformed degree (k); the y-axis represents the log10-transformed number of nodes with degree of k. Lines show the linear regression of the degree distributions. The slope of the lines (γ), which is defined as a scaling parameter, and the 95% credible interval are shown. n = 40 molecules for WT mice and n = 22 molecules for *ob*/*ob* mice. (**E** and **F**) Scatter plots for the log10-transformed degree (x-axis) and t-half (y-axis) in WT (**E**) and *ob*/*ob* (**F**) mice. Dots represent the molecules (including phosphorylation events) of the starvation-responsive metabolic network in urea cycle. Blue dots represent WT and red dots represents *ob*/*ob* mice. Spearman's correlation coefficients (Rho) and P values are shown. n = 40 molecules for WT mice and n = 22 molecules for *ob*/*ob* mice. (**G**) Distribution of the pairwise Pearson's correlation coefficients among time courses of responsive molecules in the starvation-responsive metabolic network of urea cycle in WT and *ob*/*ob* mice. The x-axis represents correlation coefficients; the y-axis represents the number of pairs of molecules examined for correlation. n = 40 molecules for WT mice and n = 22 molecules for *ob*/*ob* mice.

fig. S11: Distribution of the pairwise Pearson's correlation coefficients among time courses of all the measured metabolites, lipids, FFA & acyls, enzyme_protein, and enzyme_PTM

The x-axis represents the pairwise Pearson's correlation coefficients among time courses of all the measured metabolites, lipids, FFA & acyls, enzyme_protein and enzyme_PTM; the y-axis represents the number of pairs of molecules examined for

correlation. The data of WT (**A**) and *ob*/*ob* (**B**) mice are shown. n = 5,866 molecules in each genotype.

fig. S12: The correlation metabolic network during starvation

(**A**) Scatter plots showing the degree distributions of correlation metabolic network corresponding to each threshold of absolute values of correlation coefficients (|Rho|) ranging from 0.3 to 0.9. The x-axis represents $\log_{10}(k)$, the log10-transformed degree; the y-axis represents $\log_{10}(n(k))$, the log10-transformed number of nodes with degree of k. Dots denote the degree distribution of the indicated networks and lines show the linear-regression of the degree distribution. The scaling parameters (γ) and the 95% credible interval are shown. Data for WT and *ob*/*ob* mice are shown. The number of clusters (**B**), relative size of the largest cluster (**C**) and the average path length (**D**) for each threshold are also shown. The lower threshold than 0.8 for the absolute value of correlation coefficients resulted in formation of a single cluster (**B**). The higher threshold (0.8 or 0.9) for the absolute value of correlation coefficients resulted in more scale-free-like networks. To identify the qualitative differences between WT and *ob*/*ob* mice clearly, we used 0.9 as a threshold for the absolute value of correlation coefficients in Fig. 7**D** and **E**. Using 0.9 as a threshold for the absolute value of correlation coefficients, the relative size of the largest cluster was smaller (**C**) and the average path length was larger in *ob*/*ob* mice than in WT mice (**D**). For average path length, the numbers of the investigated paths are shown in parentheses following to the genotype label. The error bars show standard deviation.

Tables and legends

Omics type	Maximum *Q*-value
Metabolome (Liver)	0.0029
Transcriptome	0.0489
Proteome	0.0661
Phosphoproteome	0.1645
Lipidome	0.0502
FFA & acyls	0.053
Metabolome (Plasma)	0.0016

Table 1. Maximum *Q*-values for the omic layers of the starvation-responsive molecules.

Maximum *Q*-values for each omic layer for molecules with *P*-values less than 0.025. All the maximum *Q*-values were less than 0.1 except for phosphoproteome, suggesting that false discovery rates of the starvation-responsive molecules were less than 0.1 in all the omic layers except for phosphoproteome.

Common name	Abbreviation
Lysophosphatidylcholine	LPC
Lysophosphatidylethanolamine	LPE
Cholesterol	Chol
Phosphatidylethanolamine	PE
Triacylglycerol	TG
Ceramide	Cer
Diacylglycerol	DG
Monoacylglycerol	MG
Phosphatidic acid	PA
Phosphatidylcholine	PC
Phosphatidylglycerol	PG
Phosphatidylinositol	PI
Phosphatidylserine	PS
Sphingomyelin	SM
Cholesterol ester	CE
Hexose ceramide	HexCer

Table 2. Measured lipid classes

Measured lipid classes and their abbreviations.

	WT	*ob*/*ob*
Increased	Fatty acid degradation, Lysine degradation, Glycerolipid metabolism, Biosynthesis of unsaturated fatty acids, PPAR signaling pathway, Peroxisome, Fat digestion and absorption	PPAR signaling pathway, Fat digestion and absorption
Decreased	Pentose and glucuronate interconversions, Ascorbate and aldarate metabolism, Steroid biosynthesis, Steroid hormone biosynthesis, Tyrosine metabolism, Selenocompound metabolism, Glutathione metabolism, Thiamine metabolism, Retinol metabolism, Porphyrin metabolism, Terpenoid backbone biosynthesis, Sulfur metabolism, Metabolism of xenobiotics by cytochrome P450, Drug metabolism - cytochrome P450, Drug metabolism - other enzymes, ABC transporters, Protein export, Mismatch repair, Protein processing in endoplasmic reticulum, Necroptosis, Cellular senescence, Signaling pathways regulating pluripotency of stem cells, RIG-I-like receptor signaling pathway, Serotonergic synapse, Prolactin signaling pathway, Bile secretion	Glycolysis / Gluconeogenesis, Pentose phosphate pathway, Fructose and mannose metabolism, Fatty acid biosynthesis, Steroid biosynthesis, Steroid hormone biosynthesis, Glycine, serine and threonine metabolism, Tryptophan metabolism, Selenocompound metabolism, Glutathione metabolism, Starch and sucrose metabolism, Amino sugar and nucleotide sugar metabolism, Pyruvate metabolism, Glyoxylate and dicarboxylate metabolism, One carbon pool by folate, Nicotinate and nicotinamide metabolism, Retinol metabolism, Porphyrin metabolism, Terpenoid backbone biosynthesis, Sulfur metabolism, Aminoacyl-tRNA biosynthesis, Metabolism of xenobiotics by cytochrome P450, Drug metabolism - cytochrome P450, Drug metabolism - other enzymes, Biosynthesis of unsaturated fatty acids, ABC transporters, DNA replication, Protein export, Base excision repair, Mismatch repair, Non-homologous end-joining, Protein processing in endoplasmic reticulum, Peroxisome, AMPK signaling pathway, Longevity regulating pathway, Thermogenesis, Phototransduction, Insulin signaling pathway

Table 3. KEGG pathway enrichment analysis of the starvation-responsive transcripts

KEGG pathways with *Q*-value < 0.1 are shown.

	WT	*ob*/*ob*
Increased	Citrate cycle (TCA cycle), Fatty acid degradation, Arginine biosynthesis, Valine, leucine and isoleucine degradation, Phenylalanine metabolism, Phenylalanine, tyrosine and tryptophan biosynthesis, beta-Alanine metabolism, Propanoate metabolism, PPAR signaling pathway	Ribosome, Lysosome
Decreased	Pentose and glucuronate interconversions, Ascorbate and aldarate metabolism, Steroid hormone biosynthesis, Glutathione metabolism, One carbon pool by folate, Retinol metabolism, Porphyrin metabolism, Metabolism of xenobiotics by cytochrome P450, Drug metabolism - cytochrome P450, Drug metabolism - other enzymes, Protein processing in endoplasmic reticulum, Antigen processing and presentation, Serotonergic synapse	No enrichment

Table 4. KEGG pathway enrichment analysis of the starvation-responsive proteins

KEGG pathways with Q-value < 0.1 are shown.

WT	*ob*/*ob*	TFs
Up	Up	Arntl, Clock, Cry1, Egr1, Ep300, Foxa3, Hnf4a, Myc, Nelfa, Nfil3, Ppara, Prox1, Rorc, Stat3, Stat5a, Tead1, Yap1
Up	NE	Cebpb, Crebbp, Hdac3, Med1, Rad21, Rora
Up	Down	Klf15
NE	Up	Hsf1, Nr1h4, Pbrm1, Rela
NE	Down	Gps2, Gtf2e2
Down	Up	Bcl6, Foxa1, Gata4, Ncoa3
Down	NE	Ctbp2, Cux2, Foxa2, Nr1h3, Nr3c1, Onecut1, Rxra, Tead4
Down	Down	Ahr, Cebpa, Creb1, Dbp, E2f1, Esr1, Mlxipl, Ncor1, Nfe2l2, Nr1d1, Nr1d2, Pparg, Srebf1, Ssu72, Xbp1

Table 5. Activated or inhibited TFs during starvation

Activated or inhibited TFs during starvation. ‘Up’, ‘Down’, and ‘NE’ represent activation, inhibition, and no enrichment, respectively.

WT	*ob*/*ob*	Protein kinases
Up	Up	NE
Up	NE	NE
Up	Down	NE
NE	Up	NE
NE	Down	NEK1_NEK5_NEK3_NEK4_NEK11_NEK2_group
Down	Up	NE
Down	NE	CaMKII_group, PAK_group, PDHK_group, PKD_group, SLK_group
Down	Down	PKC_group

Table 6: Activated or inhibited protein kinase groups during starvation

Activated or inhibited protein kinase groups during starvation. ‘Up’, ‘Down’, and ‘NE’ represent activation, inhibition, and no enrichment, respectively.

WT	*ob*/*ob*	Signaling pathways
Up	Up	PPAR signaling pathway
Up	NE	NE
Up	Down	NE
NE	Up	NE
NE	Down	AMPK signaling pathway, Insulin signaling pathway
Down	Up	NE
Down	NE	Prolactin signaling pathway, RIG-I-like receptor signaling pathway, Signaling pathways regulating pluripotency of stem cells
Down	Down	NE

Table 7: Activated or inhibited signaling pathways during starvation

Activated or inhibited signaling pathways during starvation. ‘Up’, ‘Down’, and ‘NE’ represent activation, inhibition, and no enrichment, respectively.

Layer name	Chemical property	Biological function	Omic
metabolite	metabolite	metabolite	metabolome
metabolic reaction	-	metabolic reaction	inference
enzyme_mRNA	mRNA	enzyme	transcriptome
enzyme_protein	protein	enzyme	proteome
enzyme_PTM	PTM	enzyme	phosphoproteome
TF_mRNA	mRNA	TF	transcriptome
TF_protein	protein	TF	proteome
TF_PTM	PTM	TF	phosphoproteome
TF_activity	-	TF	inference
kinase_mRNA	mRNA	kinase	transcriptome
kinase_protein	protein	kinase	proteome
kinase_PTM	PTM	kinase	phosphoproteome
kinase_activity	-	kinase	inference
signaling_activity	-	signaling pathway	inference
transporter_mRNA	mRNA	transporter	transcriptome
transporter_protein	protein	transporter	proteome
transporter_PTM	PTM	transporter	phosphoproteome
transporter_activity	-	transporter	inference
lipid	lipid	lipid	lipidome
bloodmetabolite	metabolite	metabolite in blood	metabolome
FFA & acyls	fatty acid, acyl-CoA, acyl-carnitine	FFA & Acyls	fatty acid, acyl-CoA, acyl-carnitine

Table 8: Omic layers in the global starvation-responsive metabolic network

Classification of molecules or inferred regulators into omic layers, biological function, or chemical property.

TITLES AND LEGENDS FOR SUPPLEMENTARY TABLES

Data File S1: All the analyzed data

This file includes all the analyzed data (metabolite, lipid, FFA & acyls, protein, phosphorylation, transcript, plasma metabolite, and western blotting), that were quantified in more than half of replicates in both WT and *ob*/*ob* mice at all the time points after food removal. Raw transcriptome data, raw proteome data, and raw phosphoproteome data are uploaded on public repositories (see Data and code availability section). All measured metabolome, lipidome, and FFA & acyls data are included in Data File S9. The columns represent biological samples (S25-S104), whose biological conditions are summarized in 'Sample_information' tab. The rows represent molecules or phosphorylation events. The units were nmol/mg-protein for metabolites except for glycogen, ng/μg-protein for glycogen, μM for plasma metabolites, pmol/mg-protein for lipids and FFA & acyls, TPM for transcripts, and arbitrary units for protein ~~and~~ phosphorylation, and western blotting.

Data File S2: Properties of the analyzed molecules

This file includes properties of the time courses (AUC and *t*-half), and results of statistical tests. The columns the names of properties of the time courses (AUC and *t*-half) and the results of statistical test (*P*-values, *Q*-values, and changes). The rows represent molecules. Abbreviations for WT_change and *ob*/*ob*-change columns were as follows: Up, Down, and NS represent increase, decrease and no significant changes.

Data File S3: KEGG Pathway Enrichment Analyses

This file includes all the results of Fisher's exact test in KEGG Pathway Enrichment

Analyses for transcriptome, proteome, and phosphoproteome data. The Entry, Name, Class, and Subclass are displayed for the information of each pathway. *P*-values, *Q*-values, and odds ratio for Fisher's exact test, and significantly changed downstream molecules are listed.

Data File S4: TF and kinase enrichment analyses

This file includes all the results of TF/kinase enrichment analysis for increased or decreased transcripts/phosphorylation events in WT and *ob*/*ob* mice, respectively. For TF, Fisher's exact tests were conducted for each ChIP-seq experiment. The table contains experimental IDs, name of TFs, organ, and cell for the information of ChIP-experiments. Also, *P*-values, *Q*-values, and odds ratio for Fisher's exact test are displayed. For protein kinases, names of kinase groups, ENSMUSG IDs of kinases, and names of kinases were displayed. Also, *P*-values, *Q*-values, and odds ratio are listed.

Data File S5: The global starvation responsive transomic network

This file includes all the information of nodes and edges of the global starvation-responsive transomic network. The node tab includes information of node; IDs, names, omic layers, changes in WT and *ob*/*ob* mice, and comparisons between them (common responses both in WT and *ob*/*ob* mice; specific to WT mice; specific to *ob*/*ob* mice; opposite responses between the two genotypes). The edge tab includes the layers and IDs of the source and target nodes, the type of regulation (Act: activation or Inh: inhibition), and the presence or absence of the regulation in WT and *ob*/*ob* mice (TRUE or FALSE).

Data File S6: The starvation responsive metabolic network

This file includes all the information of nodes and edges of the starvation-responsive metabolic network. The node tab includes information of node: names, IDs, omic layers, significance of responses to starvation in WT and *ob*/*ob* mice (TRUE or FALSE), AUC of the time courses in WT and *ob*/*ob* mice, *t*-half in WT and *ob*/*ob* mice, and degrees and cluster IDs of the background network (network of the database) and starvation-responsive metabolic networks in WT and *ob*/*ob* mice. The edge tab includes the layers and IDs of the source and target nodes, the type of regulation (Act: activation or Inh: inhibition), and the presence or absence of the regulation in WT and *ob*/*ob* mice (TRUE or FALSE).

Data File S7: The correlation metabolic network during starvation

This file includes all the pairwise correlation coefficients among time courses of molecules in the starvation-responsive metabolic networks. Each tab represents WT or *ob*/*ob* mice. Both the columns and rows represent responsive molecules in the starvation-responsive metabolic network in WT and *ob*/*ob* mice. The pairwise correlation coefficients are displayed as a matrix in each tab.

Data File S8: MSigDB Enrichment Analyses

This file includes all the results of Fisher's exact test in MSigDB Enrichment Analyses for transcriptome and proteome data. *P*-values, *Q*-values, and odds ratio for Fisher's exact test, and significantly changed downstream molecules are provided for each Hallmark.

Data File S9: All the metabolome, lipidome, and FFA & acyls data

This file includes all data of metabolome, lipidome (including FFA), acyl-carnitines, and acyl-CoAs. The columns represent biological samples (S25-S104), whose biological conditions are summarized in 'Sample_information' tab. The rows represent molecules. The units were nmol/mg-protein for metabolites, pmol/mg-protein for lipids including FFA, acyl-carnitine, and acyl-CoA. Most metabolites were measured by CE-MS, while F1,6P and F2,6P were separately measured by IC-QEMS. F1,6P was quantified both in CE-MS and IC-QEMS. We used values of IC-QEMS in this study.

Data File S10: Kinase names and ENSMUSG IDs of all the kinase groups in NetPhorest

Kinase names, kinase groups and ENSMUSG IDs of protein kinases were displayed in this table.

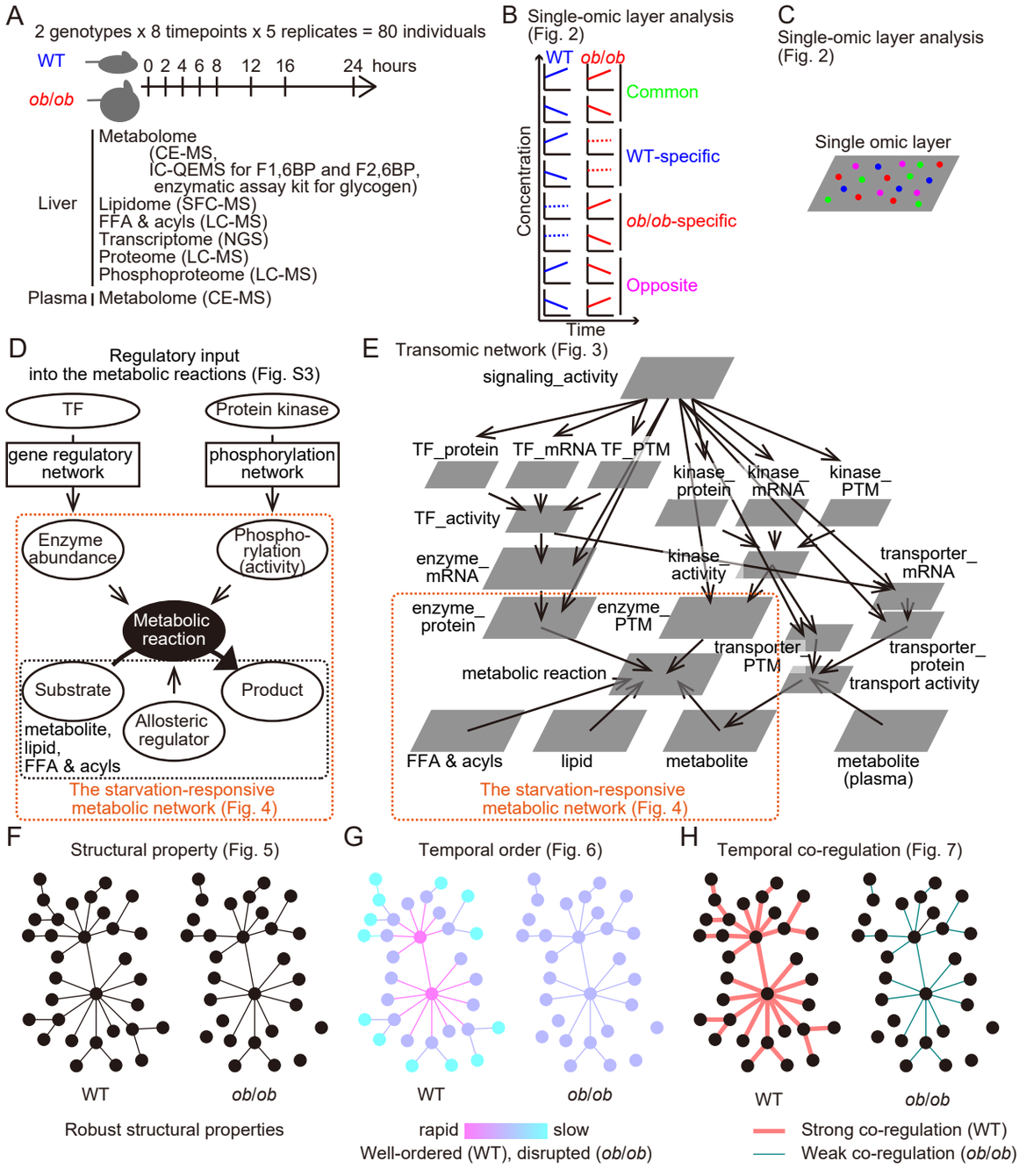

Fig. 1: Workflow for the construction and analysis of a global starvation-responsive transomic network in liver of WT and *ob*/*ob* mice

(A) Experimental design. WT and *ob*/*ob* mice were starved for the indicated hours, followed by the collection of liver and plasma samples. These samples were subjected to multiomic measurements. It should be noted that metabolome was basically measured by CE-MS, but IC-QEMS was used for quantification of F1,6BP and F2,6BP. Enzymatic assay kit was used for glycogen. (B) Classification of molecules into 4 groups: commonly responsive in both WT and *ob*/*ob* mice (common, green); WT-specifically (WT-specific, blue); *ob*/*ob*-specifically (*ob*/*ob*-specific, red); oppositely (opposite, magenta) responsive molecules between WT mice and *ob*/*ob* mice. (C) Schema for a single-omic layer composed of responsive molecules classified as in (B). (D) Schema of regulatory input into the metabolic reactions. TFs increase or decrease metabolic enzyme abundance through gene regulation. Protein kinases increase or decrease enzyme phosphorylation to activate or inhibit enzyme activity. The metabolites, FFA & acyls, and lipids act as substrates, products, and allosteric regulators in metabolic reactions. The subset of the network that is defined as the starvation-responsive metabolic network is outlined in orange. (E) Schematic representation of the global starvation-responsive transomic network consisting of the indicated layers. The subset of the network that is defined as the starvation-responsive metabolic network is outlined in orange. (F) Structural properties of the starvation-responsive metabolic network in WT and *ob*/*ob* mice. (G) Temporal order of the starvation-responsive metabolic network in WT and *ob*/*ob* mice. (H) Temporal co-regulations among time courses of molecules in the starvation-responsive metabolic network in WT and *ob*/*ob* mice.

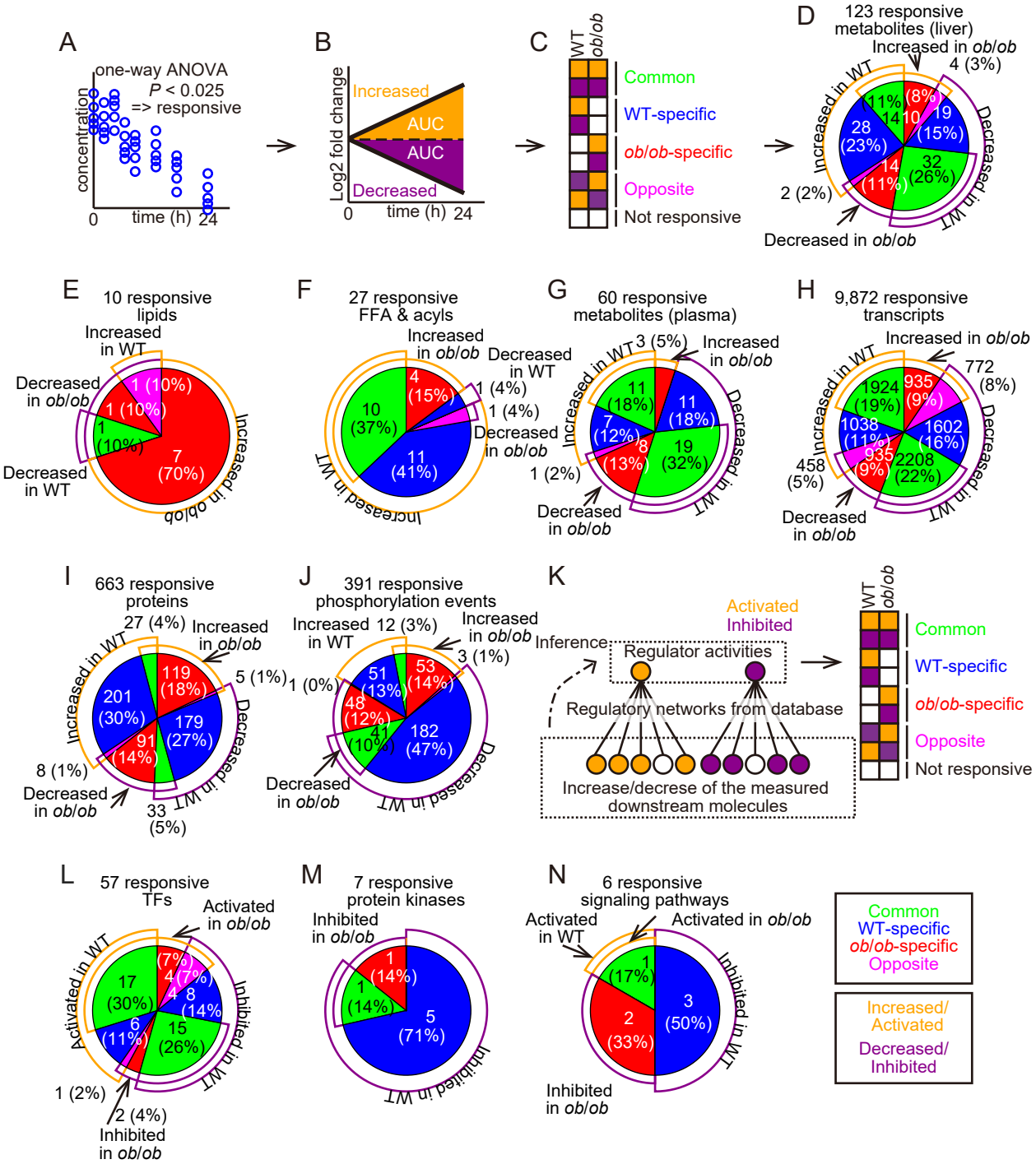

Fig. 2: Single-omic layer analysis during starvation

(A-C) Identification and classification of starvation-responsive molecules. (A) One-way ANOVA tests (P < 0.025) defined starvation-responsive molecules. (B) Area under the curve (AUC) of log2-transformed mean time courses classified molecules into increased (AUC > 0, orange) and decreased (AUC < 0, purple) classes. (C) Classification of starvation-responsive molecules: common in both WT and *ob*/*ob* (either increased or decreased in both, green), WT-specific (blue), *ob*/*ob*-specific (red), or opposite (increased in WT and decreased in *ob*/*ob*, or vice versa, magenta). (D-J) The number of molecules and distribution in each group shown as pie charts colored as defined in (C). Increased or decreased molecules are indicated by the orange or purple arcs, respectively. The number and the ratio of significantly changed molecules of the molecules in each category are shown. Responsive metabolites (D), lipids (E), and FFA & acyls (F) in liver. Responsive plasma metabolites (G). Responsive transcripts (H), proteins (I), and phosphorylation events (J) in liver. (K) Strategy for inferring activities of upstream regulators and signaling pathways. Briefly, we constructed regulatory networks using database and identified increased and decreased downstream molecules from the measured data. In the case of positive regulators, we assumed that a regulator is activated if most of the downstream molecules increased and vice versa (see Methods). We screened regulators whose inferred activities were consistent with the measured data (see Methods). Activated or inhibited regulators were classified into common (green), WT-specific (blue), *ob*/*ob*-specific (red), or opposite (magenta) groups. (L-N) The number and distribution of these inferred TFs (L), protein kinases (M), or signaling pathways (N) are shown in pie charts. n = 5 biological replicates per group.

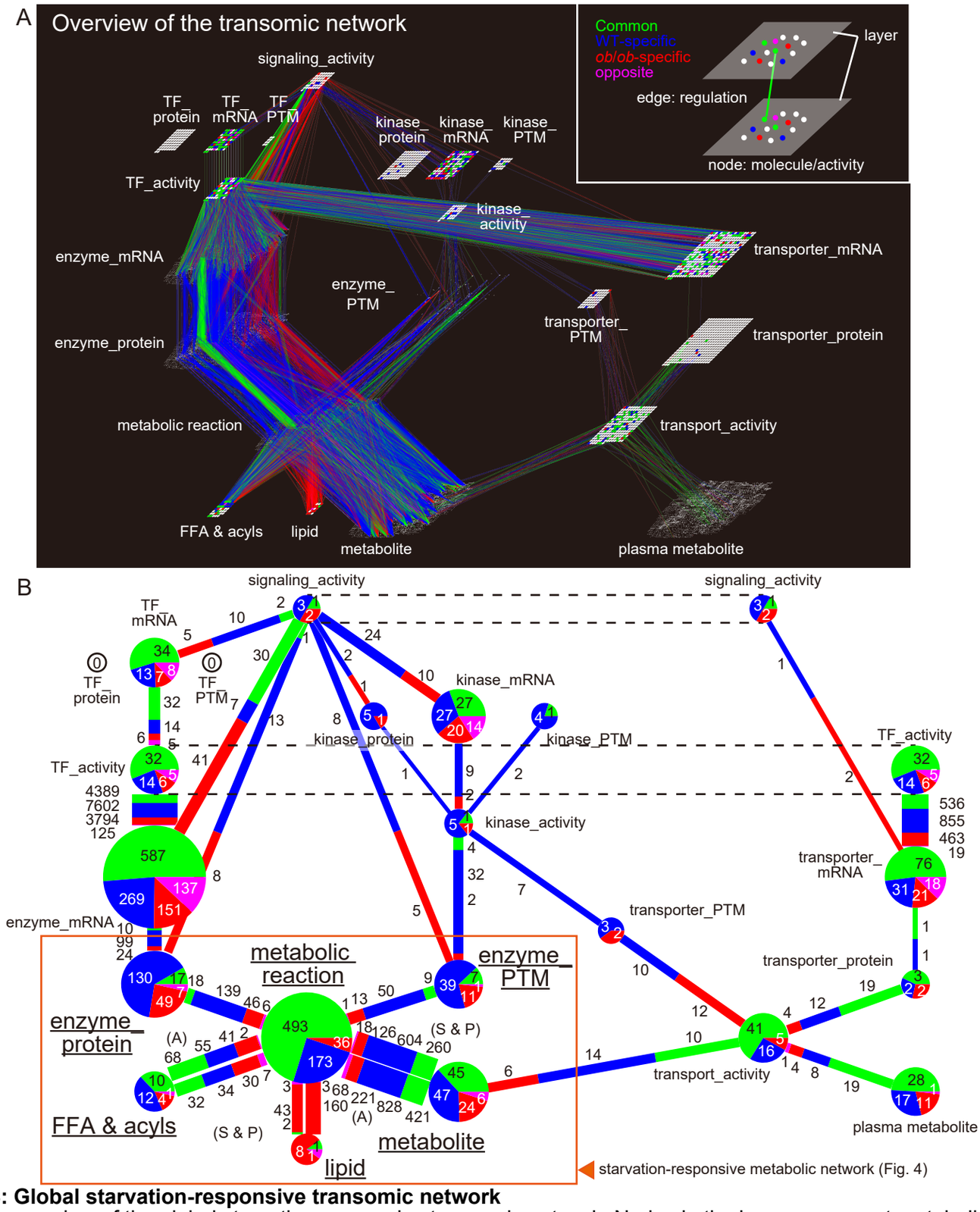

Fig. 3: Global starvation-responsive transomic network
(A) An overview of the global starvation-responsive transomic network. Nodes in the layers represent metabolic reactions, transport activities, measured molecules, measured phosphorylation events, and the inferred activities of TF, protein kinase, and signaling pathway. Edges between the nodes represent regulatory relationships identified using bioinformatic platforms. Colors represent the responsiveness: green indicates common responses both in WT and *ob*/*ob* mice; blue, specific to WT mice; red, specific to *ob*/*ob* mice; magenta, opposite responses between the WT and *ob*/*ob* mice. For metabolic reaction and transport_activity layers, the classes were defined by the existences of regulations regardless of the regulatory directions (activation or inhibition): green indicates the node is regulated in both WT and *ob*/*ob* mice; blue, specific to WT mice; red, specific to *ob*/*ob* mice. (B) The proportions of nodes and edges classified as common (green), WT-specific (blue), *ob*/*ob*-specific (red), and opposite (magenta) in the global starvation-responsive trans-omic network. Pie charts represent the distribution of nodes in the omic layers, and bar plots between pie charts represent the distribution of edges between omic layers. Type of regulation into the metabolic reactions for metabolite, FFA& acyls, and lipid are indicated as allosteric regulation (denoted as “A”) and substrate and product (denoted as “S & P”). The starvation-responsive metabolic network is outlined in orange, and layer names included in the starvation-responsive metabolic networks are underlined.

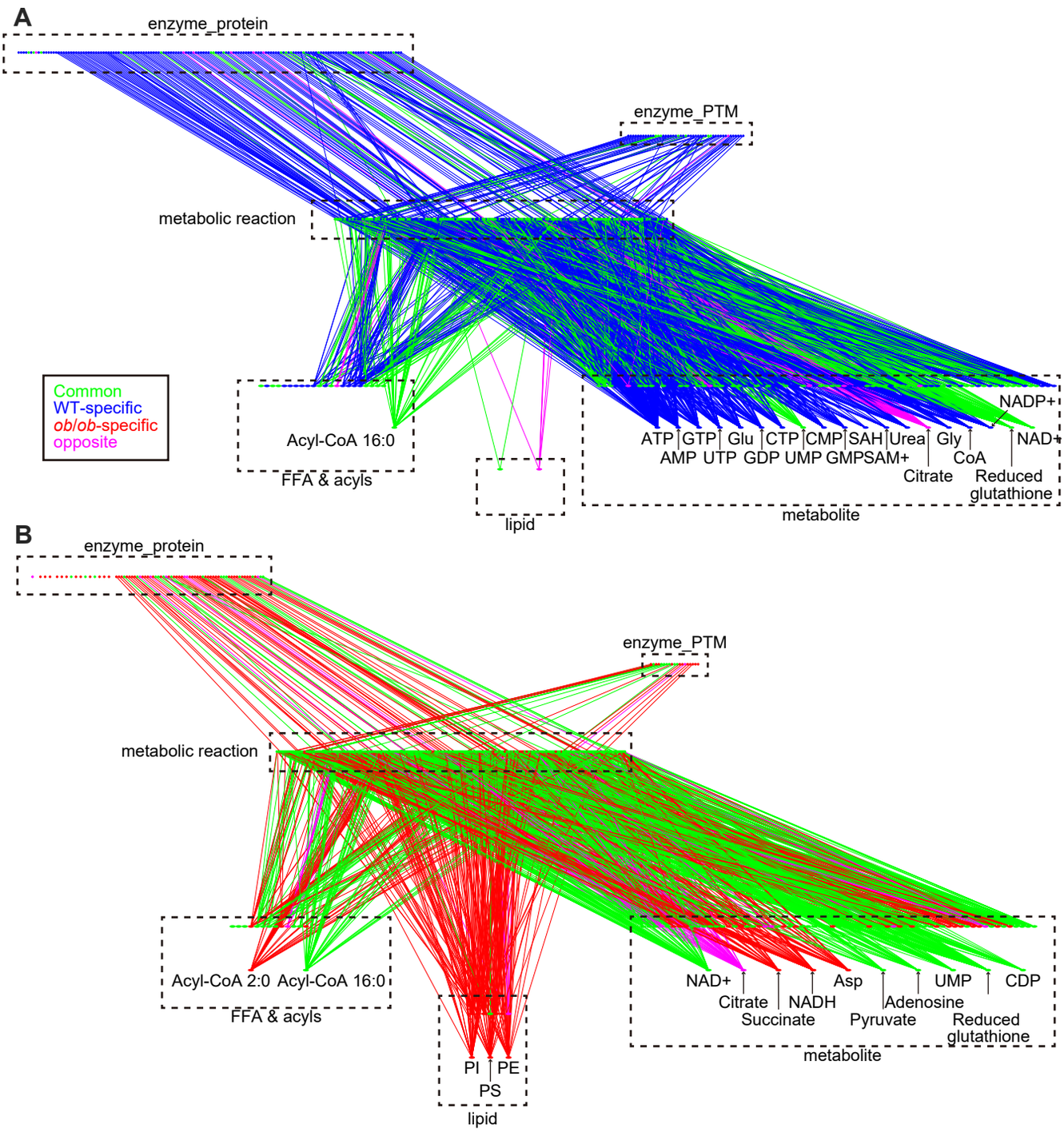

Fig. 4: Starvation-responsive metabolic network
Projected views of the starvation-responsive metabolic networks in WT (A) and *ob*/*ob* mice (B). The network is composed of direct regulators of metabolic reactions: metabolites, lipids, FFA & acyls, enzyme_proteins, and enzyme_PTMs. Colors represent the responsiveness: green indicates common responses both in WT and *ob*/*ob* mice; blue, specific to WT mice; red, specific to *ob*/*ob* mice; magenta, opposite responses between the two genotypes. Hub nodes, which will be defined in Fig. 5, are labeled.

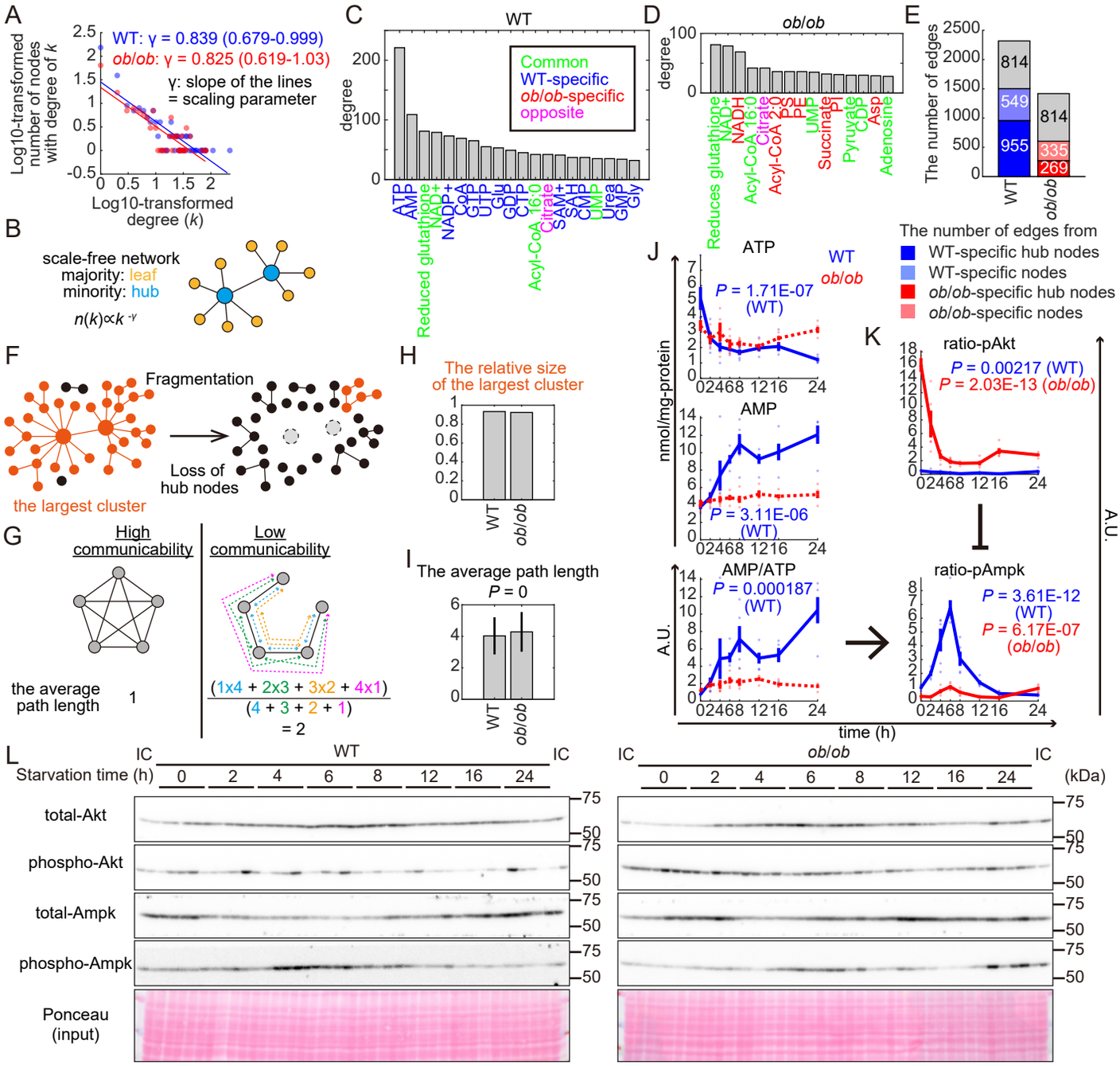

Fig. 5: Structural properties of the starvation-responsive metabolic network
(A) Degree distributions of the starvation-responsive metabolic network in WT (blue) and *ob*/*ob* (red) mice. The x-axis represents the log10-transformed degree (k); the y-axis represents the log10-transformed number of nodes with degree of k. Lines show the linear regression of the degree distributions. The slope of the lines (γ), which is defined as a scaling parameter, and the 95% credible interval are shown. n = 990 in WT and n = 721 in *ob*/*ob* mice for the number of nodes. (B) Diagram of a scale-free network, where $n(k)$ denotes the number of nodes with degree of k, and γ is a constant called a scaling parameter. Circles represent nodes; lines represent edges. Light blue represents the hub nodes; yellow represents leaf nodes. (C and D) Hub nodes with the top 2% highest degree in WT (C) and *ob*/*ob* mice (D). The x-axis represents hub nodes. The y-axis represents degrees. Colors represent the responsiveness: green indicates common responses both in WT and *ob*/*ob* mice; blue, specific to WT mice; red, specific to *ob*/*ob* mice; magenta, opposite responses between WT and *ob*/*ob* mice. (E) The number of edges (y-axis) from WT-specifically responsive hub nodes (blue), WT-specific nodes except for the hub nodes (light blue), *ob*/*ob*-specific hub nodes (red), *ob*/*ob*-specific nodes except for the hub nodes (light red), other nodes (commonly or oppositely responsive, gray). (F) Illustration of fragmentation of a network through loss of hub nodes. The largest cluster is orange. (G) Illustration of how communicability of a network influences average path length (average length of the shortest paths between all the pairs of nodes). (H) The relative size of the largest cluster in the starvation-responsive metabolic network in WT and *ob*/*ob* mice, calculated as the number of nodes in the largest cluster of the network divided by the total number of responsive nodes in the network for each genotype. (I) The average path length of the starvation-responsive metabolic network in WT and *ob*/*ob* mice. n = 853,884 paths in WT and n = 443,643 paths in *ob*/*ob* mice. The error bars show standard deviation. P value of t-test is shoiwn. (J) Time courses of ATP, AMP, and AMP/ATP ratio during starvation in WT and *ob*/*ob* mice. The x-axis represents the starvation time (hours) and the y-axis represents the concentration (nmol/mg-protein) for ATP and AMP, and ratio for AMP/ATP. Blue lines are the responses to starvation in WT mice, and red lines are those in *ob*/*ob* mice. Solid lines represent that the responses were significant; dotted lines represent no significance. Data are shown as the mean and SEM. Dots represent the data from individual mice. (K) Time courses of phosphorylation ratio of Akt and Ampk during starvation in WT and *ob*/*ob* mice. The x-axis represents the starvation time (hours) and the y-axis represents the phosphorylation ratio (the amount of phosphorylated protein divided by the total amount of protein) of Akt and Ampk. (L) Images of the western blotting analysis for (K) at the indicated starvation time (h) of the indicated genotype. IC represents internal control to normalize the signals across membranes. n = 5 biological replicates per group. P values of one-way ANOVA of the molecules or ratio with significant changes are shown.

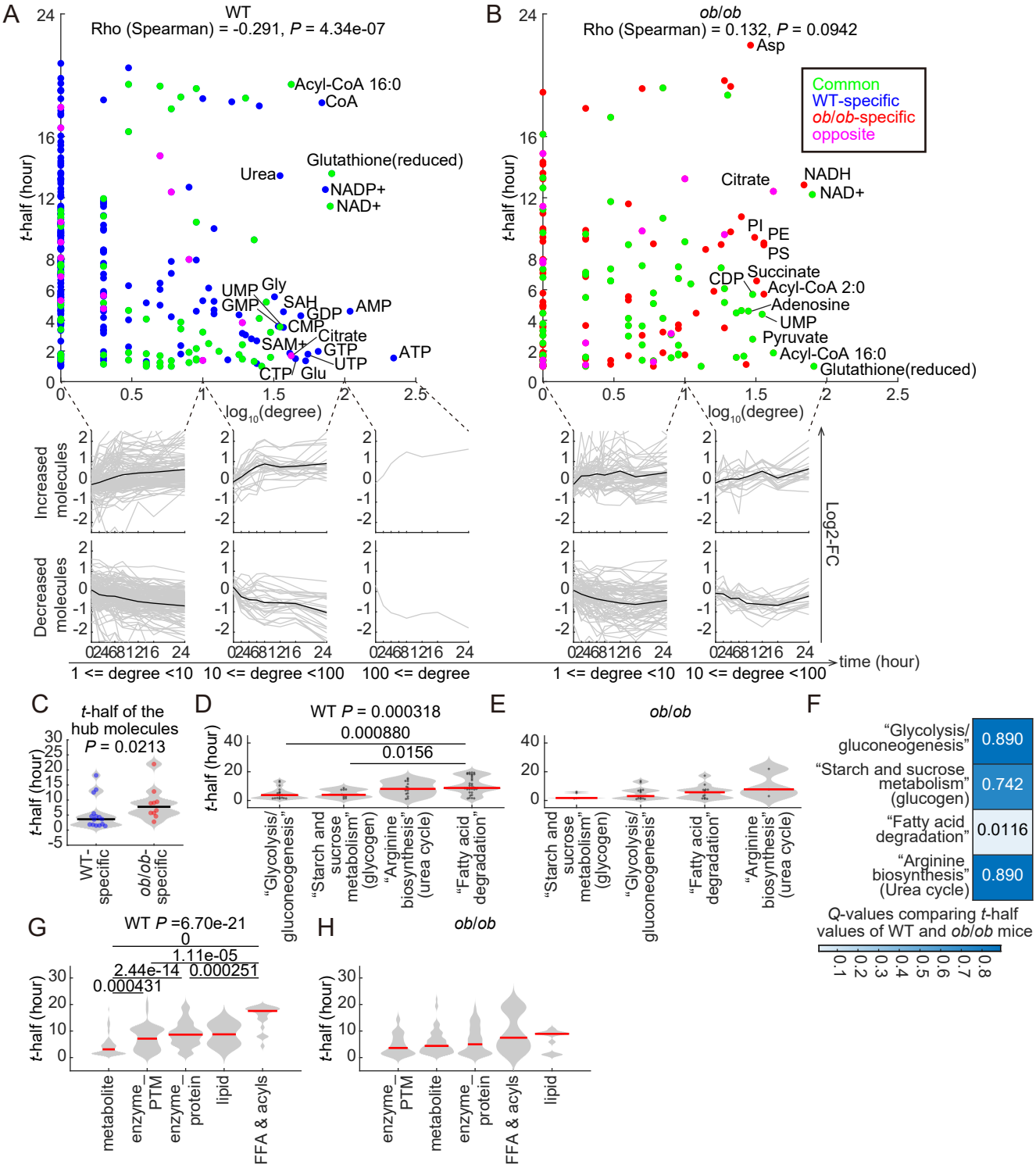

Fig. 6: Temporal order of the starvation-responsive metabolic network in WT mice and its disruption in *ob/ob* mice
(A and B) Scatter plots for the log10-transformed degree (x-axis) and *t*-half (y-axis) in WT (A) and *ob/ob* (B) mice. Dots represent the molecules (including phosphorylation events) in the starvation-responsive metabolic network and colors denote the responsiveness: green indicates common responses both in WT and *ob/ob* mice; blue, specific to WT mice; red, specific to *ob/ob* mice; magenta, opposite responses between WT and *ob/ob* mice. Spearman's correlation coefficient (Rho) and *P* values are shown. Hub molecules for each genotype are labeled (see Fig. 5C and D). Time courses of increased and decreased molecules connected with few (1 ≤ degree < 10), relatively many (10 ≤ degree < 100), and many (100 ≤ degree) edges in WT (A) and *ob/ob* (B) mice are also shown. The x-axis represents starvation time (hours) and the y-axis represents the log2-transformed concentration to the concentrations before starvation of the molecules in each genotype. n = 291 molecules for WT and n = 163 molecules for *ob/ob* mice. (C) Values of *t*-half for the WT-specific and *ob/ob*-specific hub molecules (see Fig. 5C and D). The *P* value of Wilcoxon's rank sum test is shown. n = 15 hub molecules for WT and n = 10 hub molecules for *ob/ob* mice. (D and E) Distributions of *t*-half values of molecules (metabolites, lipids, FFA & acyls, proteins, and phosphorylation events) in the indicated metabolic pathways in WT (D) and *ob/ob* mice (E). The data are ordered along the x-axis by the median t-half (red line) with each molecule represented by a dot. n = 19, 10, 14, and 36 molecules in mice WT for "Glycolysis/gluconeogenesis", "Starch and sucrose metabolism", "Arginine biosynthesis", and "Fatty acid degradation". n = 5, 15, 13, and 3 molecules in *ob/ob* mice for "Starch and sucrose metabolism", "Glycolysis/gluconeogenesis", "Fatty acid degradation", and "Arginine biosynthesis". *P* values of the Kruskal-Wallis test are shown above the panels and those of the Dunn-Sidak test are shown above the lines indicating the pairs of metabolic pathways with significant differences ($P < 0.05$). (F) *Q*-values comparing *t*-half values of WT and *ob/ob* mice for each metabolic pathway. (G and H) Distributions of *t*-half values in each omic layer in the starvation-responsive metabolic network in WT (G) and in *ob/ob* (H) mice. The data are ordered along the x-axis by the median *t*-half (red line). n = 98, 47, 154, 2, and 23 molecules in mice WT for metabolite, enzyme_PTM, enzyme_protein, lipid, and FFA & acyls. n = 19, 75, 73, 15, and 10 molecules in *ob/ob* mice for enzyme_PTM, metabolite, enzyme_protein, FFA & acyls, and lipid. *P* values of the Kruskal-Wallis test are shown above the panels and those of the Dunn-Sidak test are shown above the lines indicating the pairs of omic layers with significant differences ($P < 0.05$).

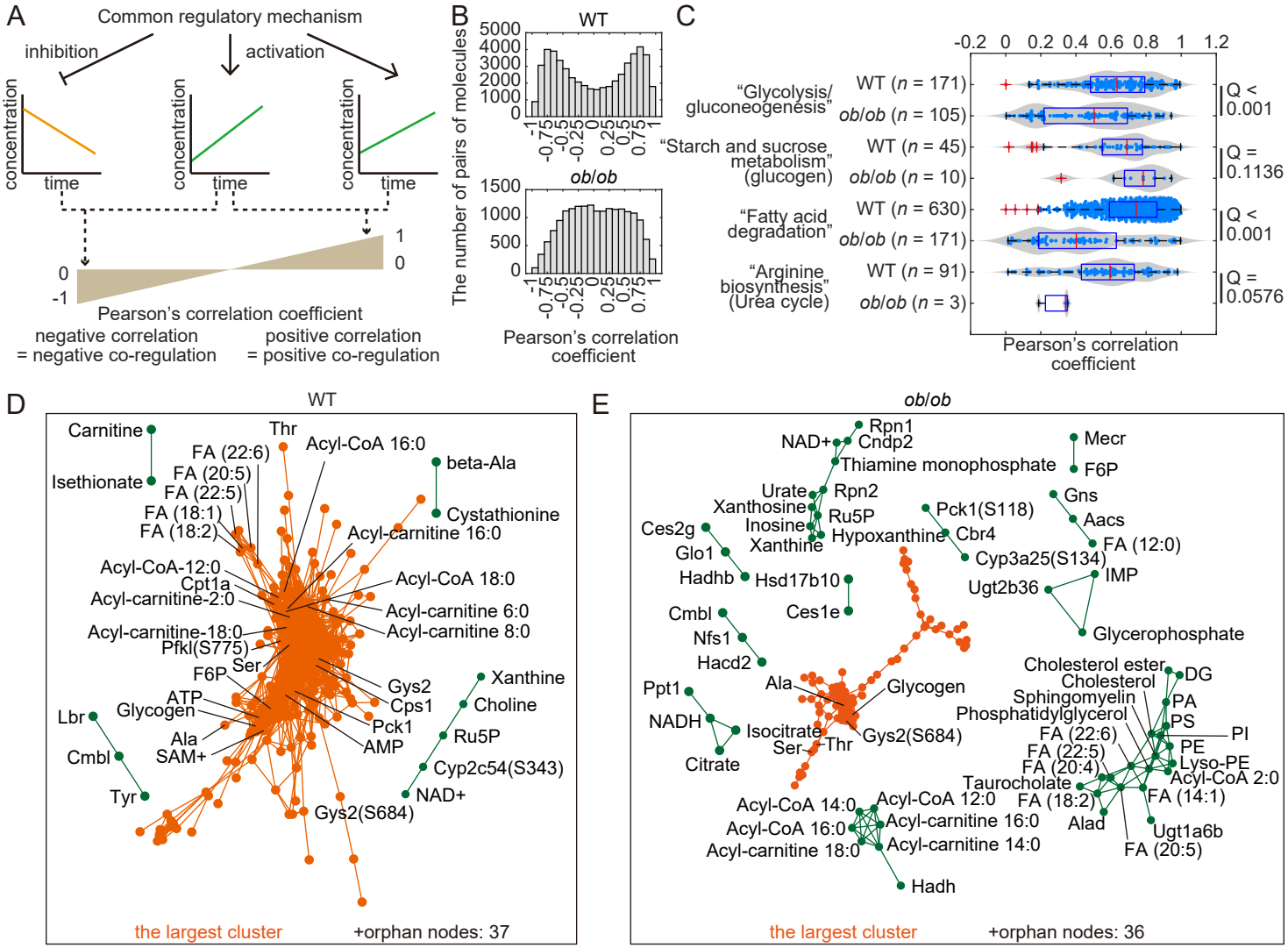

Fig. 7: Co-regulation among molecules in the starvation-responsive metabolic network and disruption in *ob*/*ob* mice

(A) Schematic representation of the analyses for co-regulation among the molecules in the starvation-responsive metabolic network. Time courses of molecules sharing a common regulatory mechanism could be positively or negatively correlated, defined as co-regulation. Pairwise Pearson' s correlation coefficients were calculated for the time courses of molecules that showed significant responses during starvation in the starvation-responsive metabolic network in WT and *ob*/*ob* mice. Positive correlation represents positive co-regulation and negative correlation represents negative co-regulation. (B) Distribution of the pairwise Pearson' s correlation coefficients for time courses of responsive molecules in the starvation-responsive metabolic network in WT and *ob*/*ob* mice. The x-axis represents correlation coefficients; the y-axis represents the number of pairs of molecules examined for correlation. Pairs with an absolute value of correlation coefficient > 0.9 were connected by edges in the correlation metabolic network (see fig. S12). n = 324 molecules for WT mice, n = 192 molecules for *ob*/*ob* mice. (C) The absolute values of pairwise Pearson' s correlation coefficients among time courses of responsive molecules in the indicated metabolic pathways in WT and *ob*/*ob* mice. The x-axis represents the absolute values of Pearson' s correlation coefficient. The y-axis represents metabolic pathways and genotypes. Light blue dots represent the absolute values of pairwise Pearson' s correlation coefficients among time courses of responsive molecules in each metabolic pathway of the starvation-responsive metabolic network. Red vertical lines indicate median, boxes the interquartile range (25th to 75th percentile), and whiskers 1.5 times the interquartile range. Red crosses represent outliers. *Q*-values comparing the correlation coefficients of WT and *ob*/*ob* mice by Wilcoxon rank sum test followed by FDR through Benjamini-Hochberg procedure are shown. The numbers of pairs of molecules are shown in the parenthesis. (D and E) The correlation metabolic network during starvation in WT (D) and *ob*/*ob* mice (E). Orange indicates the largest cluster; all other clusters are dark green. Individual orphan nodes with no connections are shown only by numbers.

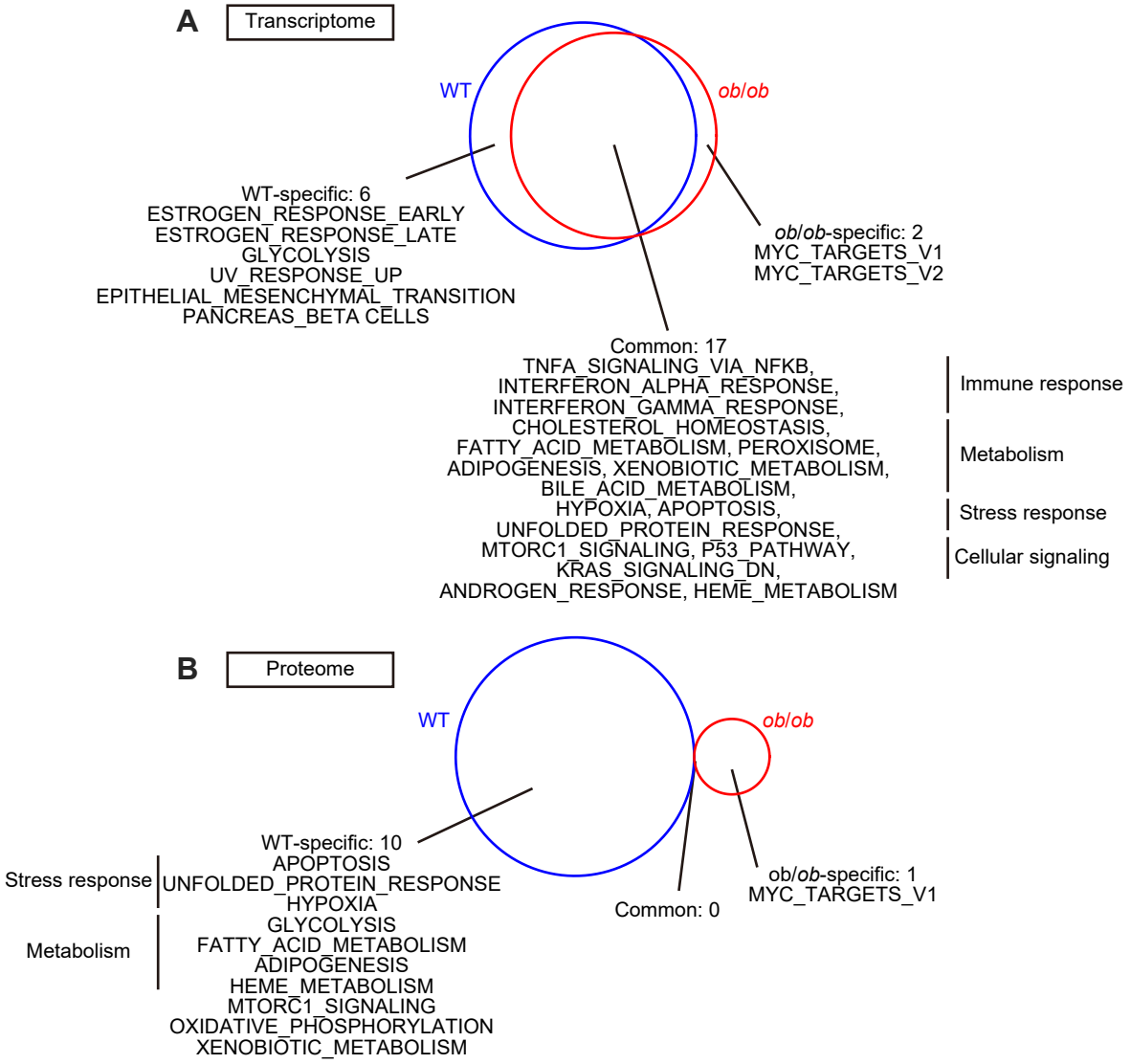

Fig. 8: Functional analysis of transcriptomic and proteomic data for potential clinical application
(A) Enrichment analysis of significantly changed transcripts in WT (blue circle) and *ob*/*ob* (red circle) mice using MSigDB. (B) Enrichment analysis of significantly changed proteins in WT (blue circle) and *ob*/*ob* (red circle) mice using MSigDB.